THERMO-VISCO-ELASTO-PLASTIC MODELING OF COMPOSITE SHELLS BASED ON MECHANICS OF STRUCTURE GENOME

by

Yufei Long

A Dissertation

Submitted to the Faculty of Purdue University

In Partial Fulfillment of the Requirements for the degree of

Doctor of Philosophy

School of Aeronautics and Astronautics

West Lafayette, Indiana

December 2021

THE PURDUE UNIVERSITY GRADUATE SCHOOL
STATEMENT OF COMMITTEE APPROVAL

Dr. Wenbin Yu, Chair

School of Aeronautics and Astronautics

Dr. Weinong W. Chen

School of Aeronautics and Astronautics

Dr. Arun Prakash

School of Civil Engineering

Dr. Vikas Tomar

School of Aeronautics and Astronautics

Approved by:

Dr. Gregory Blaisdell

Dedicated to my mother, Bo Long.

ACKNOWLEDGMENTS

My study for PhD has been more cumbersome than I could ever imagined when I started it. I would like to acknowledge all the people who helped me during this period. Without them this dissertation can never be completed.

First of all I would like to thank my advisor, Professor Wenbin Yu, for his patient guidance, explanation, enlightening, and inspiration on my study. In addition to professional knowledge, Dr. Yu also imparts the methodology of research that benefits me a lot both during graduate study and in the future career. His encouragement during my course of the PhD study also supported me to complete this journey.

I would also like to thank my other committee members, Dr. Weinong Chen, Dr. Vikas Tomar and Dr. Arun Prakash, who spent their valuable time attending my defense as well as providing suggestions on improving the work.

Thanks also go to Dr. C. T. Sun, Dr. Ganesh Subbarayan-Shastri, Dr. Alten Grandt and Dr. James Doyle, whose classes established my fundamental knowledge for doing this work.

I am fortunate to be in Dr. Yu's research group, with a lot of colleagues, among them Orzuri Rique Garaizar, Liang Zhang, Bo Peng, Xin Liu, Zhenyuan Gao, Su Tian, Hamsasew Sertse, Fang Jiang, Ning Liu, Rong Chiu, Fei Tao, Ankit Deo, Haodong Du, Banghua Zhao, Ernesto Camarena etc., to whom I want to show my appreciation, who are delighted to share their experiences in graduate study.

Appreciation to Dr. Juan Fernandez, Dr. Andrew Bergan, Dr. Kunming Mao, Dr. Alireza Forghani, Dr. Anoush Poursartip, and Dr. Kamyar Gordnian for their help on the research topics in this dissertation.

I would like to acknowledge the support from IACMI (The Institute for Advanced Composites Manufacturing Innovation) and NASA during my PhD study.

Last but not least, I would like to appreciate my mother, providing me the opportunity to be educated and study abroad for a higher degree. My appreciation to her is beyond the expression of any language.

TABLE OF CONTENTS

LIST OF TABLES

LIST OF FIGURES

ABSTRACT

Being a widely used structure, composite shells have been studied for a long time. The features of small thickness, heterogeneity, and anisotropy of composite shells have created many challenges for analyzing them. A number of theories have been developed for modeling composite shells, while they are either not practical for engineering use, or rely on assumptions that do not always hold. Consequently, a better theory is needed, especially for the application on challenging problems such as shells involving thermoelasticity, viscoelasticity, or viscoplasticity.

In this dissertation, a shell theory based on mechanics of structure genome (MSG), a unified theory for multiscale constitutive modeling, is developed. This theory is capable of handling fully anisotropy and complex heterogeneity, and because the derivation follows principle of minimum information loss (PMIL) and using the variational asymptotic method (VAM), high accuracy can be achieved. Both a linear version and a nonlinear version using Euler method combined with Newton-Raphson method are presented. This MSG-based shell theory is used for analyzing the curing process of composites, deployable structures made with thin-ply high strain composite (TP-HSC), and material nonlinear shell behaviors.

When using the MSG-based shell theory to simulate the curing process of composites, the formulation is written in an analytical form, with the effect of temperature change and degree of cure (DOC) included. In addition to an equivalent classical shell theory, a higher order model with the correction from initial geometry and transverse shear deformation is presented in the form of the Reissner-Mindlin model. Examples show that MSG-based shell theory can accurately capture the deformation caused by temperature change and cure shrinkage, while errors exist when recovering three-dimensional (3D) strain field. Besides, the influence of varying transverse shear stiffness needs to be further studied.

In order to analyze TP-HSC deployable structures, linear viscoelasticity behavior of composite shells is modeled. Then, column bending test (CBT), an experiment for testing the bending stiffness of thin panels under large bending deformation, is simulated with both quasi-elastic (QE) and direct integration (DI) implementation of viscoelastic shell properties. Comparisons of the test and analysis results show that the model is capable of predicting

most of the measured trends. Residual curvature measured in the tests, but not predicted by the present model, suggests that viscoplasticity should be considered. A demonstrative study also shows the potential of material model calibration using the virtual CBT developed in this work. A deployable boom structure is also analyzed. The complete process of flattening, coiling, stowage, deployment and recovery is simulated with the viscoelastic shell model. Results show that major residual deformation happens in the hoop direction.

A nonlinear version of the MSG-based general purpose constitutive modeling code SwiftComp is developed. The nonlinear solving algorithm based on the combined Euler-Newton method is implemented into SwiftComp. For the convenience of implementing a nonlinear material model, the capability of using user material is also added. A viscoelastic material model and a continuum damage model is tested and shows excellent match when compared with Abaqus results with solid elements and UMAT. Further validation of the nonlinear SwiftComp is done with a nonlinear viscoelastic-viscoplastic model. The high computational cost is emphasized with a preliminary study with surrogate model.

1. INTRODUCTION

1.1 Background and Motivation

Fiber reinforced composite materials have high strength while light weight, which greatly improve the performance of structures. Because of these advantages, they are more and more widely used in engineering. Limited by their manufacturing processes, many fiber reinforced composite structures are shells, having the thickness dimension much smaller than the other two. Regardless of the material, shells are common structures in different aspects of engineering, such as domes of constructions, liquid containers, fuselages and wing skins of airplanes, bodies of automobiles, pressure vessels, hulls of ships etc. When a shell does not have initial geometry, it is degenerated to a plate

Generally, a shell can be modeled in the same way as any three-dimensional (3D) structures. Then, thanks to the fast development of computer technology, a direct numerical simulation (DNS) can be used to obtain the solution, mainly through the finite element method (FEM). However, due to the small thickness of shells, DNS using 3D FEM can easily introduce numerical issues such as shear locking or hourglass effect. Besides, in order to maintain a reasonable element aspect ratio, usually mesh density of the FEM model has to be very high, greatly increase the computational cost of solving the problem. This disadvantage is substantially amplified when the shell is laminated with multiple layers, which is very common for a shell with composite materials. An alternative for overcoming the challenges associated with laminated shells is using the smeared properties, averaging the material properties of several or all layers to simplify the analysis, turning the laminate into so-called black aluminum. Using smeared properties provides moderate increase in efficiency but in the mean time induces inaccuracy in certain global behavior and losing information on stress distribution [1]. On the other hand, shell theories simplify the analysis by representing the original 3D body with a surface, utilizing the feature of small thickness of shell structures. This simplification turns the 3D analysis into a through-the-thickness analysis and a two-dimensional (2D) global analysis, greatly increase the efficiency. However, most shell theories relies on certain assumptions. For example, the classical shell theory are based on the Kirchhoff-Love kinematic hypothesis, assuming that straight lines normal to the shell

reference surface remain straight and normal after deformation, and their length does not change. These kind of assumptions do not always hold true, resulting incorrect solution in some applications. Consequently, a shell theory relies less on ad hoc assumptions is preferred, especially on solving some of the challenging problems featuring heterogeneity and anisotropy.

One of the challenging problems for shell theories is the simulation of the autoclave curing process of composites. Autoclave curing is one of the most common composite manufacturing method. In this process, prepregs, which are prefabricated thin plies having unidirectional continuous fibers impregnated with a matrix material, usually resin, are laid up on a mold whose design is based on the geometry of the part, and then the prepreg laminate is covered with several auxiliary layers and sealed with a vacuum bag, as shown in Figure 1.1. The whole assembly is put in an autoclave undergoing preset heat and pressure history called cure cycle, as shown in Figure 1.2. After curing, the assembly is moved out of the autoclave and cooled down before removing the part from the tool, usually called detooling. During this

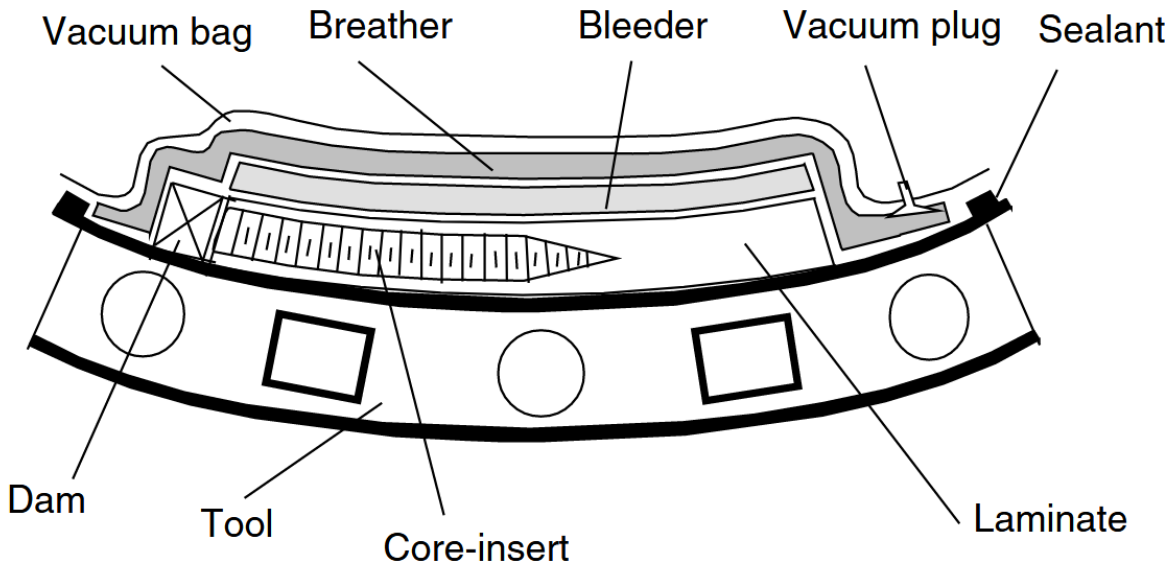

Figure 1.1. Components of the assembly for autoclave curing [2].

curing process, the laminate experiences large temperature change and phase transformation of the matrix. Temperature change generates large thermal strain in the laminate and

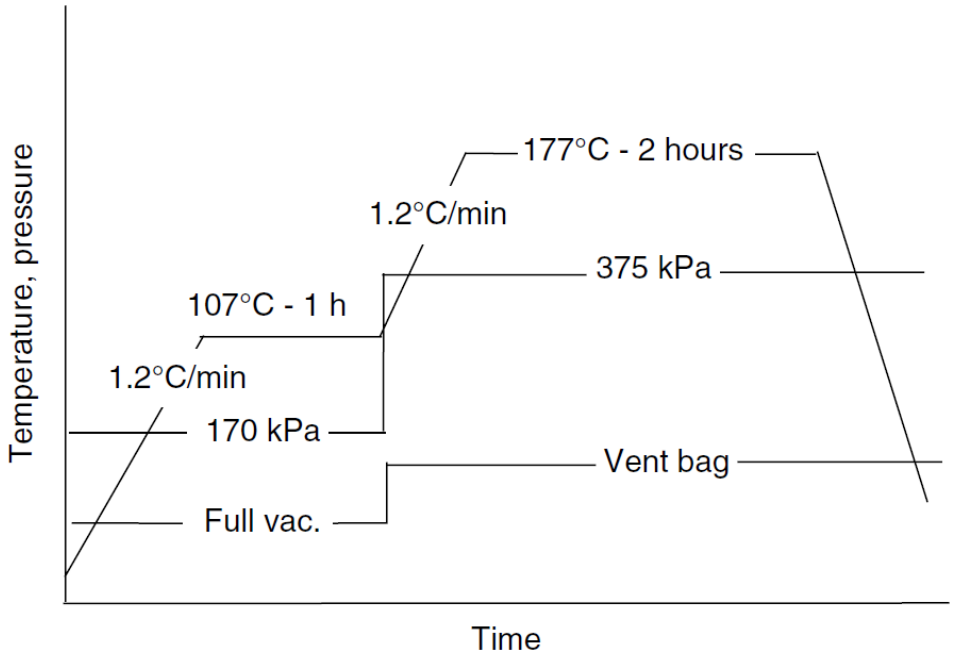

Figure 1.2. Typical autoclave cure cycle [2].

causing temperature dependency of the material properties, resulting in residual stress in the laminate. The phase transformation of the resin, measured by degree of cure (DOC), is another source of residual stress, as during this process the resin has a significant increase in density and stiffness, and a decrease in volume, usually called cure shrinkage. Residual stresses generated by these phenomena lead to a preloaded state of the composite part, and combined with the anisotropy of composites, large deformation can happen after detooling, causing difficulties on assembling or affecting the performance of the composite parts. In order to minimize the influence of manufacturing induced residual stress and deformation, an effective simulation method is required. As most parts manufactured by autoclave curing are laminates, shell theories potentially provide the most efficient way to solve this type of problems.

As mentioned previously, the small thickness of shells makes simulation with 3D FEM costly. When a laminated shell has a very small thickness and a very large surface dimension, a 3D FEM becomes almost impossible. This is the case when it comes to the analysis of thin-ply high strain composite (TP-HSC) deployable structures. TP-HSC [3] has a ply thickness

of only 0.02 to 0.1 mm. Typically, the laminates used are only a few plies thick, and thus much thinner than conventional composites employed, for instance, in commercial airplanes. TP-HSC deployable structures gain notice from researchers of space applications due to their features of light weight and high flexibility. Compared with conventional deployable structures, TP-HSC deployable structures can be applied to space platforms less than 1 m^3, such as small satellite missions. A TP-HSC boom can be rolled onto a hub, only occupying a small volume, while after deployment, size of 5-20 m can be achieved [4]. This makes low-cost deep space exploration using solar sails practical. However, small thickness, large surface dimension and high flexibility also bring difficulties on analyzing the structure. During the coiling of a TP-HSC boom, the structure undergoes large bending deformation, leading to large surface strain, involving both geometric and material nonlinearity. In addition, due to the intrinsic viscoelasticity of composite matrix, and a long time in stowed condition before deployment, time dependent behavior is observed during this period [5]. Combined with large deformation and high strain, deployment failure can occur because of stress relaxation. For example, the boom cannot goes back to its original geometry in length direction, making the solar sail unable to deploy, or it cannot keep its designed cross-section, losing the ability to support the sail. As a result, an efficient method to simulate these physics is critical to the development of TP-HSC deployable structures. A 3D solid model is not feasible as already mentioned, and although a beam model can predict the behavior in the length direction, the large cross section change during rolling to the hub and deployment are hard to capture. On the other hand, a shell model can capture the behavior in both directions and maintain a reasonable computational cost. Consequently, a shell model is the most suitable method for analyzing TP-HSC deployable structures.

In the research and application of TP-HSC and deployable structures, permanent deformation is also noticed [6], [7]. This is mainly because the intrinsic time-dependent behavior of the resin not only includes viscoelasticity, but also viscoplasticity. The material behavior can be in elastic regime at the beginning of the stowage while in the long stowage period yielding can be initiated. Different from the stress relaxation in viscoelasticity, the residual deformation caused by viscoplasticity will not be fully recovered. Permanent deformation greatly affects the performance and reliability of space platforms [8], so it is critical to

develop a nonlinear modeling technique to analyze this phenomenon. Compared to a 3D solid model, a nonlinear shell model is more suitable for this purpose. In addition to the the reasons mentioned previously, a shell model can further outperform 3D models because nonlinear analysis are usually incremental, so the computational speed improvement can be more significant. Besides, if shell elements are used for global structural analysis, 3D solid model can lead to accuracy loss if the shell formula of the global structure solver cannot accurately recover the 3D variables, because in nonlinear analysis, current loading state affects the behavior of the next increment. As a result, a nonlinear shell theory should be adopted for analyzing the nonlinear behavior of TP-HSC and deployable structures.

1.2 Literature Review

This section reviews literature related to this study. The first part is focused on the development of shell theories and MSG. Then the two applications concerned in this study are reviewed: firstly on the curing of composites, which involves thermoelasticity, and secondly TP-HSC deployable structures, which emphasizes time-dependency and nonlinearity.

1.2.1 Shell Theories and MSG

Because of the common applications of shell structures, shell theory has been a research topic for a long time. The development of a shell theory can start with the analysis of a 2D continuum, as firstly proposed by Cosserat brothers [9]. Other contributors of this method includes Ericksen [10], Naghdi [11], [12], Toupin [13], Green [14], Cohen [15] et al. Some researchers such as Simo [16], Fox [17] and Ibrahimbegovic [18] had put efforts on the computational implementation of shell theory derived in this way based on numerical methods such as FEM. However, this derivation method neglect the fact that a shell is a 3D body in real world, resulting in the difficulty of obtaining a constitutive relation based on 3D materials [19]. It was suggested by Reissner [20] that experimental methods or a derivation from the original 3D structure can be adopted to get the constitutive relation. For this reason, shell theories of this kind are not commonly used in engineering.

Alternatively, a shell theory can also be derived from 3D continuum. A process called dimensional reduction is carried out to transform the original 3D continuum problem to a 2D problem to be solved on the reference surface. One way to achieve this is by assuming the distribution of 3D fields through the thickness, and then 2D variables on the shell reference surface can be obtained by an integral in the thickness direction. One of the oldest, and maybe the most widely used assumptions are the Kirchhoff-Love assumptions [21], [22], extended from the Euler-Bernoulli beam assumptions. Improvements of shell theories based on the origin work of Love have been done by Goldenveizer [23], Lurie [24], Novozhilov [25], Koiter [26], Sanders [27], Budiansky [28] et al., including removing inconsistencies, reducing stress resultant measurements, alternating the strain measurements of the 2D reference surface, or even release one or some of the assumptions that can lead to a first-order shear deformation theory. Some higher-order distributions of 3D fields are assumed by researchers, such as the third-order theory by Reddy [29]. Another way to do the dimensional reduction is using an asymptotic method to expand the 3D quantities into series of the thickness coordinate, such as the work by Carrera [30]. When applied to composite shells, the complexity of formulation can greatly increase due to the anisotropy and heterogeneity.

On the other hand, using mechanics of structure genome (MSG), a new theory that unifies micromechanics and structural analysis presented by Yu [31], [32], a shell theory is possible to greatly reduce computational cost while maintaining high accuracy. The MSG is a theory that a Structure Gene (SG) is chosen to represent the smallest mathematical building block of the structure, and then following the Principle of Minimum Information Loss (PMIL) [33], the constitutive relation is derived for the SG via the Variational Asymptotic Method (VAM) developed by Berdichevskii [34]. The MSG-based shell theory is extended from Yu and his co-authors' work of [35], [36]. Compared to other shell theories, MSG-based shell theory does not rely on assumptions of the distribution of 3D quantities, and it is capable of handling fully anisotropy and complex heterogeneity. It has been applied to solve different problems including smart materials [37]–[39], functionally graded materials [40] and time dependent material properties [41]. A detailed introduction of MSG is included in Chapter 2.

1.2.2 Curing Simulation of Composites

Simulation of the curing process of composites consists of two parts, a thermochemical part that calculates the temperature distribution, phase transformation, DOC, and material properties depending on these quantities, and then a stress-deformation part that calculates the residual stress based on the results of the thermochemical part, and the final deformation after detooling. This study only focuses on the stress-deformation part of the simulation.

Because of the complex nature of the manufacturing process, lots of efforts are made on different aspects of the process. Early research includes Hahn and Pagano's work in 1975 [42], in which a classical lamination theory (CLT) based model was built and temperature dependent material properties were considered, while only the cooling-down from a stress-free state was analyzed. In 1983, a comprehensive model was provided by Loos and Springer [43], in which through-the-thickness thermochemical and resin flow effects were discussed but little emphasis was given to residual stress and deformation. In 1990s, White and Hahn [44] implemented an experimental study on the generation of residual stress during curing. The results were further developed into a model for predicting the resultant curvature after the process [45], [46]. Bogetti and Gillespie [47] did a cross-sectional analysis on heat transfer and cure kinetics of thick composites, and thereafter a detailed analysis on the generation of residual stress [48], with the final residual stress obtained using CLT. Johnston [49] developed a finite element based method to simulate the curing process with three separated sub-models: thermochemical, flow, and stress, with all of them under a plane strain assumption. In the stress model, detooling process was also considered.

In recent years, focus has been laid on improving the performance of residual stress and deformation prediction. Interaction between the tool and composite part was investigated by Twigg et al. [50], [51], and results showed that for a certain layup, part geometry and processing conditions were the most significant factors to affect part warpage. Clifford et al. [52] used FEM to do the analysis with flat region modeled with shell elements and curved region with solid elements. An over-prediction was observed compared with experiment. Zobeiry et al. [53] analyzed the application of viscoelastic material models on composites curing simulation and found that a more sophisticated model provides better accuracy but

is more computationally expensive and more difficult to calibrate the parameters. Arafath et al. [54] developed two higher-order brick elements for dealing with large stress gradient through the thickness and in the mean time increasing computational efficiency. Arafath et al. [55], [56] obtained an analytical solution of stresses and deformation of a composite part processed on a solid tool while several assumptions were adopted. Ersoy et al. [57] studied the spring-in of a curved part by simplifying the curing procedure into two steps. The effect of shear was analyzed. Kravchenko et al. [58] put forward a multiscale model for predicting the cure shrinkage and thermal strain in thermoset matrix. Kappel et al. [59] developed a simulation strategy that can be applied with different finite element models with either solid or shell elements. Element parameters were obtained from experiments using simple samples. Ding et al. [60] found an analytical solution to predict the spring-in of curved composite parts from the strains in both through-the-thickness and length directions. Gordnian [61] developed a thermo-viscoelastic model that can predict the deformation and residual stress of both thermoset and thermoplastic polymer composites. Li et al. [62] compared the influence of different constitutive models on residual stress and cure shrinkage. An elastic model was observed to have large error. Gordnianet al. [63] studied the effect of different cure cycles on the deformation of the composites parts. Numerical results were compared with experiments. Chen and Zhang [64] developed a multiscale model with both thermochemical and stress-deformation analysis. Viscoelastic model was adopted and the warpage of an anti-symmetric laminate was studied.

A commercial code using Abaqus as the solver called COMPRO [65] is developed to simulate the manufacturing process. However, similar to most of the researches presented here, solid elements are adopted. Using the residual stress output from COMPRO, a detooling research was done by Rique et al. [66] using shell elements, showing the feasibility of applying MSG-based shell theory on curing simulation of composites.

1.2.3 TP-HSC Deployable Structures

Research on TP-HSC deployable structures falls in three categories: design of the TP-HSC boom, analysis of constitutive relations, and simulation of global structures. The design

of boom focusing on optimization of cross-sectional stiffness falls in the field of beam theory, so it is out of the area of this study. Because of the potential coupling between structure and material behavior [3], constitutive relation used in the global shell structure analysis should be directly obtained from the original heterogeneous material instead of a lamination theory to avoid loss of accuracy [4]. In addition, time-dependent material properties also need to be considered. Mallikarachchi [67], [68] homogenized thin-walled composites used in tape spring hinges as Kirchhoff-Love plates, with elastic material properties. Failure analysis was proceeded based on this framework [69]. Kwok and Pellegrino [70] studied the viscoelastic behavior of a single-ply plain weave composite using the representative volume element (RVE) analysis. The result was in the form of Prony series of the ABD stiffness matrix, and validated by simulation and experiment of a tape spring. This work was extended by Hamillage et al. [71] to be applied on TP-HSC with multiple plies. Tetsuka et al. [72] analyzed the properties of woven composites considering temperature dependency and viscoelastoplasticity, by using a multiscale method.

In addition to numerical methods, experiments are also designed to evaluate the bending stiffness of TP-HSC, including the simple vertical test [73], the platen test [74], [75], the large deformation four-point bending (LD-FPB) test [76], and the latest being the column bending test (CBT) [77]. The CBT loads the specimen in compression with pinned ends offset from the specimen's neutral axis, generating a stress state close to pure bending. Numerical simulations of the CBT can be used to evaluate modeling techniques and material constitutive models, and to improve understanding of test results. In addition, the CBT model can be used as a tool for calibrating properties based on the experimental data [78]. Limited work has been done in modeling the CBT for TP-HSC. Sharma et al. [79] analyzed the CBT based on Euler's elastica theory to account for large deformation of one-dimensional (1D) structural elements, and compared with a kinematic solution and experiments. Nonuniform deformation along the loading direction was observed. Rose et al. [80] used a CBT simulation in Abaqus to verify the modeling technique referred to as the coincident element method. In this method, independent layers of orthotropic elastic and isotropic viscoelastic shell elements share nodes, so that orthotropic viscoleastic behavior can be simulated with current Abaqus built-in capabilities. Gomez-Delrio and Kwok [81] analyzed the bending of

a TP-HSC plate with a simplified analytical model and a finite element simulation. They found that the results from these two approaches match well when a uniform distribution of curvature is assumed. As identified in [80], [81], the most appropriate way of simulating CBT with the finite element method is using shell elements, due to the small thickness of TP-HSC.

To understand the influence of large bending deformation and long stowage time, a global structural analysis of TP-HSC deployable structures is also necessary to support practical engineering applications. However, due to the complexity of modeling a deployable structure with one or more booms and a coiling hub, and the highly nonlinear process of coiling and deployment, many researchers have used simplified models. Bai te al. [82] studied the flattening and bending of a lenticular boom using an analytical method. Results were only accurate for small displacement when compared with experiments. Brinkmeyer et al. [83] analyzed the effect of long stowage time to the deployment of a bi-stable tape spring by comparing an analytical solution with experiments. Failure of deployment caused by long stowage time was not captured by the analytical solution. Hu et al. [84] compared two different methods for flattening a lenticular boom by FEM and experiments. Compression was found to generate less stress than tension. Borowski et al. [85] studied large bending, stowage and release of a tape spring. Instead of directly providing the ABD matrix [70], stiffness of the FEM simulation model came from 3D material properties of lamina. Gomez-Delrio and Kwok [86] developed an analytical solution of viscoelastic tape spring based on instantaneous folding and deploying. Good agreements with FEM were found on relaxation only. Cox and Medina [87] studied strain development and buckling of a triangular boom during rolling, with elastic material properties. Yang et al. [88] did an optimization on section moments and dynamic properties of a triangular boom based on FEM simulation of rolling the boom on the hub for 360°. Scherbarth and Taha [89] simulated the stowage and deployment of a tape spring rolling to a hub, with different time and temperature, using shell elements with Abaqus Explicit. Results were compared with experiments. Leclerc and Pellegrino [90] studied the stress concentration of a triangular boom during coiling using Abaqus. The effect of materials, cross-sections and flattening mechanisms were compared and found that both a varying cross-section and nip rollers can reduce stress concentration.

Gomez-Delrio and Kwok [91] simulated the flattening of a segment of a lenticular boom to analyze the effect of long stowage time on cross-section, but no coiling process was involved. Validated models capable of simulating the entire process of coiling, stowage and deploying of a deployable composite boom structure considering the time-dependent material behavior are still needed, especially for booms with complex cross-sections, such as those for lenticular booms.

1.2.4 Nonlinear Shell Modeling

Research on the nonlinear behavior of shells has focused on different aspects. Both geometric and material nonlinearity have been discussed. Most of the studies analyze material nonlinearities, either homogeneous material or composites, with 3D solid models, and then apply on shells through the lamination theory or developing shell finite elements that use the 3D constitutive relations. Ramm and Matzenmiller [92] developed a formula for elasto-plastic shell based on Newton's method and the concept of degenerated soild, which requires the normal stress to be zero. Swaddiwudhipong and Liu [93] analyzed the elasto-plastic response of shells using a shell element based finite element formula with a time marching sheme. Wang et al. [94] derived a elastic-viscoplastic model for composites and implemented through plate/shell finite element based on the lamination theory. Peng and Cao [95] studied the nonlinear elastic behavior of textile composites using a 2-step homogenization method. Both steps are based on 3D solid model and finally effective shell properties are obtained through matching the reaction force and displacement of a shell element to the RVE. Chen et al. [96] derived the analytical formula for heterogeneous spherical nonlinear elastic shells. Rabczuk et al. [97] developed a meshfree shell formula that can model various nonlinear shell behaviors. This model is especially suitable for crack analysis. Caseiro et al. [98] developed the formula of a shell element for nonlinear shell analysis that calculates the strain using a new sets of calculating points instead of the conventional integration points. Goncalves et al. [99] analyzed the buckling and post buckling behavior of sandwich shells using a multi-scale nonlinear shell theory based on RVE analysis and first-order shear deformation theory. Currently, number of studies on directly using a nonlinear shell modeling to analyze shell

behavior with material nonlinearities are limited. Development of a nonlinear shell homogenization algorithm that can be applied with various material constitutive models is critical to analyze the permanent deformation and other nonlinear behavior in shell structures such as the TP-HSC deployable structures.

1.3 Objectives and Outline

Although there exist a number of shell theories, most of them have limitations on applying to problems with composite materials. Theories with difficulty on obtaining constitutive relations are generally not suitable for engineering applications. Ad hoc assumptions of displacement and stress distributions can introduce significant loss of accuracy when considering the anisotropic and heterogeneous nature of composites. Even though most composite structures manufactured by autoclave curing are shell structures, because of the complex physics during this process, simulations of composites curing are mostly done by solid models, which either greatly increase the computational cost, or decrease accuracy when smeared properties of sub-laminate are adopted. In order to reduce the error of global analysis on TP-HSC deployable structures, shell constitutive model should be based on the original heterogeneity of TP-HSC, while this is only applied on simplified structures like a tape spring.

In order to overcome those above mentioned limitations, MSG-based shell theory is developed in this work. It is capable of handling fully anisotropy and complex heterogeneity, as well as multiphysics. For this reason, it is proposed to use the MSG-based shell theory to solve the challenges brought up by composites curing simulation, TP-HSC deployable structures, and nonlinear shell analysis with the objectives as listed.

1. Obtaining the general formula of MSG-based shell theory, with the ability to handle full anisotropy and heterogeneity, and expanding it to include the physics during composites curing, as well as to solve nonlinear problem.

2. Simulating the residual stress development during the curing process of composites, and deformation after detooling, by using shell elements to model the composite parts.

3. Analyzing the time-dependent properties of TP-HSC, and simulating the coiling, stowage and deployment process of TP-HSC deployable boom and hub structures, using shell models with stiffness obtained from the original heterogeneous material.

4. Developing a nonlinear shell model that can be used for analyzing various types of nonlinear shell behaviors including time-dependent yielding and permanent deformation.

All the structural simulations are done with FEM using Abaqus, with shell constitutive models provided by MSG-based shell theory implemented as user subroutines that define the stiffness of shell elements.

Outline of this report is arranged as followed. Chapter 1 includes the background and motivation of this study, a comprehensive literature review, and the objectives and outline of this study. Chapter 2 introduces the fundamentals of MSG, and presents the formulation of MSG-based shell theory of both linear and nonlinear analysis. Chapter 3 firstly modifies MSG-based shell theory to include the physics during composites curing and high order corrections, and then examples are analyzed to demonstrate the capability of MSG-based shell theory. Chapter 4 validates the capability of MSG-based shell theory on analyzing large bend deformation of TP-HSC with viscoelasticity and simulates the coiling and deployment of deployable boom and hub structures. Chapter 5 implements the MSG-based nonlinear shell model with a user material interface and validates the implementation with viscoelastic, damage, and viscoplastic material models. Chapter 6 summarizes the results of this dissertation and discuses possible future work.

2. MSG-BASED SHELL THEORY

2.1 Introduction of MSG

MSG is a unified theory for constitutive modeling of heterogeneous materials and structures [31], [32]. MSG separates the original problem into a global macroscopic analysis and a local microscopic analysis. It is a general-purpose method for different kinds of structures including 3D solids, 2D plates/shells, and 1D beams. This study focuses on 2D plates/shells, and because plates can be treated as shells without initial curvature, the term "shell" is used without the loss of generality.

Constitutive modeling using MSG is achieved by analyzing the structure gene (SG), defined as the smallest mathematical building block of the structure. The term gene is chosen to emphasize the fact that it contains all the information required for the constitutive modeling of a structure, in the same way as in biology gene contains all the information for organism's growth and development. For a shell structure, the SG can be 1D, 2D or 3D, depending on the microstructural characteristics of the origin 3D shell body. As shown in Figure 2.1, if the shell has no heterogeneity in its surface directions, such as a laminate with the laminae considered as homogeneous, the SG is the 1D transverse normal line with each segment representing a corresponding layer (see Figure 2.1a); if the shell has heterogeneity in one of its surface directions, such as a sandwich panel with corrugated core, the SG is 2D (see Figure 2.1b); if the shell has heterogeneity in both of its surface directions, such as a woven composite panel, the SG is 3D (see Figure 2.1c). Every material point in the 2D global shell model has an SG associated with it, the constitutive modeling of which can provide effective shell properties and dehomogenization relations to recover the original 3D fields from the global shell behavior.

MSG formulation starts with kinematics that relates the 3D kinematic fields of the original structure to those of the macroscopic model and fluctuating functions. For this purpose, two sets of coordinate systems are introduced. First is the macro coordinates x_i, which represent the coordinates of the global structure. For shells, only x_α describe the reference surface exist and x_3 is eliminated. From here and after Greek indices assume 1, 2, and Latin indices assume 1, 2, 3. Repeated indices indicate summation over their range unless under-

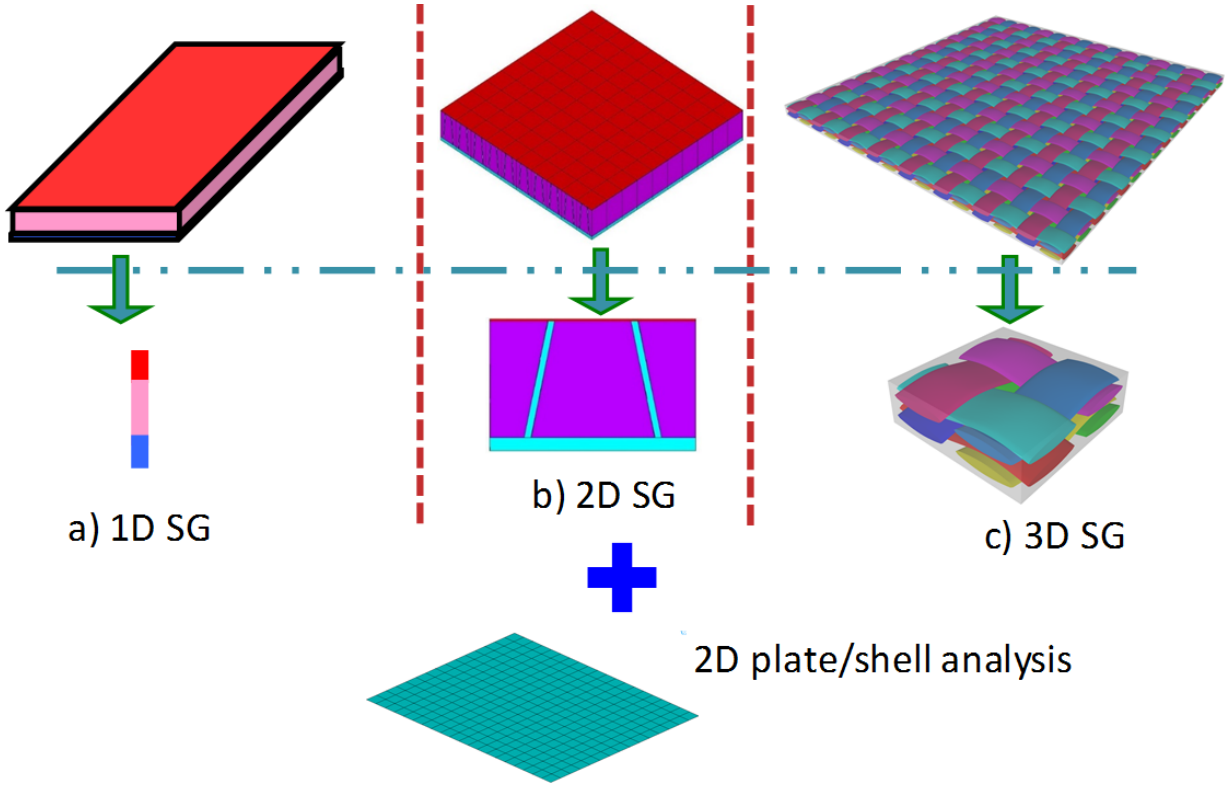

Figure 2.1. SG for shell structures.

lined or explicitly described. Because an SG represents the smallest building block, its size is much smaller than the wave length of the deformation of the global structure, a second set of coordinates, micro coordinates y_i, can be introduced. The macro coordinates and micro coordinates can be related with a small parameter ε, so that $y_i = x_i/\varepsilon$, but notice that during the analysis of a specific problem, ε does not need to be assigned a value. Depending on the dimension of SG, some of y_i can be eliminated. For example, only y_3 exists for a 1D SG. Based on this coordinate system, a field function f of the original structure can be written as a function of x_i and y_i, and its partial derivative can be expressed as [100]

$$\frac{\partial f\left(x_k, y_j\right)}{\partial x_i} = \left.\frac{\partial f\left(x_k, y_j\right)}{\partial x_i}\right|_{y_j=\text{const}} + \frac{1}{\varepsilon}\left.\frac{\partial f\left(x_k, y_j\right)}{\partial y_i}\right|_{x_k=\text{const}} \equiv f_{,i} + \frac{1}{\varepsilon} f_{|i} \tag{2.1}$$

Here the equation is in the case of shell structure with 3D SG. After the kinematics is established, variational statement of the structure can be formed. Variational statement comes from the governing functional of the original structure, for linear elastic structures

being the total potential energy, derived through substituting the kinematic relation in to it and following the PMIL, which states that the difference between the governing functional of the original 3D heterogeneous model and the macroscopic model should be minimized [33]. Then, constitutive relations can be solved using VAM. Depending on the global behavior to be captured, models of different orders can be obtained.

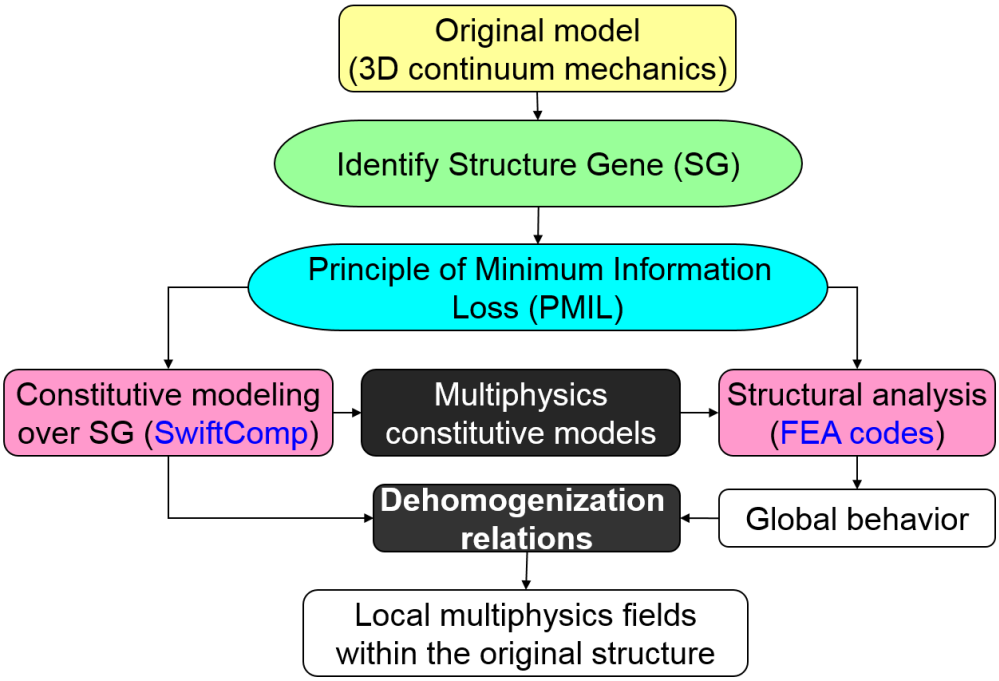

Figure 2.2. Workflow of structural analysis using MSG.

For MSG-based constitutive modeling of shells, effective shell properties can be calculated directly in terms of the material properties of the materials inside the SG, which can be obtained from experiments. A MSG-based shell analysis includes two levels: MSG-based homogenization and structural analysis using shell elements, as shown in Fig. 2.2. The process starts with MSG-based homogenization with the SG identified first. Depending on the structure to be analyzed, the SG can be microscale and/or mesoscale. Geometry as well as the constitutive models of the materials are included in the SG. A general-purpose constitutive modeling code SwiftComp [101] is developed based on MSG. It can be used to obtain the effective shell properties by homogenization. Based on the geometry and material of the SG, effective properties can be obtained either by SwiftComp. MSG-based homogenization can

be applied on different kinds of material constitutive models, either linear or nonlinear [102]–[104]. Effective properties calculated based on MSG are used in the global structural simulations. For most nonlinear and some linear material models, developing a user-subroutine would be necessary. For example, if the solver for structural simulation is Abaqus/Standard, and then the user-subroutine UGENS is used for implementing the effective shell properties. Results of the global structural simulation can be used for dehomogenization if the loading history follows step type behavior. The dehomogenization can show the distribution of displacement, stress and strain inside the SG at a point of interest in the global structural model.

2.2 Kinematics

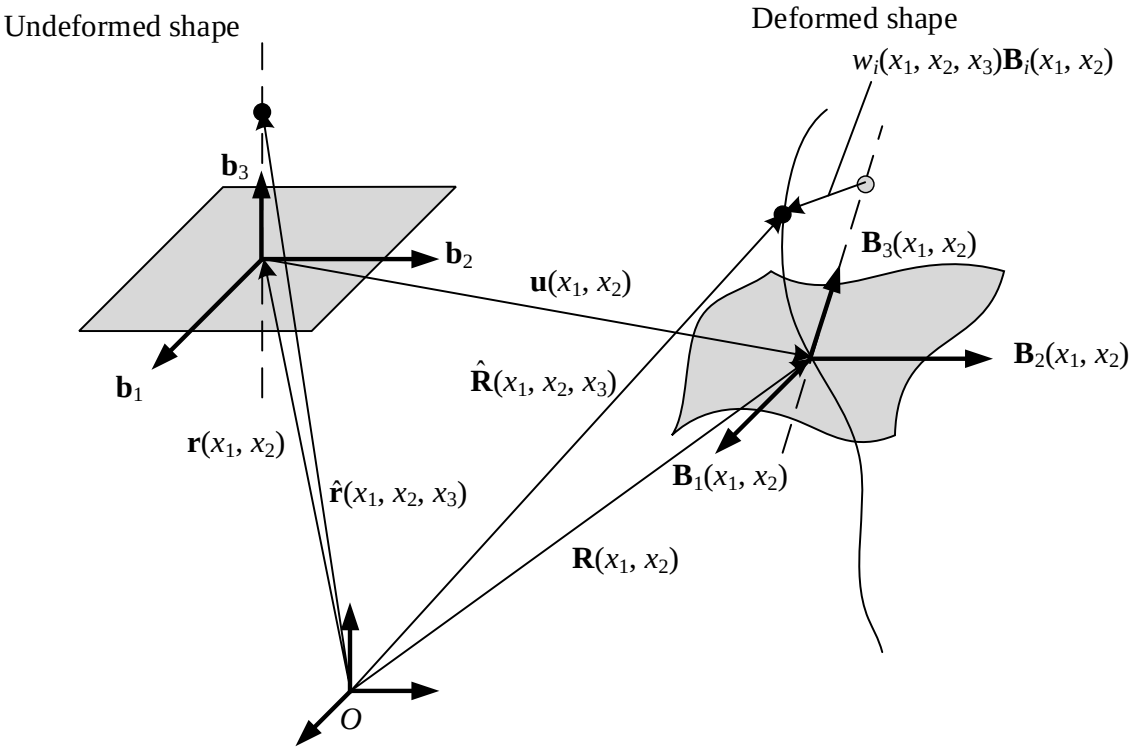

Figure 2.3. Schematic of shell deformation.

The position vector of a point in a shell can be determined by its curvilinear coordinates x_i, as shown in Figure 2.3, where x_α are two arbitrary coordinates in the reference surface and x_3 is the normal coordinate. Based on the concept of MSG, micro coordinate $y_3 = x_3/\varepsilon$ can be introduced. Without loss of generality, x_α can be chosen as the line of curvature, in which case x_i will be orthogonal, so that formulation can be simplified. Denoting the normal vector of the reference surface as $\mathbf{b}_3$, which is also the base vector of coordinate x_3, and the position vector of a point on the reference surface as $\mathbf{r}$, the position vector of any material point in the shell structure $\hat{\mathbf{r}}$ can be expressed as

$$\hat{\mathbf{r}}\left(x_1, x_2, y_3\right) = \mathbf{r}\left(x_1, x_2\right) + \varepsilon y_3 \mathbf{b}_3 \tag{2.2}$$

The vector $\mathbf{r}$ represents the intersection point between the reference surface and the normal line on which the described point is located. When taking the middle surface as the reference surface, averaging both sides of Eq. (2.2) gives

$$\left\langle\left\langle \hat{\mathbf{r}}\left(x_1, x_2, y_3\right)\right\rangle\right\rangle = \mathbf{r}\left(x_1, x_2\right) \tag{2.3}$$

where $\langle\langle\ \rangle\rangle$ indicates average over the SG. In this case, $\mathbf{r}$ also represents the through-the-thickness average of $\hat{\mathbf{r}}$. It is noted that we are free to choose any surface, not necessarily the middle surface, as the reference surface. However, if the reference surface is not the middle surface, $\mathbf{r}$ is not the through-the-thickness average of $\hat{\mathbf{r}}$.

The base vectors of coordinate x_α are defined as the tangent vectors

$$\mathbf{a}_\alpha\left(x_1, x_2\right) = \mathbf{r}_{,\alpha} \tag{2.4}$$

Then, Lamé parameters of the reference surface can be obtained as

$$A_\alpha\left(x_1, x_2\right) = \sqrt{\mathbf{a}_{\underline{\alpha}} \cdot \mathbf{a}_{\underline{\alpha}}} \tag{2.5}$$

These parameters can be interpreted as distance measurements on the corresponding directions of the surface. Using A_α, unit vectors in the tangent direction can be introduced as

$$\mathbf{b}_\alpha = \frac{\mathbf{a}_{\underline{\alpha}}}{A_{\underline{\alpha}}} \tag{2.6}$$

Obviously, $\mathbf{b}_i$ form an orthonormal triad, satisfying

$$\mathbf{b}_3 = \mathbf{b}_1 \times \mathbf{b}_2 = \frac{\mathbf{a}_1 \times \mathbf{a}_2}{|\mathbf{a}_1 \times \mathbf{a}_2|} \tag{2.7}$$

Using the surface tangent and normal vectors, covariant base vector $\mathbf{g}_i = \frac{\partial \hat{\mathbf{r}}}{\partial x_i}$ of the 3D shell body can be defined as

$$\begin{aligned} \mathbf{g}_1 &= \mathbf{a}_1 + \varepsilon y_3 \mathbf{b}_{3,1} \\ \mathbf{g}_2 &= \mathbf{a}_2 + \varepsilon y_3 \mathbf{b}_{3,2} \\ \mathbf{g}_3 &= \mathbf{b}_3 \end{aligned} \tag{2.8}$$

Partial derivatives of the normal $\mathbf{b}_3$ can be obtained based on the differential geometry of surface, so that

$$\mathbf{b}_{3,\alpha} = A_{\underline{\alpha}} k_{\underline{\alpha}\beta} \mathbf{b}_\beta \tag{2.9}$$

where $k_{\alpha\beta}$ represents the out-of-plane curvatures of the surface. Since coordinates x_α are chosen to be the lines of curvatures, $k_{12} = k_{21} = 0$. Substituting Eq. (2.9) back into Eq. (2.8) gives

$$\begin{aligned} \mathbf{g}_1 &= A_1 \left(1 + \varepsilon y_3 k_{11}\right) \mathbf{b}_1 \\ \mathbf{g}_2 &= A_2 \left(1 + \varepsilon y_3 k_{22}\right) \mathbf{b}_2 \\ \mathbf{g}_3 &= \mathbf{b}_3 \end{aligned} \tag{2.10}$$

The contravariant base vectors $\mathbf{g}^i$ can be calculated using the relation

$$\mathbf{g}^i = \frac{1}{2\sqrt{g}} \mathrm{e}_{ijk} \mathbf{g}_j \times \mathbf{g}_k \tag{2.11}$$

where

$$g = \det\left(\mathbf{g}_i \cdot \mathbf{g}_j\right) \tag{2.12}$$

resulting in

$$\begin{aligned}
\mathbf{g}^1 &= \frac{\mathbf{b}_1}{A_1\left(1+\varepsilon y_3 k_{11}\right)} \\
\mathbf{g}^2 &= \frac{\mathbf{b}_2}{A_2\left(1+\varepsilon y_3 k_{22}\right)} \\
\mathbf{g}^3 &= \mathbf{b}_3
\end{aligned} \tag{2.13}$$

When deformation happens, the material point described by vector $\hat{\mathbf{r}}$ in the undeformed state will have the position vector $\hat{\mathbf{R}}$ in the deformed state. Every material point in the undeformed state will have a corresponding position vector in the deformed shape. Similar to the undeformed state, orthonormal vector triad for the deformed state $\mathbf{B}_i$ is introduced. Relation between $\mathbf{b}_i$ and $\mathbf{B}_i$ is expressed using the direction cosine matrix $\mathcal{C}\left(x_1, x_2\right)$

$$\begin{aligned}
\mathbf{B}_i &= \mathcal{C}_{ij}\mathbf{b}_j \\
\mathcal{C}_{ij} &= \mathbf{B}_i \cdot \mathbf{b}_j
\end{aligned} \tag{2.14}$$

so that $\mathbf{B}_i$ and $\mathbf{b}_i$ are identical when the shell is undeformed. However, after rotation, $\mathbf{B}_\alpha$ are not necessarily tangential to the deformed shell reference surface. For a general SG, in adddition to y_3, micro coordinates $y_\alpha = x_\alpha/\varepsilon$ can also be introduced. Similar to Eq. (2.2), expanding $\hat{\mathbf{R}}$ based on $\mathbf{B}_i$ gives

$$\hat{\mathbf{R}}\left(x_\alpha, y_i\right) = \mathbf{R}\left(x_\alpha\right) + \varepsilon y_3 \mathbf{B}_3\left(x_\alpha\right) + \varepsilon w_i\left(x_\alpha, y_i\right)\mathbf{B}_i\left(x_\alpha\right) \tag{2.15}$$

where w_i are fluctuating functions to ensure Eq. (2.15) to be able to describe all possible deformation. No assumption is made on the shape of fluctuating functions and their exact expressions will be determined by MSG later. Unlike $\mathbf{b}_i$, $\mathbf{B}_i$ is not clearly defined due to the arbitrariness of the rotation, thus, Eq. (2.15) does not represent a unique mapping for every

point unless six more constraints are introduced. For the first three constraints, it would be convenient to set $\mathbf{R}$ to be the average of $\hat{\mathbf{R}}$ over the SG, which means

$$\left\langle\left\langle \hat{\mathbf{R}} \right\rangle\right\rangle = \mathbf{R} \tag{2.16}$$

In this way, the constraints should be

$$\langle\langle w_i \left(x_\alpha, y_i\right)\rangle\rangle = 0 \tag{2.17}$$

Before introducing the other three constraints, strains should be defined first. Defining the covariant base vectors in the deformed state as

$$\mathbf{G}_i = \frac{\partial \hat{\mathbf{R}}}{\partial x_i} \tag{2.18}$$

then the deformation gradient tensor $\mathbf{F}$ is defined as

$$\mathbf{F} = \hat{\mathbf{R}} \nabla = \frac{\partial \hat{\mathbf{R}}}{\partial x_i} \mathbf{g}^i = \mathbf{G}_i \mathbf{g}^i \tag{2.19}$$

Resolving the deformation gradient tensor along the mixed bases [105], that is

$$\mathbf{F} = F_{ij} \mathbf{B}_i \mathbf{b}_j \tag{2.20}$$

gives

$$F_{ij} = \mathbf{B}_i \cdot \mathbf{G}_k \mathbf{g}^k \cdot \mathbf{b}_j \tag{2.21}$$

Based on Eq. (2.14), introducing a global rotation tensor $\mathbf{C}^{bB}$, such that

$$\mathbf{C}^{bB} = \mathbf{b}_i \mathbf{B}_i = \mathcal{C}_{ij} \mathbf{b}_i \mathbf{b}_j \tag{2.22}$$

then for small local rotations, the 3D Jauman-Biot-Cauchy strain tensor $\mathbf{\Gamma}$ can be written as

$$\mathbf{\Gamma} = \frac{1}{2} \left(\mathbf{C}^{bB} \cdot \mathbf{F} + \mathbf{F}^{\mathrm{T}} \cdot \left(\mathbf{C}^{bB} \right)^{\mathrm{T}} \right) - \mathbf{\Delta} \tag{2.23}$$

where $\mathbf{\Delta}$ is the identity tensor. Eq. (2.23) can be written in the component form in undeformed state, gives

$$\Gamma_{ij} = \frac{1}{2}(F_{ij} + F_{ji}) - \delta_{ij} \tag{2.24}$$

where δ_{ij} is the Kronecker symbol. For expressing the 3D strains in terms of 2D strains, one can define 2D generalized strains as [31], [106]

$$\mathbf{R}_{,\alpha} = A_{\underline{\alpha}} \left(\mathbf{B}_{\underline{\alpha}} + \varepsilon_{\underline{\alpha}\beta} \mathbf{B}_{\beta} \right) \tag{2.25}$$

$$\mathbf{B}_{3,\alpha} = A_{\underline{\alpha}} \left(k_{\underline{\alpha}\beta} + \kappa_{\underline{\alpha}\beta} \right) \mathbf{B}_{\beta} \tag{2.26}$$

$$\mathbf{B}_{\alpha,\beta} = A_{\underline{\beta}} \left[- \left(k_{\underline{\beta}2} + \kappa_{\underline{\beta}2} \right) \mathbf{B}_1 + \left(k_{\underline{\beta}1} + \kappa_{\underline{\beta}1} \right) \mathbf{B}_2 + \left(k_{\underline{\beta}3} + \kappa_{\underline{\beta}3} \right) \mathbf{B}_3 \right] \times \mathbf{B}_{\alpha} \tag{2.27}$$

where $\varepsilon_{\alpha\beta}$ and $\kappa_{\alpha\beta}$ are 2D generalized membrane strains and curvatures. $k_{\alpha 3}$ can be expressed in terms of Lamé parameters as

$$k_{13} = -\frac{A_{1,2}}{A_1 A_2} \qquad k_{23} = \frac{A_{2,1}}{A_1 A_2} \tag{2.28}$$

Although components $\kappa_{\alpha 3}$ appears in Eq. (2.27), they will not appear in the expression of 3D strains as long as the fluctuating functions are small. From Eq. (2.25), three more constraints can be introduced. The first two limit the direction of vector $\mathbf{B}_3$, so that it is normal to the deformed reference surface

$$\frac{\mathbf{R}_{,\underline{\alpha}} \cdot \mathbf{B}_3}{A_{\underline{\alpha}}} = 0 \tag{2.29}$$

It should be noted that these two constraints do not mean that transverse shear deformation is not allowed, because the transverse shear deformation can be captured by the fluctuating functions. The last constraint can be introduced as

$$\frac{\mathbf{B}_1 \cdot \mathbf{R}_{,2}}{A_2} = \frac{\mathbf{B}_2 \cdot \mathbf{R}_{,1}}{A_1} \tag{2.30}$$

so that $\varepsilon_{12} = \varepsilon_{21}$.

Considering strains are small compared with unity and fluctuating functions are of similar magnitude of strains, then using Eq. (2.13), (2.21), and (2.24) – (2.27), 3D strain fields can be expressed in terms of 2D strains and fluctuating functions as

$$
\begin{aligned}
\Gamma_{11} =& \frac{\varepsilon_{11} + \varepsilon y_3 \kappa_{11} + \left(\varepsilon w_{1,1} + w_{1|1}\right)/A_1 + \varepsilon w_3 k_{11} - \varepsilon w_2 k_{13}}{1 + \varepsilon y_3 k_{11}} \\
2\Gamma_{12} =& \frac{\varepsilon_{21} + \varepsilon y_3 \kappa_{21} + \left(\varepsilon w_{1,2} + w_{1|2}\right)/A_2 - \varepsilon w_2 k_{23}}{1 + \varepsilon y_3 k_{22}} \\
&+ \frac{\varepsilon_{12} + \varepsilon y_3 \kappa_{12} + \left(\varepsilon w_{2,1} + w_{2|1}\right)/A_1 + \varepsilon w_1 k_{13}}{1 + \varepsilon y_3 k_{11}} \\
\Gamma_{22} =& \frac{\varepsilon_{22} + \varepsilon y_3 \kappa_{22} + \left(\varepsilon w_{2,2} + w_{2|2}\right)/A_2 + \varepsilon w_3 k_{22} + \varepsilon w_1 k_{23}}{1 + \varepsilon y_3 k_{22}} \\
2\Gamma_{13} =& w_{1|3} + \frac{\left(\varepsilon w_{3,1} + w_{3|1}\right)/A_1 - \varepsilon w_1 k_{11}}{1 + \varepsilon y_3 k_{11}} \\
2\Gamma_{23} =& w_{2|3} + \frac{\left(\varepsilon w_{3,2} + w_{3|2}\right)/A_2 - \varepsilon w_2 k_{22}}{1 + \varepsilon y_3 k_{22}} \\
\Gamma_{33} =& w_{3|3}
\end{aligned}
\tag{2.31}
$$

Although Eq. (2.31) is directly derived from the definition of 2D and 3D strains, due to its complexity, it is not convenient to be used for deriving the shell constitutive model relating 2D strains and sectional forces and moments. Consequently, it is necessary to introduce approximations to simplify the formulation. Following [34], [36], this model considers shells with moderate thickness, i.e. $h/R \sim 10^{-1}$ and $R > l^2/h$. Based on these assumptions, terms of the order h^2/R^2, h^2/lR, h^3/l^3 and higher will be dropped. Energy introduced by h/R terms are considered geometric corrections, and h/l and h^2/l^2 terms are transverse shear corrections. Furthermore, geometry of the shell is assumed to be constant or slowly varying, so that derivatives of $k_{\alpha\beta}$ and A_α with respect to surface coordinates can be neglected. Though in current formulation κ_{12} does not necessarily equal to κ_{21}, it has been proved that their difference only contribute to the order of h^2/R^2 or $\varepsilon h^3/l^2/R$ [107], which means within the current approximation $\kappa_{12} = \kappa_{21}$. Based on the above approximation, and expanding

$$
\frac{1}{1 + \varepsilon y_3 k_{\alpha\beta}} = 1 - \varepsilon y_3 k_{\alpha\beta} + O\left(\frac{h^2}{R^2}\right) \tag{2.32}
$$

Eq. (2.31) can be simplified to written in a matrix form as

$$\Gamma = \Gamma_h w + \Gamma_\epsilon \epsilon + \varepsilon \Gamma_{Rh} w + \varepsilon \Gamma_{R\epsilon} \epsilon + \varepsilon \Gamma_{l1} w_{;1} + \varepsilon \Gamma_{l2} w_{;2} \tag{2.33}$$

where

$$\Gamma = \begin{bmatrix} \Gamma_{11} & \Gamma_{22} & \Gamma_{33} & 2\Gamma_{23} & 2\Gamma_{13} & 2\Gamma_{12} \end{bmatrix}^{\mathrm{T}} \tag{2.34}$$

$$w = \begin{bmatrix} w_1 & w_2 & w_3 \end{bmatrix}^{\mathrm{T}} \tag{2.35}$$

$$\epsilon = \begin{bmatrix} \varepsilon_{11} & \varepsilon_{22} & 2\varepsilon_{12} & \kappa_{11} & \kappa_{22} & \kappa_{12} + \kappa_{21} \end{bmatrix}^{\mathrm{T}} \tag{2.36}$$

and $(\ )_{;\alpha} = (\partial/\partial x_\alpha)\,(1/A_\alpha)$. Γ_h is an operator matrix for calculating derivatives with respect to the micro coordinates which depend on the dimension of the SG. For a 3D SG, it is

$$\Gamma_h = \begin{bmatrix} \frac{1}{A_1}\frac{\partial}{\partial y_1} & 0 & 0 \\ 0 & \frac{1}{A_2}\frac{\partial}{\partial y_2} & 0 \\ 0 & 0 & \frac{\partial}{\partial y_3} \\ 0 & \frac{\partial}{\partial y_3} & \frac{1}{A_2}\frac{\partial}{\partial y_2} \\ \frac{\partial}{\partial y_3} & 0 & \frac{1}{A_1}\frac{\partial}{\partial y_1} \\ \frac{1}{A_2}\frac{\partial}{\partial y_2} & \frac{1}{A_1}\frac{\partial}{\partial y_1} & 0 \end{bmatrix} \tag{2.37}$$

If the SG has a lower dimension, Γ_h can be obtained by vanishing components having the micro coordinates not used for the SG. Notice that for a shell structure y_3 will never be vanished. Γ_ϵ is an operator matrix associated with 2D strains and curvatures

$$\Gamma_\epsilon = \begin{bmatrix} 1 & 0 & 0 & \varepsilon y_3 & 0 & 0 \\ 0 & 1 & 0 & 0 & \varepsilon y_3 & 0 \\ 0 & 0 & 0 & 0 & 0 & 0 \\ 0 & 0 & 0 & 0 & 0 & 0 \\ 0 & 0 & 0 & 0 & 0 & 0 \\ 0 & 0 & 1 & 0 & 0 & \varepsilon y_3 \end{bmatrix} \tag{2.38}$$

Γ_{Rh} and $\Gamma_{R\epsilon}$ are operators introduced by the initial curvatures

$$\Gamma_{Rh} = \begin{bmatrix} 0 & 0 & k_{11} \\ 0 & 0 & k_{22} \\ 0 & 0 & 0 \\ 0 & -k_{22} & 0 \\ -k_{11} & 0 & 0 \\ 0 & 0 & 0 \end{bmatrix} \tag{2.39}$$

$$\Gamma_{R\epsilon} = -y_3 \begin{bmatrix} k_{11} & 0 & 0 & \varepsilon y_3 k_{11} & 0 & 0 \\ 0 & k_{22} & 0 & 0 & \varepsilon y_3 k_{22} & 0 \\ 0 & 0 & 0 & 0 & 0 & 0 \\ 0 & 0 & 0 & 0 & 0 & 0 \\ 0 & 0 & 0 & 0 & 0 & 0 \\ 0 & 0 & \frac{k_{11}+k_{22}}{2} & 0 & 0 & \varepsilon y_3 \frac{k_{11}+k_{22}}{2} \end{bmatrix} \tag{2.40}$$

Γ_{l1} and Γ_{l2} are operators for introducing the contribution of partial derivatives with respect to macro coordinates x_α of the fluctuating functions to the 3D strains

$$\Gamma_{l1} = \begin{bmatrix} 1 & 0 & 0 \\ 0 & 0 & 0 \\ 0 & 0 & 0 \\ 0 & 0 & 0 \\ 0 & 0 & 1 \\ 0 & 1 & 0 \end{bmatrix} \qquad \Gamma_{l2} = \begin{bmatrix} 0 & 0 & 0 \\ 0 & 1 & 0 \\ 0 & 0 & 0 \\ 0 & 0 & 1 \\ 0 & 0 & 0 \\ 1 & 0 & 0 \end{bmatrix} \tag{2.41}$$

Notice that in Eq. (2.33), all the terms with the small parameter ε have the order of either h/R or h/l, so they are higher-order terms compared with the terms without ε. Up to this point, we have completely formulated the kinematics of a shell.

2.3 MSG-based Classical Shell Theory

To construct a 2D shell model, we need to formulate the energy of the shell first. The strain energy of a shell can be expressed as

$$\mathcal{J} = \frac{1}{2}\int_{\mathcal{V}} (\mathbf{\Gamma} : \mathbf{C} : \mathbf{\Gamma})\, \mathbf{g}_1 \times \mathbf{g}_2 \cdot \mathbf{g}_3 \mathrm{d}x_1 \mathrm{d}x_2 \mathrm{d}x_3 \tag{2.42}$$

where $\mathcal{V}$ is the volume of the 3D shell body, and $\mathbf{C}$ is the fourth-order material stiffness tensor. The strain energy can be written in terms of areal energy density, such that

$$\mathcal{J} = \int_{\Omega} \frac{1}{\omega} U \mathrm{d}\Omega \tag{2.43}$$

where Ω represents the reference surface. Then,

$$U = \left\langle \rho \left(\frac{1}{2} \Gamma^{\mathrm{T}} D \Gamma \right) \right\rangle \tag{2.44}$$

with

$$\rho = \frac{\mathbf{g}_1 \times \mathbf{g}_2 \cdot \mathbf{g}_3}{|\mathbf{a}_1 \times \mathbf{a}_2|} = 1 + \varepsilon y_3 \left(k_{11} + k_{22} \right) + O\left(\frac{h^2}{R^2} \right) \tag{2.45}$$

where D is the 6×6 material stiffness matrix comes from tensor $\mathbf{C}$. Angle bracket denotes integral over the domain of the SG. ω represents the area occupied by y_α coordinates in the SG. When the SG is 2D with one of y_α disappears, it becomes the length. When the SG is 1D, it is equal to 1.

When external loads are applied on the shell, we also need to calculate virtual work of applied loads. When the shell is applied with body force $\mathbf{P} = P_i \mathbf{B}_i$, tractions on the top and bottom surfaces $\boldsymbol{\tau} = \tau_i \mathbf{B}_i$ and $\boldsymbol{\beta} = \beta_i \mathbf{B}_i$, respectively, the virtual work in the shell due to applied loads can be calculated as

$$\overline{\delta W} = \frac{1}{\omega} \left(\left\langle \mathbf{P} \cdot \delta \hat{\mathbf{R}} \right\rangle + \boldsymbol{\tau} \cdot \delta \hat{\mathbf{R}}^{+} + \boldsymbol{\beta} \cdot \delta \hat{\mathbf{R}}^{-} \right) \tag{2.46}$$

where + and − in superscript denote evaluation at the top and bottom surface, respectively. $\delta\hat{\mathbf{R}}$ is the virtual displacement, which can be derived by taking the variation of equation (2.15), such that

$$\delta\hat{\mathbf{R}} = \delta\mathbf{R} + \varepsilon y_3 \delta\mathbf{B}_3 + \varepsilon\delta w_i \mathbf{B}_i + \varepsilon w_i \delta\mathbf{B}_i \tag{2.47}$$

In a similar way as the definition of 2D strains, the virtual displacement of the reference surface can be defined as

$$\delta\mathbf{R} = \overline{\delta q_i}\mathbf{B}_i \tag{2.48}$$

and the virtual rotation is defined as

$$\delta\mathbf{B}_i = \left(-\overline{\delta\psi}_\beta \mathbf{B}_\beta \times \mathbf{B}_3 + \overline{\delta\psi}_3 \mathbf{B}_3\right) \times \mathbf{B}_i \tag{2.49}$$

where $\overline{\delta q_i}$ and $\overline{\delta\psi}_i$ are the virtual displacement and rotation components in the $\mathbf{B}_i$ bases respectively. Substitute Eq. (2.48) and (2.49) into Eq. (2.47), then into Eq. (2.46) gives

$$\overline{\delta W} = \frac{1}{\omega}\left[f_i \overline{\delta q_i} + m_\alpha \overline{\delta\psi}_\alpha + \varepsilon\delta\left(\langle P_i w_i\rangle + \tau_i {w_i}^+ + \beta_i {w_i}^-\right)\right] \tag{2.50}$$

where f_i and m_α are distributed forces and moments defined as

$$\begin{aligned} f_i &= \langle P_i\rangle + \tau_i + \beta_i \\ m_\alpha &= \langle \varepsilon y_3 P_\alpha\rangle + \frac{h}{2}(\tau_\alpha - \beta_\alpha) \end{aligned} \tag{2.51}$$

For the purpose of constructing a shell model, only fluctuating functions w_i are treated as unknown variables, as virtual displacements and rotations will be handled by the global shell analysis. As a result, the total potential energy can be formed as

$$\Pi = U - W \tag{2.52}$$

where

$$W = \varepsilon\left(\langle P_i w_i\rangle + \tau_i {w_i}^+ + \beta_i {w_i}^-\right) \tag{2.53}$$

Then the shell model can be obtained through minimizing the total potential

$$\delta\Pi = 0 \tag{2.54}$$

Solving Eq. (2.54) directly would have a similar difficulty as solving a 3D problem. To avoid this difficulty, the problem is solved asymptotically based on VAM. To do so, FEM is used to discretize the SG, so that the fluctuating functions can be expressed as

$$w\left(x_\alpha, y_i\right) = S\left(y_i\right) V\left(x_\alpha\right) \tag{2.55}$$

where S is the shape function depending on the type of element, and V is the nodal value, determined by 2D strains at coordinates x_α.

To obtain a classical shell model, all higher order terms compared to unity in the total potential function can be dropped, such that

$$2\Pi_0 = V^{\mathrm{T}} E V + 2V^{\mathrm{T}} D_{h\epsilon}\epsilon + \epsilon^{\mathrm{T}} D_{\epsilon\epsilon}\epsilon \tag{2.56}$$

where

$$\begin{aligned} E &= \left\langle \left(\Gamma_h S\right)^{\mathrm{T}} D \left(\Gamma_h S\right) \right\rangle \\ D_{h\epsilon} &= \left\langle \left(\Gamma_h S\right)^{\mathrm{T}} D \Gamma_\epsilon \right\rangle \\ D_{\epsilon\epsilon} &= \left\langle \Gamma_\epsilon^{\mathrm{T}} D \Gamma_\epsilon \right\rangle \end{aligned} \tag{2.57}$$

Minimizing Π_0 in Eq. (2.56) subject to the constraints in Eq. (2.17), a linear system can be obtained as

$$EV = -D_{h\epsilon}\epsilon \tag{2.58}$$

It is clear that V can be solved from Eq. (2.58) as a linear function of ϵ, giving

$$V = \hat{V}_0 \epsilon \tag{2.59}$$

Substituting Eq. (2.59) back into Eq. (2.56), the total potential in the SG can be obtained as

$$2\Pi_0 = \epsilon^{\mathrm{T}} \left(\hat{V}_0^{\mathrm{T}} D_{h\epsilon} + D_{\epsilon\epsilon} \right) \epsilon = \omega \epsilon^{\mathrm{T}} A \epsilon \tag{2.60}$$

where A is the effective stiffness matrix of the shell. For a classical shell model, A is equivalent to the 6×6 ABD matrix, which can be fully populated, so it can be used as the sectional stiffness matrix of shell elements in finite element analysis for predicting the global behavior. With ϵ obtained from the global shell analysis, fluctuating functions can be written as

$$w = S \hat{V}_0 \epsilon \tag{2.61}$$

Then components in the undeformed base $\mathbf{b}_i$ of the local displacement field $\mathbf{U} = \hat{\mathbf{R}} - \hat{\mathbf{r}}$ can be calculated as

$$U_i = u_i + \varepsilon y_3 (\mathcal{C}_{3i} - \delta_{3i}) + \varepsilon w_j \mathcal{C}_{ji} \tag{2.62}$$

where u_i are the components in the undeformed base of global displacement $\mathbf{u} = \mathbf{R} - \mathbf{r}$. 3D strain field can be recovered by neglecting terms with ε in Eq. (2.33), gives

$$\Gamma^0 = \left(\Gamma_h S \hat{V}_0 + \Gamma_\epsilon \right) \epsilon \tag{2.63}$$

and 3D stress field can be calculated using the Hooke's law as

$$\sigma = D \Gamma^0 \tag{2.64}$$

where

$$\sigma = \begin{bmatrix} \sigma_{11} & \sigma_{22} & \sigma_{33} & \sigma_{23} & \sigma_{13} & \sigma_{12} \end{bmatrix}^{\mathrm{T}} \tag{2.65}$$

2.4 MSG-based Classical Shell for Nonlinear Analysis

The MSG-based shell theory can be applied to nonlinear analysis with both physical and geometrical nonlinearities, as the kinematics in Section 2.2 is geometrically exact. In this section, an implicit algorithm for nonlinear shell modeling is presented. For demonstrating

the algorithm, formulation in this section considers 1D SG only. Also, even though in nonlinear analyses strains are larger than those in linear analyses, in most of the cases they are still small compared with unity, so coupling terms between 2D strains and fluctuating functions are still neglected in 3D strain fields. Based on these considerations, leading terms of the 3D strain fields in Eq. (2.33) can be expressed as

$$\Gamma = \Gamma_h w + \Gamma_\epsilon \epsilon \tag{2.66}$$

For 1D SG, Γ_h is simplified to be

$$\Gamma_h = \begin{bmatrix} 0 & 0 & 0 \\ 0 & 0 & 0 \\ 0 & 0 & \frac{\partial}{\partial y_3} \\ 0 & \frac{\partial}{\partial y_3} & 0 \\ \frac{\partial}{\partial y_3} & 0 & 0 \\ 0 & 0 & 0 \end{bmatrix} \tag{2.67}$$

Define a state function $\mathcal{W}$ as

$$\mathcal{W}\left(\dot{\Gamma}_{ij}\right) = \frac{1}{2}\dot{\Gamma}_{ij} C^{alg}_{ijkl} \dot{\Gamma}_{kl} \tag{2.68}$$

where C^{alg}_{ijkl} is the tangent stiffness of the material. Then, the variational statement for this problem can be described as: among all the admissible strain rates, the actual strain rates should minimize the functional

$$U = \langle \mathcal{W} \rangle \tag{2.69}$$

so that

$$\delta U = \langle \delta \mathcal{W} \rangle = \left\langle \frac{\partial \mathcal{W}}{\partial \dot{\Gamma}_{ij}} \delta \dot{\Gamma}_{ij} \right\rangle = \left\langle \dot{\sigma}_{ij} \delta \dot{\Gamma}_{ij} \right\rangle = 0 \tag{2.70}$$

in which only the fluctuating functions are varied, and subject to the constraints in Eq. (2.17). To solve the problem, the 1D SG is discretized using finite elements, so that the fluctuating functions can be expressed as

$$w\left(x_\alpha, y_3\right) = S\left(y_3\right) V\left(x_\alpha\right) \tag{2.71}$$

The Newton-Raphson method can be applied to solve the problem with 2D strain ϵ been held fixed and V being the variable. However, using the Newton-Raphson method directly may result in convergence issues, especially when the initial point is far from the solution. To overcome this, an Euler prediction step can be added prior to the Newton-Raphson step, which means the loading process is firstly proceeded in the tangent direction of the loading path, then correction is calculated to obtain the solution. The Euler step obtains the increments of 3D variables at the beginning of the current loading step, so that the following Newton-Raphson step can have a better convergence to the final solution. Substituting Eq. (2.66) and (2.71) into Eq. (2.69) gives

$$U = \frac{1}{2}\left(\dot{V}^{\mathrm{T}} E \dot{V} + 2\dot{V}^{\mathrm{T}} D_{h\epsilon}\dot{\epsilon} + \dot{\epsilon}^{\mathrm{T}} D_{\epsilon\epsilon}\dot{\epsilon}\right) \tag{2.72}$$

where $D_{h\epsilon}$, $D_{\epsilon\epsilon}$ and E have the same expression in Eq. (2.57), with D being the 6×6 matrix form of the tangent stiffness C^{alg}_{ijkl}. Following the same way in last section, minimizing U in Eq. (2.72) gives

$$\dot{V} = \hat{V}_0\dot{\epsilon} \tag{2.73}$$

3D strain fields can be recovered using Eq. (2.73) as

$$\dot{\Gamma} = \Gamma_\epsilon\dot{\epsilon} + \Gamma_h S\hat{V}_0\dot{\epsilon} \tag{2.74}$$

Written in an incremental form gives

$$\Delta\Gamma = \Gamma_\epsilon\Delta\epsilon + \Gamma_h S\hat{V}_0\Delta\epsilon \tag{2.75}$$

Substituting Eq. (2.73) back into Eq. (2.72) gives

$$U = \frac{1}{2}\dot{\epsilon}^{\mathrm{T}} A \dot{\epsilon} \tag{2.76}$$

where A is the current effective stiffness matrix of the shell having the same expression as Eq. (2.60). By definition, sectional force and moment N can be calculated as

$$\dot{N} = \frac{\partial}{\partial \dot{\epsilon}} \langle \mathcal{W} \rangle = A \dot{\epsilon} \tag{2.77}$$

where

$$N = \begin{bmatrix} N_{11} & N_{22} & N_{12} & M_{11} & M_{22} & M_{12} \end{bmatrix}^{\mathrm{T}} \tag{2.78}$$

Based on the result of the Euler step, the Newton-Raphson step can be proceeded. To do so, writing Eq. (2.70) in incremental form

$$\delta U^* = \langle \Delta \sigma_{ij} \delta \left(\Delta \Gamma_{ij} \right) \rangle = 0 \tag{2.79}$$

discretizing Ep. (2.79) gives

$$\begin{aligned} \delta U^* &= \langle \left[\sigma \left(V \right) - \sigma_n \right] \delta \left[\Gamma_h S \left(V - V_n \right) \right] \rangle \\ &= \delta V^{\mathrm{T}} \left\langle \left(\Gamma_h S \right)^{\mathrm{T}} \left[\sigma \left(V \right) - \sigma_n \right] \right\rangle \\ &= 0 \end{aligned} \tag{2.80}$$

where subscript n represent the value at the beginning of the current step. Notice here that the stress σ can be calculated based on the nonlinear material model, and generally $\sigma \neq D\Gamma$. Eq. (2.80) holds only if

$$\Psi \left(V \right) = \left\langle \left(\Gamma_h S \right)^{\mathrm{T}} \left[\sigma \left(V \right) - \sigma_n \right] \right\rangle = 0 \tag{2.81}$$

Suppose the Newton-Raphson loop converged in the previous step, then

$$\left\langle \left(\Gamma_h S \right)^{\mathrm{T}} \sigma_n \right\rangle = 0 \tag{2.82}$$

As a result,

$$\Psi\left(V\right)=\left\langle \left(\Gamma_{h}S\right)^{\mathrm{T}}\sigma\left(V\right)\right\rangle =0 \tag{2.83}$$

To solve Eq. (2.83), it requires that

$$\Psi\left(V_{old}+\mathrm{d}V\right)=\Psi\left(V_{old}\right)+\frac{\partial\Psi}{\partial V}\mathrm{d}V=0 \tag{2.84}$$

where

$$\frac{\partial\Psi}{\partial V}=\left\langle \left(\Gamma_{h}S\right)^{\mathrm{T}}\frac{\partial\sigma}{\partial V}\right\rangle =\left\langle \left(\Gamma_{h}S\right)^{\mathrm{T}}D\left(\Gamma_{h}S\right)\right\rangle =E \tag{2.85}$$

Then using Eq. (2.85), the correction can be computed from Eq. (2.84) and added to the solution, i.e.,

$$V_{new}=V_{old}+\mathrm{d}V \tag{2.86}$$

Resultant sectional force and moment N can be obtained through differentiating U, which gives

$$\begin{aligned}\dot{N}&=\frac{\partial}{\partial\dot{\epsilon}}\left\langle \mathcal{W}\right\rangle =\left\langle \frac{\partial\mathcal{W}}{\partial\dot{\epsilon}}\right\rangle =\left\langle \left(\frac{\partial\dot{\Gamma}}{\partial\dot{\epsilon}}\right)^{\mathrm{T}}\frac{\partial\mathcal{W}}{\partial\dot{\Gamma}}\right\rangle \\&=\left\langle \left(\Gamma_{h}S\frac{\partial V}{\partial\epsilon}+\Gamma_{\epsilon}\right)^{\mathrm{T}}\dot{\sigma}\right\rangle\end{aligned} \tag{2.87}$$

Because of Eq. (2.83), the first term in the bracket of Eq. (2.87) will be zero when multiplied with $\dot{\sigma}$, so that

$$\dot{N}=\left\langle \Gamma_{\epsilon}^{\mathrm{T}}\dot{\sigma}\right\rangle \tag{2.88}$$

then

$$N=\int_{0}^{t}\dot{N}\mathrm{d}t=\left\langle \Gamma_{\epsilon}^{\mathrm{T}}\sigma\right\rangle \tag{2.89}$$

From the expression of the sectional force and moment in Eq. (2.89), a Jacobian defining the relation between 2D strain and sectional force increments can be obtained as

$$\frac{\partial N}{\partial\epsilon}=\frac{\left\langle \Gamma_{\epsilon}^{\mathrm{T}}\partial\sigma\right\rangle }{\partial\epsilon}=\left\langle \Gamma_{\epsilon}^{\mathrm{T}}\frac{\partial\sigma}{\partial\Gamma}\frac{\partial\Gamma}{\partial\epsilon}\right\rangle =\left\langle \Gamma_{\epsilon}^{\mathrm{T}}D\Gamma_{\epsilon}\right\rangle =D_{\epsilon\epsilon} \tag{2.90}$$

With a material model, all the parameters required for a nonlinear shell analysis can be determined. With current 2D strains and their increments as the inputs, one can calculate deformation dependent state variables and the tangent stiffness of the material. Using this stiffness in the above analysis, Jacobian and resultant sectional force of the current loading step can be obtained as outputs for the global shell analysis. Since shells with 2D and 3D SGs can also exhibit nonlinear behavior, the applicability of the present formulation need to be verified.

2.5 Summary

In this chapter, concept of SG and the procedure of MSG-based structure analysis are introduced. A geometric exact kinematics of shell is formulated, with the relation between 3D strains, and 2D strains and curvatures and fluctuating functions written in matrix form. Classical models for elastic and nonlinear material are presented. For elastic materials, total potential is formulated with strain energy and external work, and fluctuating function discretized for solving the problem using FEM. Expressions for recovering 3D fields are provided. For nonlinear analysis, variational statement is given in terms of strain rates. The fluctuating functions are solved by using an Euler step to proceed in the tangent direction first, then using the Newton-Raphson method to calculate the correction. 3D fields are recovered during the iterations.

3. CURING SIMULATION OF COMPOSITES

3.1 Shell Model for Composites Curing

In this section, analytical formulation of MSG-based shell theory with 1D SG is presented based on the kinematics and energy statement in Chapter 2. Since only 1D SG is considered, micro coordinates y_1 and y_2 disappear, and for the convenience of notation, y_3 is written in terms of x_3 as $y_3 = x_3/\varepsilon$, so that y_3 also disappears. In this case, the angle brackets indicating integral over the SG become integral over the thickness. For applying the theory in composites curing, reference surface is changed to the bottom surface with modified constraints on fluctuating functions to handle the contact with the tool, and terms related with non-mechanical strains are introduced so that effect of large temperature change and cure shrinkage can be considered. In addition to a classical model, models with geometric correction and transverse shear are also derived.

3.1.1 Modification on 3D Formulation

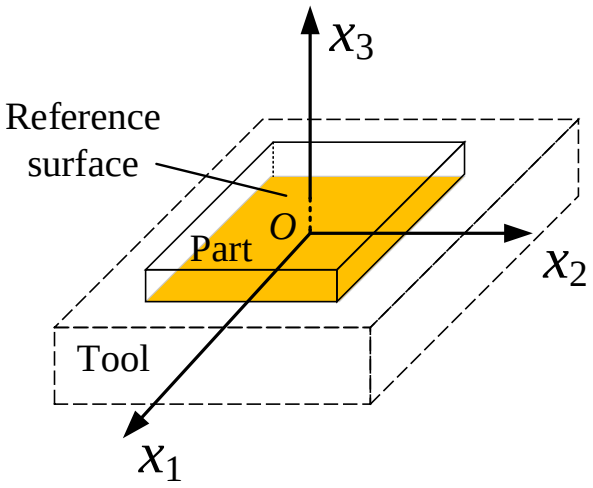

Figure 3.1. Schematic of the part and the tool.

In order to model the contact between the composite part and the tool, it is better to use the bottom surface of the part as the reference surface, since it is on the bottom surface

where the contact is actually happening. As shown in Figure 3.1, origin of the x_3 coordinate is on the reference surface, and to make sure that behavior of the reference surface represents that of the bottom surface of the part, constraints in Eq. (2.17) are modified to be

$$\begin{aligned} w_{\|}^{-}(x_1, x_2, x_3) &= c_{\|} \\ w_3^{-}(x_1, x_2, x_3) &= 0 \end{aligned} \tag{3.1}$$

where $(\ )_{\|} = \lfloor (\ )_1 \quad (\ )_2 \rfloor^{\mathrm{T}}$, and c_α are free variables independent of x_3. They can be determined in by solving an optimization problem later.

In order to derive a model with the transverse shear deformation, an additional term is added to Eq. (2.25) that defines the 2D transverse shear strain $\gamma_{\alpha 3}$

$$\mathbf{R}_{,\alpha} = A_{\underline{\alpha}} \left(\mathbf{B}_{\underline{\alpha}} + \varepsilon_{\underline{\alpha}\beta} \mathbf{B}_\beta + 2\gamma_{\underline{\alpha}3} \mathbf{B}_3 \right) \tag{3.2}$$

This also changes the constraints in Eq. (2.29) to

$$\frac{\mathbf{R}_{,\underline{\alpha}} \cdot \mathbf{B}_3}{A_{\underline{\alpha}}} = 2\gamma_{\alpha 3} \tag{3.3}$$

By adding the transverse shear term, the analytical form of Eq. (2.33) can be written as

$$\begin{aligned} \Gamma_{\mathrm{e}} &= \epsilon + x_3 \kappa + I_\alpha w_{\|;\alpha} + R_{ke} w_3 + x_3 k\epsilon + x_3^2 k\kappa \\ 2\Gamma_s &= \gamma + {w_{\|}}' + \mathrm{e}_\alpha w_{3;\alpha} + R_{ks} w_{\|} \\ \Gamma_{33} &= {w_3}' \end{aligned} \tag{3.4}$$

where $(\ )' = \partial / \partial x_3$, and

$$\begin{aligned} \Gamma_{\mathrm{e}} &= \begin{bmatrix} \Gamma_{11} & 2\Gamma_{12} & \Gamma_{22} \end{bmatrix}^{\mathrm{T}} \\ 2\Gamma_s &= \begin{bmatrix} 2\Gamma_{13} & 2\Gamma_{23} \end{bmatrix}^{\mathrm{T}} \end{aligned} \tag{3.5}$$

and

$$\begin{aligned}\epsilon &= \begin{bmatrix} \varepsilon_{11} & 2\varepsilon_{12} & \varepsilon_{22} \end{bmatrix}^{\mathrm{T}} \\ \kappa &= \begin{bmatrix} \kappa_{11} & \kappa_{12}+\kappa_{21} & \kappa_{22} \end{bmatrix}^{\mathrm{T}} \\ \gamma &= \begin{bmatrix} 2\gamma_{13} & 2\gamma_{23} \end{bmatrix}^{\mathrm{T}}\end{aligned} \tag{3.6}$$

and

$$\begin{aligned} I_1 &= \begin{bmatrix} 1 & 0 \\ 0 & 1 \\ 0 & 0 \end{bmatrix} \qquad I_2 = \begin{bmatrix} 0 & 0 \\ 1 & 0 \\ 0 & 1 \end{bmatrix} \\ \mathrm{e}_1 &= \begin{Bmatrix} 1 \\ 0 \end{Bmatrix} \qquad \mathrm{e}_2 = \begin{Bmatrix} 0 \\ 1 \end{Bmatrix} \end{aligned} \tag{3.7}$$

and

$$\begin{aligned} k &= -\begin{bmatrix} \frac{k_{11}}{1+x_3 k_{11}} & 0 & 0 \\ 0 & \frac{(k_{11}+k_{22})/2}{1+x_3(k_{11}+k_{22})/2} & 0 \\ 0 & 0 & \frac{k_{22}}{1+x_3 k_{22}} \end{bmatrix} \\ R_{k\mathrm{e}} &= \begin{Bmatrix} \frac{k_{11}}{1+x_3 k_{11}} \\ 0 \\ \frac{k_{22}}{1+x_3 k_{22}} \end{Bmatrix} \\ R_{ks} &= -\begin{bmatrix} \frac{k_{11}}{1+x_3 k_{11}} & 0 \\ 0 & \frac{k_{22}}{1+x_3 k_{22}} \end{bmatrix} \end{aligned} \tag{3.8}$$

Particularly, when $A_\alpha = 1$ and $k_{\alpha\beta} = 0$, all parameters in Eq. (3.8) go to zero and the strains in Eq. (3.4) degenerate to those of a plate theory as in [35].

Under large temperature change, material properties will become temperature dependent. Considering a material point with large temperature change and following [108], energy can be written as

$$f\left(\Gamma_{ij},T\right)=f\left(0,T\right)+\Gamma_{ij}\frac{\partial f}{\partial\Gamma_{ij}}\bigg|_{\Gamma_{ij}=0}+\frac{1}{2}\Gamma_{ij}\Gamma_{kl}\frac{\partial^{2}f}{\partial\Gamma_{ij}\partial\Gamma_{kl}}\bigg|_{\Gamma_{ij}=0} \tag{3.9}$$

where T is the temperature. From the relation between energy and stress

$$\sigma_{ij}=\frac{\partial f}{\partial\Gamma_{ij}}=C_{ijkl}\left(T\right)\Gamma_{ij}+l_{ij}\left(T\right) \tag{3.10}$$

where $C_{ijkl}=\frac{\partial^{2}f}{\partial\Gamma_{ij}\partial\Gamma_{kl}}\Big|_{\Gamma_{ij}=0}$ is the fourth-order elasticity tensor and $l_{ij}=\frac{\partial f}{\partial\Gamma_{ij}}\Big|_{\Gamma_{ij}=0}$ is the second-order thermal stress tensor. The corresponding strain-stress relation can be expressed as

$$\Gamma_{ij}=S_{ijkl}\sigma_{kl}-S_{ijkl}l_{kl}=S_{ijkl}\sigma_{kl}+m_{ij} \tag{3.11}$$

where S_{ijkl} is the fourth-order compliance tensor, m_{ij} is the second-order thermal strain tensor. The coefficients of thermal expansion (CTEs) α_{ij} can be defined as

$$\alpha_{ij}=\frac{\partial\Gamma_{ij}}{\partial T}\bigg|_{\sigma_{ij}=\text{constant}}=\frac{\partial S_{ijkl}}{\partial T}\sigma_{kl}+\frac{\partial m_{ij}}{\partial T} \tag{3.12}$$

so that

$$\alpha_{ij}\left(0,T\right)=\frac{\partial m_{ij}}{\partial T} \tag{3.13}$$

Performing integration of the above equation, we obtain

$$m_{ij}=\int_{T_{0}}^{T}\alpha_{ij}\left(0,\theta\right)\mathrm{d}\theta+m_{ij}\left(0,T_{0}\right) \tag{3.14}$$

Note that in Eq. (3.14) the CTEs should be the stress-free coefficients depending on the temperature. $m_{ij}\left(0,T_{0}\right)$ corresponds to the stress-free thermal strain at the reference temperature T_{0}. By defining

$$\breve{\alpha}_{ij}=\frac{1}{T-T_{0}}\int_{T_{0}}^{T}\alpha_{ij}\left(0,\theta\right)\mathrm{d}\theta \tag{3.15}$$

as the secant CTEs, Eq. (3.14) can be rewritten as

$$m_{ij} = \breve{\alpha}_{ij} \left(T - T_0\right) + m_{ij} \left(0, T_0\right) \tag{3.16}$$

By adding non-mechanical strain, including thermal strain and cure shrinkage, into the energy density, and if the material is monoclinic, Eq. (2.44) becomes

$$\begin{aligned} U = \Bigg\langle \rho \Bigg(& \frac{1}{2} \begin{Bmatrix} \Gamma_{\mathrm{e}} \\ 2\Gamma_s \\ \Gamma_{33} \end{Bmatrix}^{\mathrm{T}} \begin{bmatrix} C_{\mathrm{e}} & 0 & C_{\mathrm{et}} \\ 0 & C_s & 0 \\ C_{\mathrm{et}}^{\mathrm{T}} & 0 & C_{33} \end{bmatrix} \begin{Bmatrix} \Gamma_{\mathrm{e}} \\ 2\Gamma_s \\ \Gamma_{33} \end{Bmatrix} \\ & - \begin{Bmatrix} \Gamma_{\mathrm{e}} \\ 2\Gamma_s \\ \Gamma_{33} \end{Bmatrix}^{\mathrm{T}} \begin{bmatrix} C_{\mathrm{e}} & 0 & C_{\mathrm{et}} \\ 0 & C_s & 0 \\ C_{\mathrm{et}}^{\mathrm{T}} & 0 & C_{33} \end{bmatrix} \begin{Bmatrix} \Gamma_{\mathrm{e}}^R \\ 2\Gamma_s^R \\ \Gamma_{33}^R \end{Bmatrix} \Bigg) \Bigg\rangle \end{aligned} \tag{3.17}$$

where C_{e}, C_{et} and C_s are the submatrices of the partitioned 6×6 material stiffness matrix, Γ_{e}^R and Γ_s^R are non-mechanical strain components arranged in the same manner as Eq. (3.5), and can be calculated as

$$\Gamma_{ij}^R = m_{ij} + \beta_{ij}\xi \tag{3.18}$$

where β_{ij} are the cure shrinkage coefficients and ξ is DOC.

3.1.2 Classical Model

Using the energy density in Eq. (3.17), Eq. (2.54) can be solved based on VAM. Firstly a zeroth-order model, equivalent to the classical shell theory, is obtained by dropping all higher-order terms compared to unity in the total potential function, such that

$$\begin{aligned} 2\Pi_0 = \Big\langle & \left(\epsilon + x_3\kappa\right)^{\mathrm{T}} C_{\mathrm{e}} \left(\epsilon + x_3\kappa\right) + {w_{\|}}'^{\mathrm{T}} C_s {w_{\|}}' + {w_3}'^{\mathrm{T}} C_{33} {w_3}' \\ & + 2(\epsilon + x_3\kappa)^{\mathrm{T}} C_{\mathrm{et}} {w_3}' - 2 \Big[\left(\epsilon + x_3\kappa\right)^{\mathrm{T}} C_{\mathrm{e}} \Gamma_{\mathrm{e}}^R + \left(\epsilon + x_3\kappa\right)^{\mathrm{T}} C_{\mathrm{et}} \Gamma_{33}^R \\ & + {w_3}'^{\mathrm{T}} C_{33} \Gamma_{33}^R + {w_3}'^{\mathrm{T}} C_{\mathrm{et}}^{\mathrm{T}} \Gamma_{\mathrm{e}}^R + {w_{\|}}'^{\mathrm{T}} C_s \left(2\Gamma_s^R\right) \Big] \Big\rangle \end{aligned} \tag{3.19}$$

Then the variational statement can be written as

$$\begin{aligned}\delta\Pi_0 =& \left\langle \left[{w_3}'^{\mathrm{T}} C_{33} + (\epsilon + x_3\kappa)^{\mathrm{T}} C_{et} - \left(\Gamma_{33}^R C_{33} + \Gamma_{\mathrm{e}}^{R^{\mathrm{T}}} C_{et} \right) \right] \delta {w_3}' \right. \\ & \left. + \left[{w_\parallel}'^{\mathrm{T}} C_s - \left(2\Gamma_s^R \right)^{\mathrm{T}} C_s \right] \delta {w_\parallel}' \right\rangle \\ =& 0 \end{aligned} \tag{3.20}$$

From Eq. (3.20), Euler-Lagrange equations for solving $w_\parallel$ and w_3 can be obtained as

$$\left[{w_3}'^{\mathrm{T}} C_{33} + (\epsilon + x_3\kappa)^{\mathrm{T}} C_{et} - \left(\Gamma_{33}^R C_{33} + \Gamma_{\mathrm{e}}^{R^{\mathrm{T}}} C_{et} \right) \right]' = 0 \tag{3.21}$$

$$\left[{w_\parallel}'^{\mathrm{T}} C_s - \left(2\Gamma_s^R \right)^{\mathrm{T}} C_s \right]' = 0 \tag{3.22}$$

with boundary conditions

$$\left[{w_3}'^{\mathrm{T}} C_{33} + (\epsilon + x_3\kappa)^{\mathrm{T}} C_{et} - \left(\Gamma_{33}^R C_{33} + \Gamma_{\mathrm{e}}^{R^{\mathrm{T}}} C_{et} \right) \right]^+ = 0 \tag{3.23}$$

$$\left[{w_\parallel}'^{\mathrm{T}} C_s - \left(2\Gamma_s^R \right)^{\mathrm{T}} C_s \right]^+ = 0 \tag{3.24}$$

The boundary conditions in Eq. (3.23) and (3.24) is introduced based on the fact that w_i are free to vary on top surface, leading to $\delta w_i^+ \neq 0$. The boundary conditions corresponding to the bottom surface disappears because of the constraints in Eq. (3.1) that lead to w_i being specified on bottom surface so that $\delta w_i^- = 0$. Notice that though not explicitly denoted, all material properties can be different from layer to layer for a laminated shell, so in addition to boundary conditions, continuity conditions also need to be satisfied at the interfaces between layers.

Integrating Eq. (3.21) and (3.22) with respect to x_3 and utilize the boundary conditions, it can be trivially solved that integration constants are zero. Then, the fluctuating functions w_i can be obtained as

$${w_3}' = {C_\perp}' \mathcal{E} + {w_{3R}^0}' \tag{3.25}$$

$$w_{\|}{}' = 2\Gamma_s^R \tag{3.26}$$

with $\mathcal{E} = \begin{bmatrix} \epsilon & \kappa \end{bmatrix}^{\mathrm{T}}$ and

$$\begin{aligned} C_{\perp}{}' &= \begin{bmatrix} -\dfrac{C_{et}^{\mathrm{T}}}{C_{33}} & -x_3\dfrac{C_{et}^{\mathrm{T}}}{C_{33}} \end{bmatrix} \\ w_{3R}^{0}{}' &= \frac{C_{et}^{\mathrm{T}}}{C_{33}}\Gamma_{\mathrm{e}}^R + \Gamma_{33}^R \end{aligned} \tag{3.27}$$

With the solution of fluctuating functions, 2D constitutive model can be obtained by substituting Eq. (3.25) and (3.26) back into Eq. (3.19), gives

$$2\Pi_0 = \mathcal{E}^{\mathrm{T}} A^0 \mathcal{E} - 2\mathcal{E}^{\mathrm{T}} S_{\epsilon\kappa}^0 \tag{3.28}$$

with

$$\begin{aligned} A^0 &= \begin{bmatrix} \langle C_{\mathrm{e}}^* \rangle & \langle x_3 C_{\mathrm{e}}^* \rangle \\ \langle x_3 C_{\mathrm{e}}^* \rangle^{\mathrm{T}} & \langle {x_3}^2 C_{\mathrm{e}}^* \rangle \end{bmatrix} \\ S_{\epsilon\kappa}^0 &= \begin{Bmatrix} \left\langle C_{\mathrm{e}}^* \Gamma_{\mathrm{e}}^R \right\rangle \\ \left\langle x_3 C_{\mathrm{e}}^* \Gamma_{\mathrm{e}}^R \right\rangle \end{Bmatrix} \end{aligned} \tag{3.29}$$

where

$$C_{\mathrm{e}}^* = C_{\mathrm{e}} - \frac{C_{et} C_{et}^{\mathrm{T}}}{C_{33}} \tag{3.30}$$

The equivalent stiffness matrix in Eq. (3.29) has the same form as the ABD matrices in the classical shell theory, so they can be used as the sectional stiffness matrix of shell elements in finite element analysis for predicting the global behavior. With the results from 2D global analysis, 3D strain fields can be recovered by neglecting smaller terms in Eq. (3.4), leads to

$$\begin{aligned} \Gamma_{\mathrm{e}}^0 &= \epsilon + x_3\kappa \\ 2\Gamma_s^0 &= w_{\|}{}' \\ \Gamma_{33}^0 &= w_3{}' \end{aligned} \tag{3.31}$$

The 3D stress fields can be obtained using the 3D stress-strain relations.

Different from conventional shell theories, the MSG-based shell theory can predict the thickness change of the shell as the transverse normal strain Γ_{33} can be directly recovered from the fluctuating function.

3.1.3 Geometric Corrections

The equivalent classical shell model can have accurate prediction of the shell behavior for thin shells. However, when the shell has moderate thickness, depending on the loads and boundary conditions, the classical model can lose significant accuracy. Specifically, when the shell extension is much greater than bending, i.e. $\varepsilon_{\alpha\beta} \gg \kappa_{\alpha\beta}$, geometric corrections to the order of h/R become necessary [109], [110].

Unlike the classical model or the transverse shear refined model in the next section, introducing geometric corrections does not need to re-calculate the fluctuating functions [36], as only terms of h/R are kept. Keeping h/R terms in the total potential function gives

$$\begin{aligned}
2\Pi_k =& 2\Pi_0 + \Big\langle (\rho-1)\left(\epsilon + x_3\kappa\right)^{\mathrm{T}} C_{\mathrm{e}} \left(\epsilon + x_3\kappa\right) + (\rho-1)\, {w_3}'^{\mathrm{T}} C_{33} {w_3}' \\
&+ 2(\rho-1)\left(\epsilon + x_3\kappa\right)^{\mathrm{T}} C_{et} {w_3}' + 2\left(\epsilon + x_3\kappa\right)^{\mathrm{T}} C_{\mathrm{e}} \left(R_{k\mathrm{e}} w_3\right) \\
&+ 2{w_3}'^{\mathrm{T}} C_{et}^{\mathrm{T}} \left(R_{k\mathrm{e}} w_3\right) + 2x_3 \left(\epsilon + x_3\kappa\right)^{\mathrm{T}} C_{\mathrm{e}} k \left(\epsilon + x_3\kappa\right) \\
&+ 2x_3 {w_3}'^{\mathrm{T}} C_{et}^{\mathrm{T}} k \left(\epsilon + x_3\kappa\right) - 2\Big[(\rho-1)\left(\epsilon + x_3\kappa\right)^{\mathrm{T}} C_{\mathrm{e}} \Gamma_{\mathrm{e}}^R \\
&+ (\rho-1)\left(\epsilon + x_3\kappa\right)^{\mathrm{T}} C_{et} \Gamma_{33}^R + (\rho-1)\, {w_3}'^{\mathrm{T}} C_{33} \Gamma_{33}^R + (\rho-1)\, {w_3}'^{\mathrm{T}} C_{et}^{\mathrm{T}} \Gamma_{\mathrm{e}}^R \\
&+ \left(R_{k\mathrm{e}} w_3\right)^{\mathrm{T}} C_{\mathrm{e}} \Gamma_{\mathrm{e}}^R + \left(R_{k\mathrm{e}} w_3\right)^{\mathrm{T}} C_{et} \Gamma_{33}^R + x_3 \left(\epsilon + x_3\kappa\right)^{\mathrm{T}} k^{\mathrm{T}} C_{\mathrm{e}} \Gamma_{\mathrm{e}}^R \\
&+ x_3 \left(\epsilon + x_3\kappa\right)^{\mathrm{T}} k^{\mathrm{T}} C_{et} \Gamma_{33}^R \Big] \Big\rangle
\end{aligned} \tag{3.32}$$

Substitute Eq. (3.25) and (3.26) into Eq. (3.32) and rearrange, giving

$$2\Pi_k = \mathcal{E}^{\mathrm{T}} A^k \mathcal{E} - 2\mathcal{E}^{\mathrm{T}} S_{\epsilon\kappa}^k \tag{3.33}$$

with

$$A^k = \begin{bmatrix} \langle \rho C_{\mathrm{e}}^* + C_k \rangle & \langle x_3 \left(\rho C_{\mathrm{e}}^* + C_k\right) \rangle \\ \langle x_3 \left(\rho C_{\mathrm{e}}^* + C_k\right) \rangle^{\mathrm{T}} & \langle {x_3}^2 \left(\rho C_{\mathrm{e}}^* + C_k\right) \rangle \end{bmatrix} + \langle C_R \rangle \tag{3.34}$$

$$S_{\epsilon\kappa}^k = \begin{Bmatrix} \left\langle \rho C_{\mathrm{e}}^* \Gamma_{\mathrm{e}}^R + x_3 k^{\mathrm{T}} C_{\mathrm{e}}^* \Gamma_{\mathrm{e}}^R \right\rangle \\ \left\langle x_3 \left(\rho C_{\mathrm{e}}^* \Gamma_{\mathrm{e}}^R + x_3 k^{\mathrm{T}} C_{\mathrm{e}}^* \Gamma_{\mathrm{e}}^R \right) \right\rangle \end{Bmatrix} + \langle S_R \rangle \tag{3.35}$$

where

$$\begin{aligned} C_k &= x_3 k^{\mathrm{T}} C_{\mathrm{e}}^* + x_3 C_{\mathrm{e}}^* k \\ C_R &= C_\perp^{\mathrm{T}} \begin{bmatrix} R_{ke}^{\mathrm{T}} C_{\mathrm{e}}^* & x_3 R_{ke}^{\mathrm{T}} C_{\mathrm{e}}^* \end{bmatrix} + \begin{bmatrix} R_{ke}^{\mathrm{T}} C_{\mathrm{e}}^* & x_3 R_{ke}^{\mathrm{T}} C_{\mathrm{e}}^* \end{bmatrix}^{\mathrm{T}} C_\perp \end{aligned} \tag{3.36}$$

$$S_R = -\begin{bmatrix} R_{ke}^{\mathrm{T}} C_{\mathrm{e}}^* & x_3 R_{ke}^{\mathrm{T}} C_{\mathrm{e}}^* \end{bmatrix}^{\mathrm{T}} w_{3R}^0 + C_\perp^{\mathrm{T}} R_{ke}^{\mathrm{T}} C_{\mathrm{e}}^* \Gamma_{\mathrm{e}}^R \tag{3.37}$$

The energy expression in Eq. (3.33) has the same form as the classical model, but the matrices in Eq. (3.34) and (3.35) contain more terms due to geometric corrections. Specifically, if the middle surface is taken as the reference surface, a symmetric laminate will have the B matrix equal to zero in the classical model, while it is not zero when geometric corrections are taken into consideration. This means that initial geometry of the shell can bring in some extension-bending couplings.

Similar to the classical model, 3D strain fields can be recovered with solution of the global shell analysis using the relations

$$\begin{aligned} \Gamma_{\mathrm{e}}^k &= \epsilon + x_3 \kappa + R_{ke} w_3 + x_3 k \epsilon + x_3^2 k \kappa \\ 2\Gamma_s^k &= {w_\parallel}' + R_{ks} w_\parallel \\ \Gamma_{33}^k &= {w_3}' \end{aligned} \tag{3.38}$$

However, because the fluctuating functions w_i directly comes from the result of the classical model, results recovered using Eq. (3.38) will inevitably include an error up to the order of h/R. This deviation can be avoided by solving the fluctuating function to the order of h/R, but to do so the total potential need to be expanded to the order of h^2/R^2. Due to

the complexity of the expressions as well as in most cases an error of h/R is acceptable, the solution of fluctuating functions to the order of h/R is believed to be unnecessary.

3.1.4 Transverse Shear Deformation

The equivalent classical shell model provides accurate prediction on the in-plane extension and bending behavior of the shell, and when the influence of initial geometry is significant, geometric corrections can effectively improve the solution of the global shell analysis. However, both models take the same form as the classical shell theory, making the prediction of transverse shear behavior impossible. When the shell thickness is moderate, depending on the loading and boundary conditions, transverse shear can greatly affect the global shell behavior. In order to capture the transverse shear behavior, a refined model to the order of h^2/l^2 becomes necessary.

To obtain a model of h^2/l^2, the fluctuating functions need to be solved to the order of h/l. Expanding the fluctuating functions gives

$$\begin{aligned} w_\parallel &= w_\parallel^0 + v_\parallel \\ w_3 &= w_3^0 + v_3 \end{aligned} \tag{3.39}$$

where $w_\parallel^0$ and w_3^0 are the solution of the fluctuating function from Eq. (3.26) and (3.25) respectively; $v_\parallel$ and v_3 are the h/l part of the fluctuating functions. Similar to last section, terms to the order of h/l and h^2/l^2 need to be included in the total potential, such that

$$\begin{aligned} 2\Pi_1 =& 2\Pi_k + \Big\langle 2(\epsilon + x_3\kappa)^{\mathrm{T}} C_{\mathrm{e}} I_\alpha w_{\parallel;\alpha}^0 + 2(\epsilon + x_3\kappa)^{\mathrm{T}} C_{\mathrm{e}} I_\alpha v_{\parallel;\alpha} \\ &+ 2\Big(I_\alpha w_{\parallel;\alpha}^0\Big)^{\mathrm{T}} C_{\mathrm{et}} {v_3}' + 2\Big(I_\alpha w_{\parallel;\alpha}^0\Big)^{\mathrm{T}} C_{\mathrm{et}} w_3^{0\prime} + 2\Big(I_\alpha v_{\parallel;\alpha}\Big)^{\mathrm{T}} C_{\mathrm{et}} w_3^{0\prime} \\ &+ \gamma^{\mathrm{T}} C_s \gamma + 2\gamma^{\mathrm{T}} C_s w_\parallel^{0\prime} + 2\gamma^{\mathrm{T}} C_s {v_\parallel}' + 2\gamma^{\mathrm{T}} C_s \mathrm{e}_\alpha w_{3;\alpha}^0 + {v_\parallel}'^{\mathrm{T}} C_s {v_\parallel}' \\ &+ 2{v_\parallel}'^{\mathrm{T}} C_s \mathrm{e}_\alpha w_{3;\alpha}^0 + \Big(\mathrm{e}_\alpha w_{3;\alpha}^0\Big)^{\mathrm{T}} C_s \mathrm{e}_\alpha w_{3;\alpha}^0 + {v_3}'^{\mathrm{T}} C_{33} {v_3}' \\ &- 2\left[\Big(I_\alpha v_{\parallel;\alpha}\Big)^{\mathrm{T}} C_{\mathrm{e}} \Gamma_{\mathrm{e}}^R + \Big(I_\alpha v_{\parallel;\alpha}\Big)^{\mathrm{T}} C_{\mathrm{et}} \Gamma_{33}^R + \gamma^{\mathrm{T}} C_s \left(2\Gamma_s^R\right)\right]\Big\rangle \\ &- 2\left[\Big\langle P_\parallel^{\mathrm{T}} v_\parallel \Big\rangle + \tau_\parallel^{\mathrm{T}} v_\parallel^+ + \beta_\parallel^{\mathrm{T}} v_\parallel^- + \Big\langle P_3 w_3^0 \Big\rangle + \tau_3 w_3^{0+} + \beta_3 w_3^{0-}\right] \end{aligned} \tag{3.40}$$

The variation of Eq. (3.40) is

$$\begin{aligned}\delta\Pi_1 = &\left\langle \left[\left(\gamma + {v_\parallel}' + \mathrm{e}_\alpha w^0_{3;\alpha}\right)^{\mathrm{T}} C_s\right]\delta {v_\parallel}' + \left[\left(I_\alpha w^0_{\parallel;\alpha}\right)^{\mathrm{T}} C_{et} + {v_3}' C_{33}\right]\delta {v_3}' \right. \\ &\left. + \left[(\epsilon + x_3\kappa)^{\mathrm{T}} C^*_{\mathrm{e}} - {\Gamma^R_{\mathrm{e}}}^{\mathrm{T}} C^*_{\mathrm{e}}\right] I_\alpha \delta v_{\parallel;\alpha}\right\rangle - \left\langle P^{\mathrm{T}}_\parallel \delta v_\parallel \right\rangle - \tau^{\mathrm{T}}_\parallel \delta v^+_\parallel - \beta^{\mathrm{T}}_\parallel \delta v^-_\parallel \\ &= 0\end{aligned} \tag{3.41}$$

Similar to the derivation of the classical model, Euler-Lagrange equations for $v_\parallel$ and v_3 can be obtained as

$$\left[C_s\left(\gamma + {v_\parallel}' + \mathrm{e}_\alpha w^0_{3;\alpha}\right)\right]' = {D_\alpha}' \mathcal{E}_{;\alpha} + g' \tag{3.42}$$

$$\left[\left(I_\alpha w^0_{\parallel;\alpha}\right)^T C_{et} + {v_3}' C_{33}\right]' = 0 \tag{3.43}$$

with boundary conditions

$$\left[C_s\left(\gamma + {v_\parallel}' + \mathrm{e}_\alpha w^0_{3;\alpha}\right)\right]^+ = \tau_\parallel \tag{3.44}$$

$$\left[\left(I_\alpha w^0_{\parallel;\alpha}\right)^{\mathrm{T}} C_{et} + {v_3}' C_{33}\right]^+ = 0 \tag{3.45}$$

where

$${D_\alpha}' = -I^{\mathrm{T}}_\alpha \begin{bmatrix} C^*_{\mathrm{e}} & x_3 C^*_{\mathrm{e}} \end{bmatrix} \tag{3.46}$$

$$g' = I^{\mathrm{T}}_\alpha C^*_{\mathrm{e}} \Gamma^R_{\mathrm{e};\alpha} - P_\parallel \tag{3.47}$$

Boundary conditions corresponding to the bottom surface for the same reason as Section 3.1.2. Then, v_3 can be solved as

$$v_3' = -\frac{C^{\mathrm{T}}_{et}}{C_{33}} I_\alpha w^0_{\parallel;\alpha} \tag{3.48}$$

Integrating Eq. (3.42) with respect to x_3 gives

$$C_s\left(\gamma + {v_\parallel}' + \mathrm{e}_\alpha w^0_{3;\alpha}\right) = D_\alpha \mathcal{E}_{;\alpha} + g + \bar{\mu}_\parallel \tag{3.49}$$

Due to the effect of in-plane traction applied on the top surface, integration constants $\bar{\mu}_{\|}$ are not zero. Using the boundary conditions in Eq. (3.44), $\bar{\mu}_{\|}$ can be derived to be

$$\bar{\mu}_{\|} = \tau_{\|} - D_{\alpha}^{+}\mathcal{E}_{;\alpha} - g^{+} \tag{3.50}$$

Then

$${v_{\|}}' = -\gamma + C_s^{-1}D_{\alpha}^{*}\mathcal{E}_{;\alpha} - \mathrm{e}_{\alpha}C_{\perp}\mathcal{E}_{;\alpha} + C_s^{-1}g^{*} - \mathrm{e}_{\alpha}w_{3R;\alpha}^{0} \tag{3.51}$$

where

$$D_{\alpha}^{*} = D_{\alpha} - D_{\alpha}^{+} \tag{3.52}$$

$$g^{*} = g + \tau_{\|} - g^{+} \tag{3.53}$$

Integrating Eq. (3.51) gives

$$v_{\|} = -x_3\gamma + (\bar{D}_{\alpha} + L_{\alpha})\mathcal{E}_{;\alpha} + \bar{g} \tag{3.54}$$

where

$$\bar{D}_{\alpha}' = C_s^{-1}D_{\alpha}^{*} - \mathrm{e}_{\alpha}C_{\perp} \tag{3.55}$$

$$\bar{g}' = C_s^{-1}g^{*} - \mathrm{e}_{\alpha}w_{3R;\alpha}^{0} \tag{3.56}$$

In order to satisfy the constraints in Eq. (3.1), constants L_{α} are introduced, which satisfy

$$L_{\alpha}\mathcal{E}_{;\alpha} = c_{\|} \tag{3.57}$$

These constants will be used as optimization parameters for transforming the model to the form of the Reissner-Mindlin model.

Substituting the solution of fluctuating functions back into the total potential in Eq. (3.40) gives

$$2\Pi_1 = \mathcal{E}^{\mathrm{T}}A^{k}\mathcal{E} + \mathcal{E}_{;\alpha}^{\mathrm{T}}B_{\alpha\beta}\mathcal{E}_{;\beta} - 2\mathcal{E}^{\mathrm{T}}\left\langle D_{\alpha}^{*\mathrm{T}}\right\rangle\gamma_{;\alpha} - 2\mathcal{E}^{\mathrm{T}}F + 2\gamma^{\mathrm{T}}\left\langle g^{*}\right\rangle \tag{3.58}$$

where

$$\begin{aligned} B_{\alpha\beta} = & \left\langle -{D_\alpha^*}^{\mathrm{T}} C_s^{-1} D_\beta^* + {D_\alpha^*}^{\mathrm{T}} \mathrm{e}_\beta C_\perp + C_\perp^{\mathrm{T}} \mathrm{e}_\alpha^{\mathrm{T}} D_\beta^* \right\rangle \\ & + \left\langle {D_\alpha'}^{\mathrm{T}} \right\rangle L_\beta + L_\alpha^{\mathrm{T}} \left\langle D_\beta' \right\rangle \end{aligned} \tag{3.59}$$

$$\begin{aligned} F = & S_{\epsilon\kappa}^k + \left\langle -{D_\alpha^*}^{\mathrm{T}} C_s^{-1} g_{;\alpha}^* + {D_\alpha^*}^{\mathrm{T}} \mathrm{e}_\beta w_{3R;\alpha\beta}^0 + C_\perp^{\mathrm{T}} \mathrm{e}_\alpha^{\mathrm{T}} g_{;\alpha}^* \right\rangle \\ & + \left\langle C_\perp^{\mathrm{T}} P_3 \right\rangle + {C_\perp^+}^{\mathrm{T}} \tau_3 - L_\alpha^{\mathrm{T}} \Big(\beta_\parallel - \left\langle g' \right\rangle \Big)_{;\alpha} \end{aligned} \tag{3.60}$$

and A^k and $S_{\epsilon\kappa}^k$ are the matrices in Eq. (3.34) and (3.35). Although Eq. (3.58) is asymptotically correct up to the order of h^2/l^2, it is not convenient for practical use because it contains derivatives of 2D strain, making the boundary conditions hard to define. This problem can be solved if it can be transformed into the form of the Reissner-Mindlin model, which is commonly used in shell analyses. Comparing Eq. (3.58) with the total potential of the Reissner-Mindlin model, which takes the form of

$$2\Pi_{\mathcal{R}} = \mathcal{E}^{\mathrm{T}} A^k \mathcal{E} + \gamma^{\mathrm{T}} G \gamma - 2\mathcal{E}^{\mathrm{T}} F - 2\gamma^{\mathrm{T}} F_\gamma \tag{3.61}$$

all partial derivatives of 2D strains must be eliminated. Using the shell equilibrium equations

$$G\gamma - F_\gamma = \mathcal{D}_\alpha^{\mathrm{T}} A^0 \mathcal{E}_{;\alpha} - \mathcal{D}_\alpha^{\mathrm{T}} F_{;\alpha} + \begin{Bmatrix} m_1 \\ m_2 \end{Bmatrix} \tag{3.62}$$

where

$$\begin{aligned} \mathcal{D}_1 &= \begin{bmatrix} 0 & 0 & 0 & 1 & 0 & 0 \\ 0 & 0 & 0 & 0 & 1 & 0 \end{bmatrix}^{\mathrm{T}} \\ \mathcal{D}_2 &= \begin{bmatrix} 0 & 0 & 0 & 0 & 1 & 0 \\ 0 & 0 & 0 & 0 & 0 & 1 \end{bmatrix}^{\mathrm{T}} \end{aligned} \tag{3.63}$$

Eq. (3.58) can be written as

$$2\Pi_1 = \mathcal{E}^{\mathrm{T}} A^k \mathcal{E} + \mathcal{E}_{;\alpha}^{\mathrm{T}} \bar{B}_{\alpha\beta} \mathcal{E}_{;\beta} + \gamma^{\mathrm{T}} G \gamma - 2\mathcal{E}^{\mathrm{T}} F - 2\gamma^{\mathrm{T}} F_\gamma \tag{3.64}$$

where

$$\begin{aligned} \bar{B}_{\alpha\beta} &= B_{\alpha\beta} + A^0 \mathcal{D}_\alpha G^{-1} \mathcal{D}_\beta^{\mathrm{T}} A^0 \\ F_\gamma &= -\langle g^* \rangle \end{aligned} \tag{3.65}$$

Notice in Eq. (3.62) A^0 instead of A^k is used, as h/R terms introduced from A^k will generate h^2/lR terms when multiplied with in-plane partial derivatives of 2D strains, which are considered small and can be dropped. At this point, transverse shear stiffness matrix G is still unknown, and partial derivatives still exist in Eq. (3.64). To obtain the expression in the form of of the Reissner-Mindlin model, the most ideal case is that $\bar{B}_{\alpha\beta}$ can be driven to zero by defining appropriate G, but this is not achievable even for an isotropic plate, so the best way is to drive them to as close to zero as possible using an optimization process, in which way the error between the equivalent Reissner-Mindlin model and asymptotically correct model can be minimized. Considering symmetry, there are totally 78 quantities that should be minimized to be zero, 21 terms of $\bar{B}_{11}$, 36 terms of $\bar{B}_{12} = \bar{B}_{21}^{\mathrm{T}}$, and 21 terms of $\bar{B}_{22}$. There are 27 parameters that can be solved to drive $\bar{B}_{\alpha\beta}$ as close to zero as possible, 3 terms in G and 24 terms in L_1 and L_2. Since $\bar{B}_{\alpha\beta}$ are written in terms of G and L_α, a column matrix with the 27 parameters can be formed, so that a 78×27 coefficient matrix can be constructed. This will lead to an overdetermined linear system with 78 equations and 27 unknowns, and the least square method can be used to solve for the 27 unknowns with a minimized error.

By the optimization process, the best transverse shear stiffness matrix G can be obtained to fit into to the Reissner-Mindlin model. The current equivalent model can be directly applied in any Reissner-Mindlin shell analyses with equivalent stiffness matrices A^k, G, F and F_γ calculated from shell geometry and material constants.

3D displacement fields u_i can be easily recovered using Eq. (2.3). By neglecting smaller terms not contributing to energy, the 3D strain fields can be recovered to be

$$\begin{aligned}
\Gamma_{\mathrm{e}}^1 &= \epsilon + x_3\kappa + I_\alpha w_{\|;\alpha}^0 + R_{k\mathrm{e}} w_3^0 + x_3 k\epsilon + x_3^2 k\kappa \\
2\Gamma_s^1 &= \gamma + w_\|^{0\prime} + v_\|{}' + \mathrm{e}_\alpha w_{3;\alpha}^0 + R_{ks} w_\|^0 \\
\Gamma_{33}^1 &= w_3^{0\prime} + v_3{}'
\end{aligned} \tag{3.66}$$

For the same reason as discussed in last section, 3D strains recovered from Eq. (3.66) will have an error to the order of h/R. However, due to the fact that total potential is expanded to the order of h^2/l^2 and fluctuating functions are solved to the order of h/l, accurate recovery can be achieved when the shell has no initial curvature, i.e. becomes a plate.

3.2 Case Studies

To validate the formulation developed in Section 3.1, case studies are necessary. For this purpose, three kinds of shells are studied. Firstly a unidirectional shell is studied, in which case 3D exact solution exists, so that the performance of the formulation with geometric corrections can be rigorously evaluated. Then, a more realistic situation is simulated with laminated shells as the parts, contacting with tools modeled as 3D solids. Lastly the effect of transverse shear stiffness is studied using an example.

3.2.1 Unidirectional Shell

Before applying the MSG-based analytical shell formulation to calculate the stress and deformation in a curing simulation containing the part and the tool, a simple case with an infinite width, which means it is infinite large in the out-of-plane direction so that plane strain assumption can be adopted, unidirectional shell under temperature change is studied. In this case, a 3D exact solution based on plane strain can be obtained, and global shell analysis can be solved analytically. Geometry of the part is shown in Figure 3.2, with the thickness h being 1.488 mm, inner radius R being 20 mm, and angle span φ being $\pi/4$. The boundary condition is simply supported at the bottom surface. In this study, a uniform

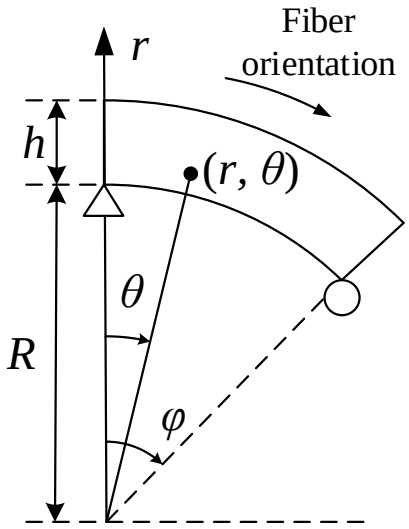

Figure 3.2. Geometry of the unidirectional shell.

temperature change of -160 °C is applied on the shell, without mechanical loading. The material is AS4/8552 continuous fiber composite, with the fiber orientation following the curve. Material properties of the composite is shown in Table 3.1.

Table 3.1. Material properties of AS4/8552 composite.

E_1 (MPa)	122.57×10^3
$E_2 = E_3$ (MPa)	9.72×10^3
$G_{12} = G_{13}$ (MPa)	5.21×10^3
G_{23} (MPa)	3.38×10^3
$\nu_{12} = \nu_{13}$	0.27
ν_{23}	0.44
α_1 ($^\circ C^{-1}$)	0.06×10^{-5}
$\alpha_2 = \alpha_3$ ($^\circ C^{-1}$)	3.65×10^{-5}

Following [111], this original 3D thermoelasticity problem can be solved analytically using a cylindrical coordinate system. Since this 3D problem is in a plane strain state, constitutive equations can be written first

$$\begin{aligned}
\varepsilon_\theta &= \left(S_{22} - \frac{S_{23}^2}{s_{33}}\right)\sigma_\theta + \left(S_{12} - \frac{S_{23}S_{13}}{s_{33}}\right)\sigma_r - \frac{S_{23}}{S_{33}}\alpha_z\Delta T + \alpha_\theta\Delta T \\
\varepsilon_r &= \left(S_{11} - \frac{S_{13}^2}{s_{33}}\right)\sigma_r + \left(S_{12} - \frac{S_{23}S_{13}}{s_{33}}\right)\sigma_\theta - \frac{S_{13}}{S_{33}}\alpha_z\Delta T + \alpha_r\Delta T \\
\gamma_{r\theta} &= S_{66}\tau_{r\theta}
\end{aligned} \tag{3.67}$$

where ε_r, ε_θ, $\gamma_{r\theta}$, σ_r, σ_θ, $\tau_{r\theta}$ are the normal and shear strains and stresses in the cylindrical coordinates, respectively; S_{ij} are terms of the 6×6 material compliance matrix; ΔT is the temperature change. By introducing a stress function, stresses can be expresses in terms of the stress function that automatically satisfy the equilibrium equations. Then, the stresses can be solved using compatibility equation along with traction boundary conditions. However, when mechanical loads are absent, it can be easily verified that $\sigma_r = \sigma_\theta = \tau_{r\theta} = 0$ satisfies all equations and boundary conditions. As a result, strains can be calculated using Eq. (3.67) by setting all stresses equal to zero. Then, displacement can be obtained using the strain-displacement relations along with displacement boundary conditions.

$$\begin{aligned}
\varepsilon_r &= \frac{\partial u_r}{\partial r} \\
\varepsilon_\theta &= \frac{1}{r}\frac{\partial u_\theta}{\partial \theta} + \frac{u_r}{r} \\
\gamma_{r\theta} &= \frac{1}{r}\frac{\partial u_r}{\partial \theta} + \frac{\partial u_\theta}{\partial r} - \frac{u_\theta}{r}
\end{aligned} \tag{3.68}$$

where u_r are u_θ are displacements in r and θ directions. With the geometry and material properties in this case, strains are constants in the whole part, with

$$\varepsilon_r = -0.00840077 \qquad \varepsilon_\theta = -0.000220276 \qquad \gamma_{r\theta} = 0 \tag{3.69}$$

and displacement u_r is

$$u_r = -0.00840077\ r + 0.168015\ \cos\theta + 0.0695943\ \sin\theta \tag{3.70}$$

When solving this problem as a shell, global curvilinear coordinate x_1 goes along with the curve of the bottom surface in the same direction as θ in Figure 3.2, and x_3 is the normal coordinates in the same direction as r. Using the MSG-based shell theory, equivalent stiffness matrices can be obtained, and used for solving the global shell problem analytically. The normal displacement of the bottom surface u_3 is solved to be

$$u_3 = 0.0692272 \sin\frac{x_1}{20} + 0.167129 \cos\frac{x_1}{20} - 0.167129 \tag{3.71}$$

By setting $r = 20$ and $\theta = x_1/20$ in Eq. (3.70), it takes the same form as Eq. (3.71) and the coefficients are close. Figure 3.3 shows the normal displacement predicted by the MSG-based shell theory, the 3D exact solution and Abaqus with composite shell section. It can be seen that the result from the MSG-based shell theory agrees well with the 3D exact solution, while the displacement is greatly underestimated with Abaqus composite shell section. This is mainly due to two reasons: when calculating the shell stiffness matrix, the Abaqus composite shell section cannot take the initial curvature into consideration, and Abaqus composite shell section is based on ad hoc kinematic assumptions such as the Kirchhoff assumptions used in CLT, while such assumptions are not used in MSG-based shell theory. However, as described in Section 3.1.3, strains predicted by MSG-based shell theory inevitably contain errors due to the formulation of geometric corrections. Longitudinal and transverse normal strains through the thickness at $\theta = \pi/8$ are shown in Figure 3.4 and 3.5. It can be seen that contrary to the 3D exact solution that strains are constant in the part, the MSG-based shell results are varying through the thickness. The largest error of these strains are -4.2329% and 2.8478% respectively. Considering the aspect ratio $h/R = 1.488/20 = 0.0744$, error of this magnitude is expected.

In order to demonstrate the capability of the MSG-based shell theory on handling nonuniform temperature change through the thickness, another example with a linear temperature distribution is presented. The geometry and material properties are identical to the previous example, but the temperature change is

$$\Delta T = -140 - \frac{40}{1.488}(r - R) \tag{3.72}$$

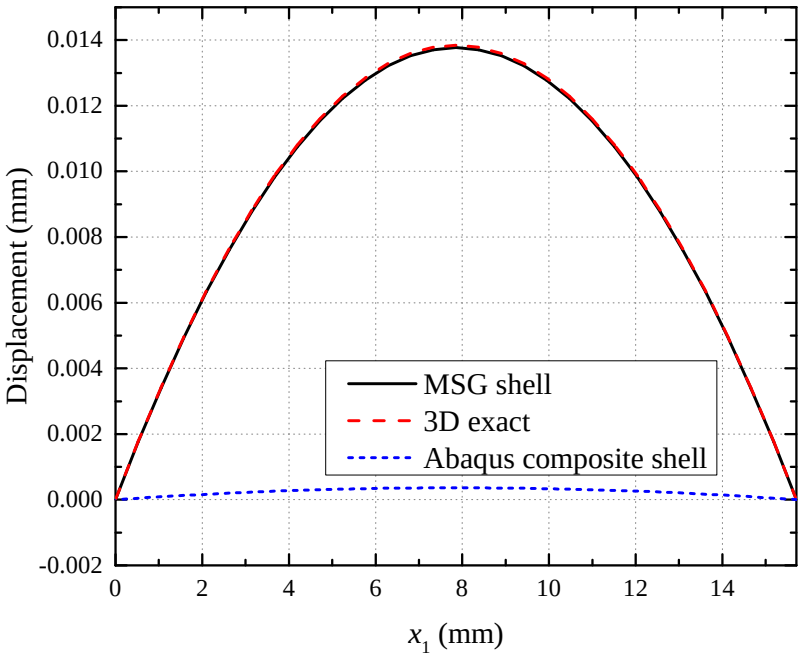

Figure 3.3. Normal displacement of the bottom surface u_3.

In this case, 3D exact solution is not available, so the shell analysis results are compared with Abaqus DNS with plane strain element CPE8R. Normal displacement of the bottom surface is shown in Figure 3.6. It is obvious that the MSG-based shell theory works well with nonuniform through-the-thickness temperature distribution, which can be confidently used to capture the phenomenon introduced by varying temperature distribution during composites curing.

3.2.2 Multi-Layered Structures

In real applications, composite parts are seldom made of composite layers with the same layup angle. In order to validate the capability of the MSG-based shell theory on composites curing simulation, laminates with complex layup need to be considered. In addition, during the curing process, not only temperature change, other factors will also affect the behavior so they need to be considered. For this purpose, models with a tool and a part with the

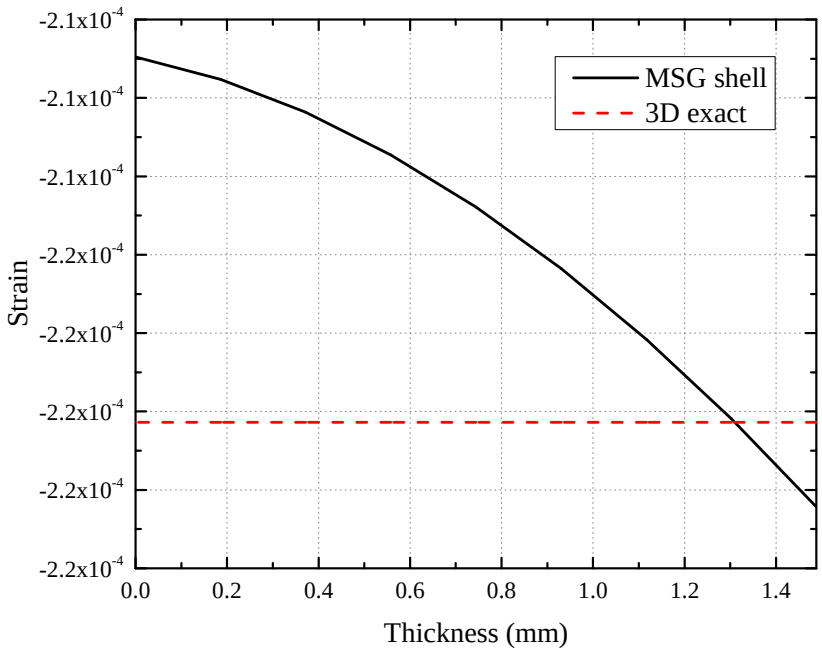

Figure 3.4. Longitudinal normal strain Γ_{11} through the thickness at $\theta = \pi/8$.

layup of $[90/\text{-}45/0/45]_{2s}$ are constructed in Abaqus. The tool is modeled using solid element C3D20R. For the MSG-based shell analysis, the part is modeled using shell element S8R, and for having an identical mesh in the reference surface, solid element C3D20R is chosen for the DNS. The contact between the part and the tool is modeled using a surface-to-surface contact in Abaqus, with a tangential friction coefficient of 0.15 and maximum shear stress of 40 kPa. Results from simulation with the MSG-based shell theory are compared with those from DNS.

Since the purpose of this study is to demonstrate the potential of the MSG-based shell theory, the whole curing process with continuous temperature and DOC history is simplified to have four states only. The first state is the initial state before curing, with a temperature of 20 °C and a DOC of 0%. The second state has a temperature of 180 °C and a DOC of 80%. The third state is the state after cooling, with a temperature of 20 °C and DOC of 80%. The last state is the state after detooling, with the tool removed. In the MSG-based shell analysis, stiffness of shell elements as well as non-mechanical section forces and moments are

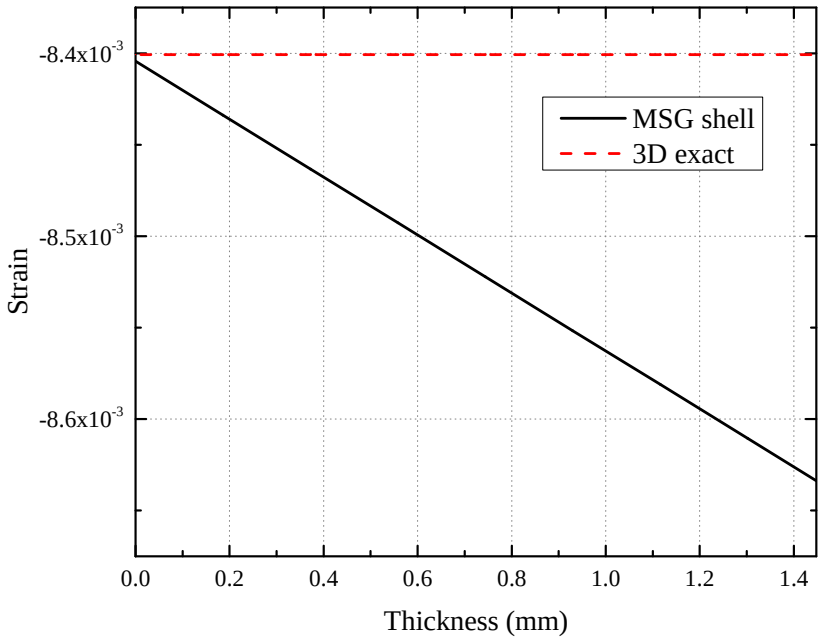

Figure 3.5. Longitudinal normal strain Γ_{33} through the thickness at $\theta = \pi/8$.

calculated using the lamina properties of composite parts, along with the temperature and DOC of each state. However, when implementing the shell stiffness into Abaqus through the user subroutine UGENS, the transverse shear stiffness has to be constant within the section through the whole analysis due to current limitation of UGENS. For a direct comparison between the MSG-based shell analysis and DNS, transverse shear moduli G_{13} and G_{23} are fixed at the value of the final state.

The material of the part is AS4/8552, with the shear moduli G_{13} and G_{23} being constant in the whole simulation. Material properties are shown in Table 3.2. The effect of varying transverse shear stiffness is discussed in the following subsection. The CTEs are also varying with temperature. As the fiber properties are not changing, CTE change in fiber orientation is negligible while in other directions a linear variation with the temperature is assumed [49], so that $\breve{\alpha}_{11} = 6.00 \times 10^{-7}$ °C^{-1}, $\breve{\alpha}_{22} = \breve{\alpha}_{33} = 3.65 \times 10^{-5}$ °C^{-1}. The cure shrinkage only happens when there is a change in DOC. The cure shrinkage coefficients used here are $\beta_{11} = -8.82 \times 10^{-7}$, $\beta_{22} = \beta_{33} = -3.41 \times 10^{-2}$. The material properties of the tool does not

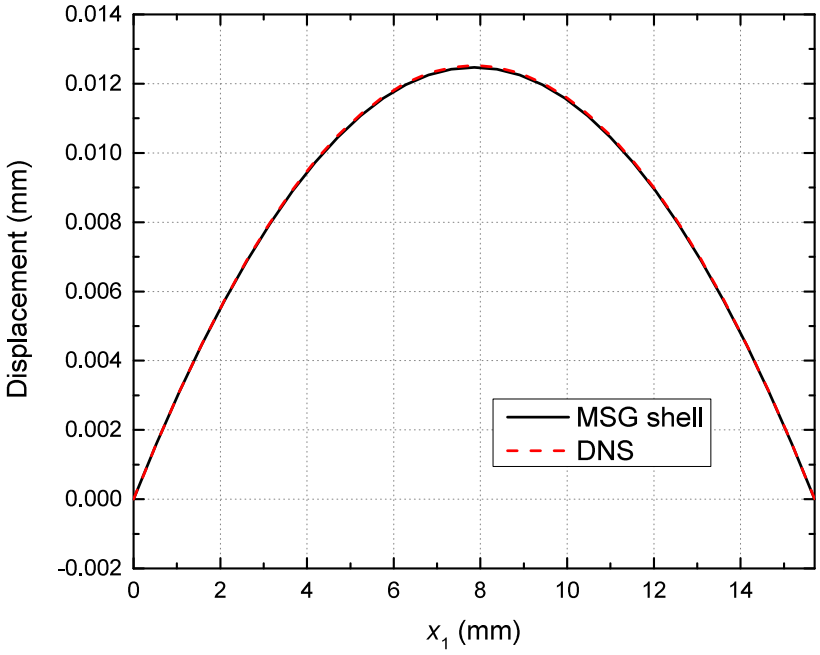

Figure 3.6. Normal displacement of the bottom surface u_3.

Table 3.2. Material properties of the composite lamina with constant G_{13} and G_{23}.

	1st state	2nd state	3rd and 4th state
E_1 (MPa)	120.54×10^3	122.57×10^3	122.57×10^3
$E_2 = E_3$ (MPa)	22.97	9.72×10^3	9.72×10^3
$\nu_{12} = \nu_{13}$	0.33	0.27	0.27
ν_{23}	1.00	0.44	0.44
G_{12} (MPa)	5.75	5.21×10^3	5.21×10^3
G_{13} (MPa)	5.21×10^3	5.21×10^3	5.21×10^3
G_{23} (MPa)	3.38×10^3	3.38×10^3	3.38×10^3

change during the curing process, having a Young's modulus of $E = 69$ GPa, Poisson's ratio of 0.327 and CTE of 2.36×10^{-5} K^{-1}.

In the first example, the part is an L-shape laminate. Geometry of the part is shown in Figure 3.7, with a width of 100 mm and total thickness of 3 mm. Shell and DNS models in Abaqus are shown in Figure 3.8. The shell model uses the bottom surface as the reference surface so it can be seen overlapping with the top surface of the tool. Spring-in angles after

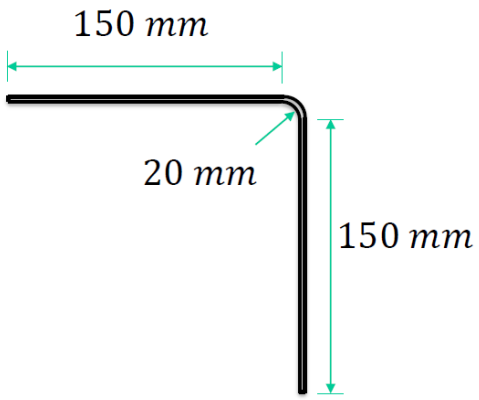

Figure 3.7. Geometry of the L-shape part.

detooling along with model size in Abaqus are shown in Table 3.3. It can be seen that

Table 3.3. Spring-in angles and model sizes of the L-shape part with constant G_{13} and G_{23}.

	Spring-in angle (°)	Number of nodes	Number of elements
MSG shell	3.667966	147,935	43,694
DNS	3.744059	2,435,359	574,694

compared with DNS, the MSG-based shell analysis has a high accuracy on predicting the spring-in angle, with an error of -2.03%, while the number of nodes used in the MSG-based shell analysis is only about 5% of that in the DNS model, which means computational cost is greatly reduced. It has been shown that strains recovered with geometric corrections contain error, but if there is no initial curvature, strains and stresses recovered from the MSG-based shell theory will be accurate. Longitudinal normal stress σ_{11} and shear stress σ_{12} through the thickness at the center point of the vertical flat region is shown in Figure 3.9 and Figure 3.10. It can be seen that layer-wise distributed stresses are accurately captured.

The second example is a C-channel, as shown in Figure 3.11. The width and total thickness are the same as the last example, 100 mm and 3 mm respectively. In Table 3.4, model size and spring-in angle of both sides of the MSG-base shell model and DNS model are presented. Similar to the first example, it is obvious that MSG-based shell analysis can

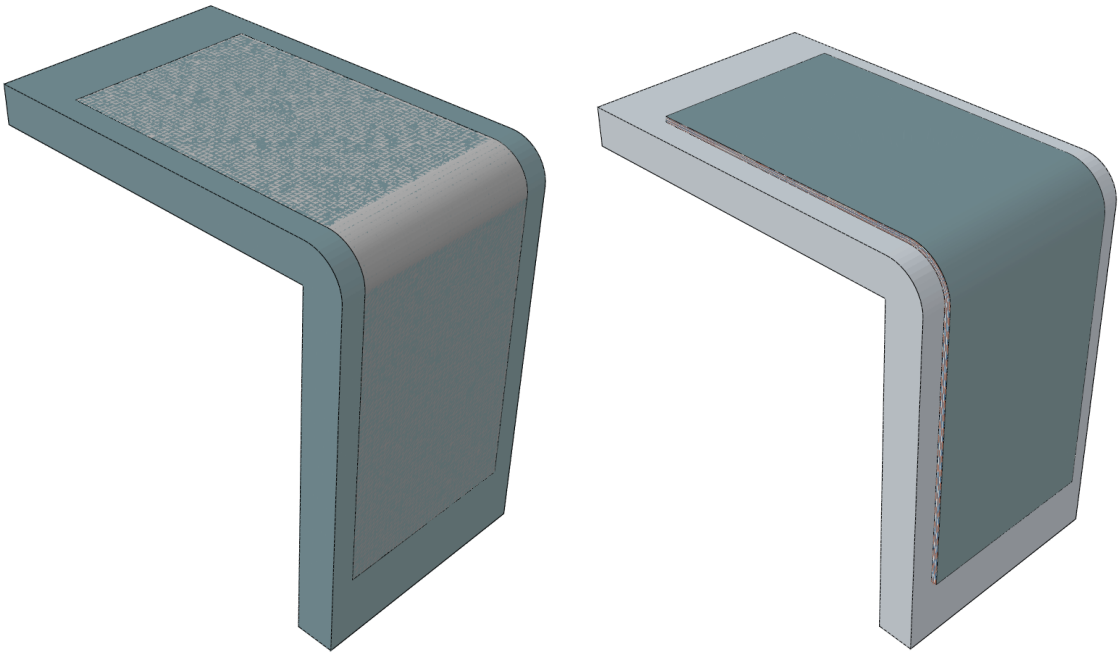

(a) Shell model. (b) DNS model.

Figure 3.8. Tool and L-shape part model in Abaqus.

Table 3.4. Spring-in angles and model sizes of the C-channel part with constant G_{13} and G_{23}.

	Spring-in angle (°)		Number of nodes	Number of elements
	Left	Right		
MSG shell	3.574787	3.574782	244,648	71,564
DNS	3.733181	3.733181	3,907,464	921,164

accurately predict the spring-in on both sides of the part, with an error of -4.24% on both the left and the right, with significantly decreased computational cost.

3.2.3 Effect of Transverse Shear Stiffness

In a real curing process of a composite part, temperature and DOC of the part are changing continuously with respect to time, resulting continuous histories of all the properties of the lamina, including elastic moduli, Poisson's ratios, CTEs and cure shrinkage coefficients. To capture this physics, simulation using the cure-hardening instantaneously linear elastic (CHILE) [45] model can be adopted. In the CHILE model, material properties at every

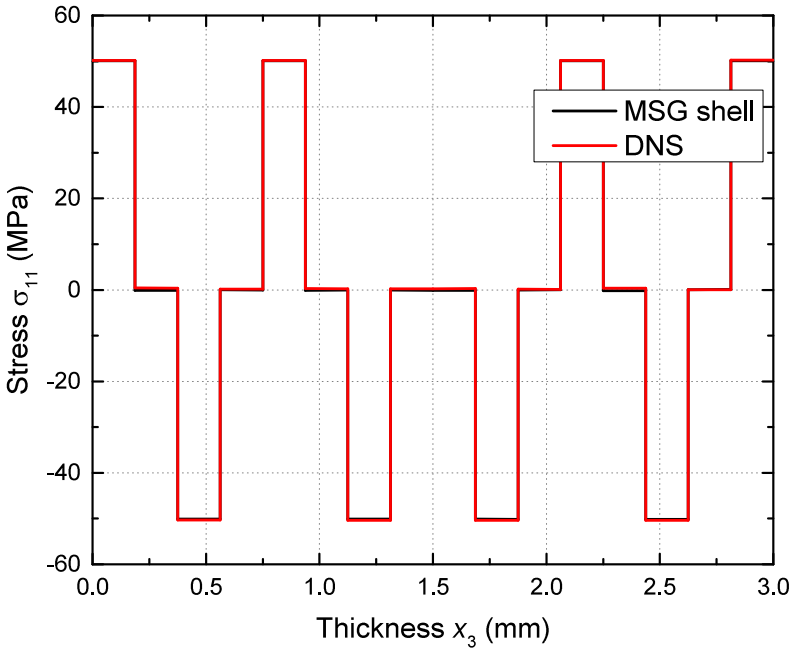

Figure 3.9. Longitudinal normal stress σ_{11} through the thickness at the center of the vertical flat region.

time instants are evaluated based on the temperature and DOC of that instant, and treated as instantaneously elastic within the increment corresponding to that instant. The CHILE model is implemented in the commercial code COMPRO, so in this study, material properties, temperature and DOC are calculated using the thermochemical module of COMPRO, and for a direct comparison between the analysis using MSG-based shell elements and solid elements, those properties are imported to Abaqus with the user subroutine UGENS for the MSG-based shell analysis and UMAT for DNS. As mentioned previously, due to the limitation of Abaqus, varying transverse shear stiffness could not be accommodated for shell elements when using the user subroutine UGENS, so the transverse shear stiffness of the shell model is calculated from final value of the shear moduli. The geometry of the part is similar with the L-shape part in the first example in Section 3.2.2, with the total thickness reduced to 1.488 mm and the flange length increased to 200 mm. Due to increased complexity of the analysis procedure, symmetry of the part is utilized to simplified the model, as shown

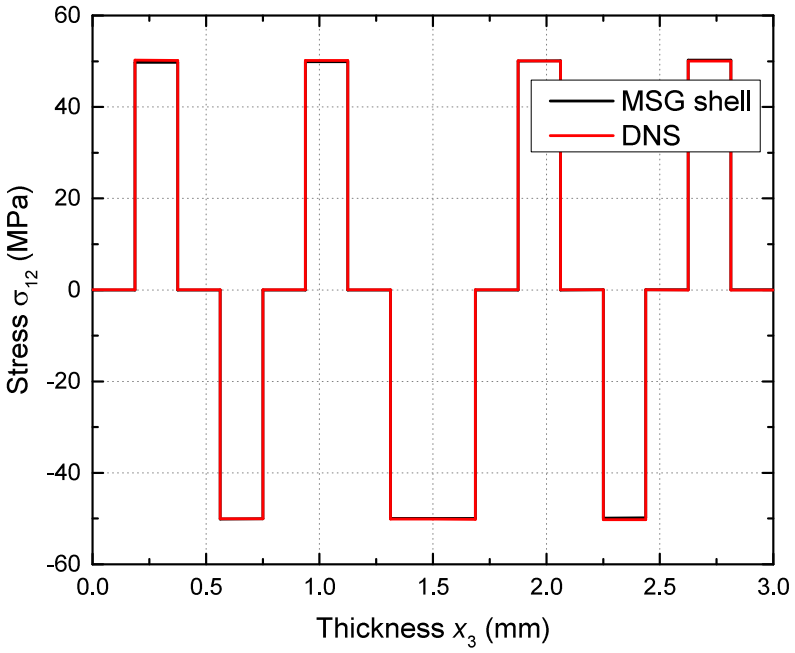

Figure 3.10. Longitudinal shear stress σ_{12} through the thickness at the center of the vertical flat region.

in Figure 3.12. The layup is $[0/90]_{2s}$. Element used in the DNS model is changed to C3D8I for better efficiency. The complete cure cycle lasts 310 minutes, with the first 80 minutes rising the temperature from 20 °C to 180 °C, then holding for 150 minutes, and then cooling down to 20 °C with another 80 minutes. After this process follows the detooling. Normal displacement at the bottom surface of the flat region along the x_2 symmetry line is shown in Figure 3.13. It can be seen that the MSG-based shell analysis can still match the DNS with the CHILE model if the transverse shear moduli G_{13} and G_{23} are fixed as constants, but when compared with varying G_{13} and G_{23}, the shell analysis not only overestimated the displacement, but also failed to capture the curving of the flat surface. The loss of accuracy is caused by the inability of varying transverse shear stiffness of shell elements in Abaqus.

In order to verify that this incorrectness comes from the inability of varying transverse shear stiffness of shell elements during the analysis, we simplify the problem to be solved analytically to avoid the limitation brought by Abaqus. For this purpose, symmetric bound-

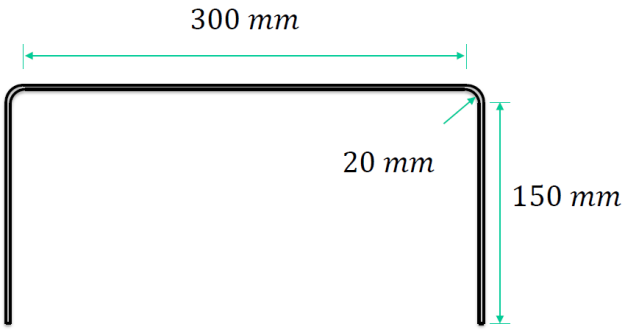

Figure 3.11. Geometry of the C-channel part.

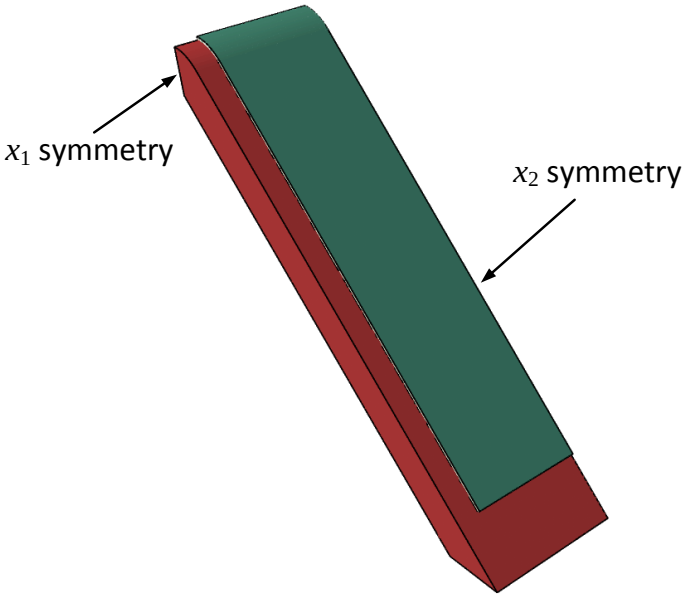

Figure 3.12. Model of the part and tool in Abaqus.

ary conditions on x_2 faces are applied on both sides so that the it becomes a plane strain problem in the x_1-x_3 plane. Also, in order to remove the influence from the deformation of the tool, it is replaced with a frictionless rigid surface. In addition, the analysis procedure returns to the four states in Section 3.2.2, with material properties in each step the same as in Section 3.2.2, except that the transverse shear moduli are also varying, as shown in Table 3.5. Since plane strain condition is adopted, the global shell problem becomes solving a set of ordinary differential equations, as shown in Figure 3.14. The whole process is solved in three steps, representing the transitions among the four states. The solutions of

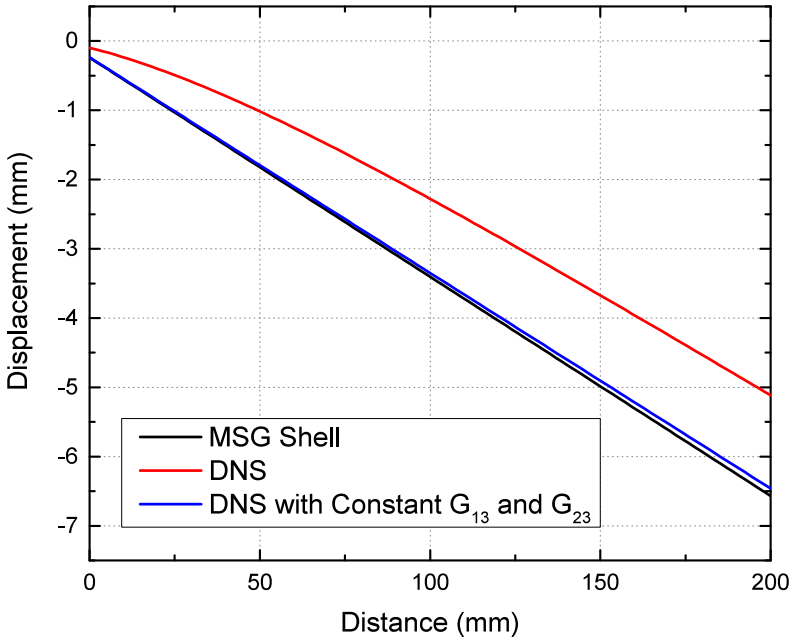

Figure 3.13. Normal displacement u_3 at the bottom surface of the flat region along the x_2 symmetry line.

Table 3.5. Material properties of the composite lamina.

	1st state	2nd state	3rd and 4th state
G_{13} (MPa)	5.75	5.21×10^3	5.21×10^3
G_{23} (MPa)	5.75	3.38×10^3	3.38×10^3

previous steps are used as the initial conditions in the following steps. In the first two steps, the rigid tool is represented by a displacement boundary condition $u_3 = 0$ along the entire length, so contrary to a conventional shell problem that solves for deflection, this problem solves the pressure. The boundary conditions at point A are longitudinal displacement and rotation $u_1 = \phi_1 = 0$, and at point C are section force and moment $N_{11} = M_{11} = 0$. At point B the continuous condition on forces and displacements need to be satisfied. The third step solves the detooling, in which the displacement boundary condition $u_3 = 0$ is removed, and boundary conditions of normal displacement $u_3 = 0$ at point A and transverse shear force $Q_1 = 0$ at point C is introduced. Pressure solved from previous steps becomes the

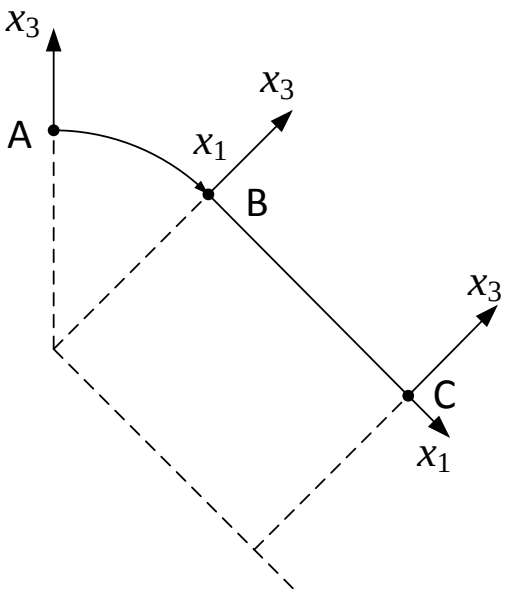

Figure 3.14. Illustration of the global shell problem.

driving force of displacement in detooling. Normal displacement u_3 after detooling is shown in Figure 3.15. It can be seen that even though the error compared with DNS is larger with analytical solution, the curving in the flat region is successfully captured by varying the transverse shear stiffness. To figure out the reason of this underestimation, pressure before detooling is analyzed. By observing the pressure in the curved region and part of the flat region in Figure 3.16, it can be found that the pressure from DNS is continuous at the connecting point between the curved and flat region, while in analytical solution no continuous condition can be applied on pressure or the differential equations can be over-constrained. This results in the difference near the connecting point in the curved region, causing an under estimation of rotation at the connecting point. Since this phenomenon is induced by the difference between the solving technique of FEM and analytical method, a possible method to eliminate this difference is developing a user shell element that allows changing the transverse shear stiffness.

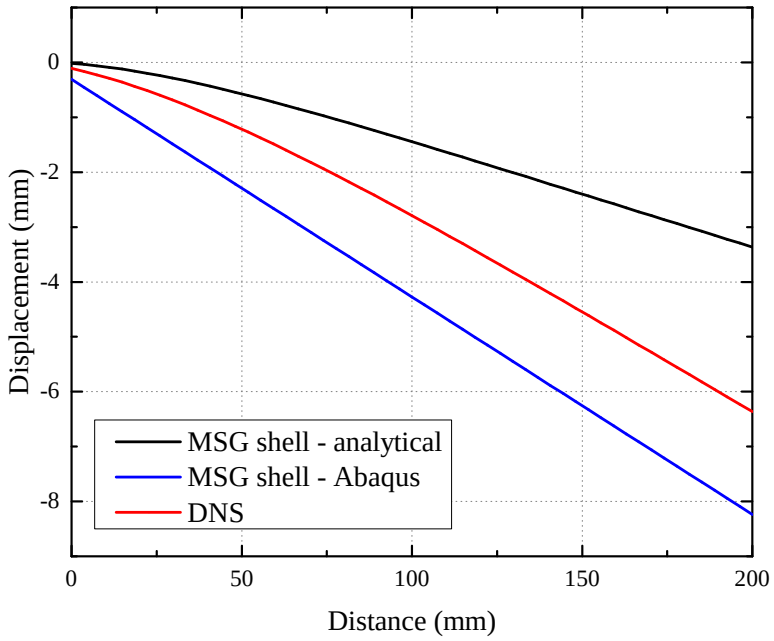

Figure 3.15. Normal displacement u_3 of the flat region.

3.3 Summary

In this chapter, The MSG-based shell theory in Chapter 2 is modified to be applied in composites curing simulation. SG in this chapter is limited to 1D so that formulation of the MSG-based shell theory can be written analytically. Reference surface of the shell is set to be the bottom surface to ensure that the global shell model represent the behavior of the part bottom surface which is contacting with the tool. Geometric corrections and transverse shear stiffness are included to model the behavior that cannot be captured by a classical shell model. The capability of the MSG-based shell theory on capturing curvature change under non-mechanical loading is validated by a unidirectional shell, and in the mean time error in strain recovery is explained. In the same shell geometry, the effect of through-the-thickness temperature change is also captured y the MSG-based shell theory. Demonstrative examples shows the potential of the MSG-based shell theory on predicting spring-in angle of multilayered composites. The influence of varying transverse shear stiffness on composite

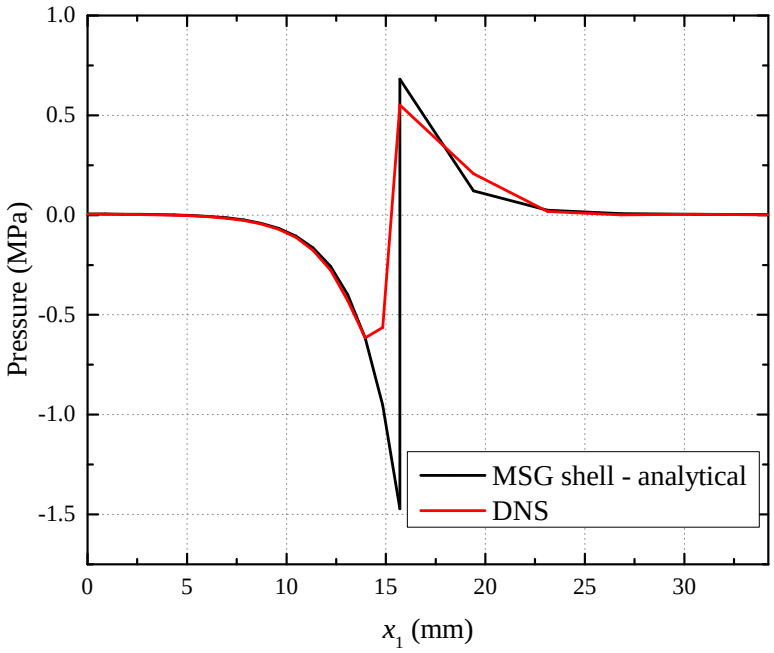

Figure 3.16. Pressure on the shell in the curved region and part of the flat region.

curing simulation is also studied, with the possible solution of developing a user shell element in Abaqus.

4. SIMULATION OF TP-HSC DEPLOYABLE STRUCTURES

4.1 Viscoelastic Material Model

Because of the material property of the polymer matrix and long stowage time before deployment, viscoelastic behavior is commonly seen in TP-HSC deployable structures. As a result, a viscoelastic material model need to be considered for analysing TP-HSC deployable structures. In this chapter, only linear viscoelastic model is considered. General nonlinearities including nonlinear viscoelasticity are considered in next chapter.

Different from an elastic material behavior, behavior of the material becomes time and history dependent when considering viscoelasticity. Without loss of generality, the Boltzmann superposition integral is applied, so that a general statement of linear viscoelasticity can be expressed as

$$\boldsymbol{\sigma}(t) = \int_{-\infty}^{t} \mathbf{C}^{rel}(t-\tau) : \frac{\mathrm{d}\boldsymbol{\Gamma}}{\mathrm{d}\tau}\mathrm{d}\tau \tag{4.1}$$

where t is time, $\boldsymbol{\sigma}$ is the second-order stress tensor, $\mathbf{C}^{rel}$ is the fourth-order tensor of the relaxation moduli. In addition to the strain, tensor $\mathbf{C}^{rel}$ is also a function of time, so an expression of $\mathbf{C}^{rel}$ is necessary to obtained $\boldsymbol{\sigma}$. In experiments, a strain Γ_0 is applied to the specimen, then a curve of the stress history $\sigma(t)$ is recorded, so that the relaxation modulus of the corresponding direction can be calculated with $E_{rel}(t) = \sigma(t)/\Gamma_0$ and fitted to some equations. One method to do this fitting is to use a Prony series, which takes the form

$$E_{rel}(t) = E_{\infty} + \sum_{m=1}^{n} E_m \mathrm{e}^{-t/\rho_m} \tag{4.2}$$

where E_{∞} is the long term modulus, E_m are Prony coefficients, and ρ_m are relaxation times. The elastic modulus E equals to the value of E_{rel} at the start of loading, and obviously,

$$E = E_{rel}(0) = E_{\infty} + \sum_{m=1}^{n} E_m \tag{4.3}$$

Extending Eq. (4.2) to the fourth-order relaxation modulus tensor of a general anisotropic material, terms in $\mathbf{C}^{rel}$ can be expressed as

$$C_{ijkl}^{rel} = C_{ijkl,\infty}^{rel} + \sum_{m=1}^{n} C_{ijkl,m}^{rel} \mathrm{e}^{-t/\rho_m} \tag{4.4}$$

In order to solve the integral equation in Eq. (4.1), three methods are proposed: direct time integration (DI), viscoelastic correspondence principle, and quasi-elastic (QE) method [112]. The DI method is the most straight forward method, in which Eq. (4.1) is transformed into an incremental form, and the stress increment can be expressed as [113]

$$\Delta\sigma_{ij} = C_{ijkl}^{T} \Delta\Gamma_{kl} + \Delta\sigma_{ij}^{R} \tag{4.5}$$

where C_{ijkl}^{T} are terms of the tangent stiffness tensor calculated from the Prony series, $\Delta\sigma_{ij}^{R}$ are history dependent stresses. The DI method can provide solution for general loading cases, but the implementation is relatively difficult compared with the other two methods. The viscoelastic correspondence principle utilizes the existing solution of an elastic problem spatially similar to the viscoelastic problem to be solved. Using a Laplace transform, equations and boundary conditions are transformed from time domain to Laplace domain, and then the problem can be solved with an elastic solution, and the final solution of the original viscoelastic problem can be obtained by an inverse transform. When a corresponding elastic solution exist, this method is easy to implement and the accuracy is guaranteed. However, it is limited by the boundary conditions, as the boundary condition can be altered during the Laplace transform and its inverse. The QE method use the elastic constitutive equation to approximate Eq. (4.1), with the elastic stiffness tensor replaced by the relaxation moduli tensor [114]. Compared with the other two methods, this is the simplest one as the integral in time domain is completely eliminated. On the other hand, this simplification makes the QE method provides accurate results only in the case that the strain input is a step function $\mathbf{\Gamma}(t) = \mathbf{\Gamma}_0 H(t)$, because

$$\boldsymbol{\sigma}(t) = \int_{-\infty}^{t} \mathbf{C}^{rel}(t-\tau) : \mathbf{\Gamma}_0 \frac{\mathrm{d}H(\tau)}{\mathrm{d}\tau} \mathrm{d}\tau = \mathbf{C}^{rel}(t) : \mathbf{\Gamma}_0 H(t) \tag{4.6}$$

where $H(t)$ is the Heaviside step function. The step function strain input is common in material testing experiments, as well as constitutive modeling considering viscoelastic properties. Thus the QE method is the simplest and most efficient approach for these applications.

In this chapter, linear viscoelastic material model is applied in the MSG-based shell theory for the simulation of TP-HSC. The effective shell properties can be otained using the MSG-based homogenization tool SwiftComp [41], and fitted into Prony series. They are implemented in Abaqus UGENS with either QE or DI methods. The QE implementation is straightforward, similar to an elastic material, with the main difference being the material properties being functions of time. The DI implementation is based on the theory developed by Rique Garaizar [115]. The formulation follows the form of classical shell model, in which increments of the shell sectional forces ΔN and moments ΔM are calculated using

$$\begin{aligned} \Delta N\left(t_{n+1}\right) &= A_{eq}\Delta\epsilon\left(t_{n+1}\right) + B_{eq}\Delta\kappa\left(t_{n+1}\right) + \Omega_N \\ \Delta M\left(t_{n+1}\right) &= B_{eq}\Delta\epsilon\left(t_{n+1}\right) + D_{eq}\Delta\kappa\left(t_{n+1}\right) + \Omega_M \end{aligned} \tag{4.7}$$

where A_{eq}, B_{eq}, and D_{eq} are equivalent tangent stiffness matrices calculated from the Prony series of the equivalent shell properties, $\Delta\epsilon$ is the membrane strain increment, $\Delta\kappa$ is the curvature increment, Ω_N and Ω_M are column matrices determined from the loading history, and t_{n+1} is the time at increment $n+1$. Sectional forces and moments at the end of the current increment are obtained by adding the increments ΔN and ΔM to the sectional forces and moments from the previous increment. Details of the derivation of Eq. (4.7) can be found in [115].

Although the formulation of linear viscoelasticity was originally developed for small strain condition, the strain measurement in the formulas can also be logarithmic strain. In the simulation of TP-HSC deployable structures, since the geometric nonlinearity can be handle by the global structural solver Abaqus, and in Abaqus when geometric nonlinearity is enabled, logarithmic strain will be used, the current formulation will be enough for the strain level observed in TP-HSC deployable structures. Finite strain formulation is unnecessary unless large shear and local rotation are observed.

4.2 Column Bending Test Simulation

In this section, simulation of the CBT is presented. The model setup in Abaqus is introduced, and results of moment relaxation, energy dissipation, and residual deformation are demonstrated. The CBT is developed at Opterus R&D and improved by NASA Langley Research Center (LaRC) [5], [77] to evaluate the flexure of thin composites. This test method loads the specimen in the vertical direction, generating a stress state close to pure bending. In the CBT, the specimen is vertically clamped by upper and lower arms, which are pinned inside clevises. An initial angle θ exists between the arms and the loading direction, creating an offset between the specimen and the loading axis. Due to this offset, when the clevises move towards each other, a moment is generated and the specimen bends. A schematic of the CBT is shown in Figure 4.1, with the angle θ, arm length l and gauge length s known, clevis displacement δ and applied load P controlled or measured, and angle change ϕ and offset r calculated. In addition to these values shown in Figure 4.1, the width of the specimen d is also a known parameter.

The test consists of four different load steps that represent the conditions similar to the stowage of a boom: folding, relaxation, unfolding and recovery. In the initial folding step, the specimen is bent to a set curvature that is representative of the boom during stowage. In the relaxation step, the specimen is kept at a constant strain for six hours. Then, in the unfolding step the specimen is unfolded to a zero-load condition. Finally, during the creep recovery step, it is held at zero-load condition. Time of the steps are shown in Table 4.1.

Table 4.1. Step time of the CBT.

Step	Folding/Unfolding	Relaxation	Recovery
Time t (s)	120	21,600	7,200

4.2.1 Data Reduction

The deformation of the specimen in CBT is designed to have a small gradient from the grip to the center, with the center having the largest deformation and moment. This ensures failure of the specimen occurs at the center during a failure test. The experimental results

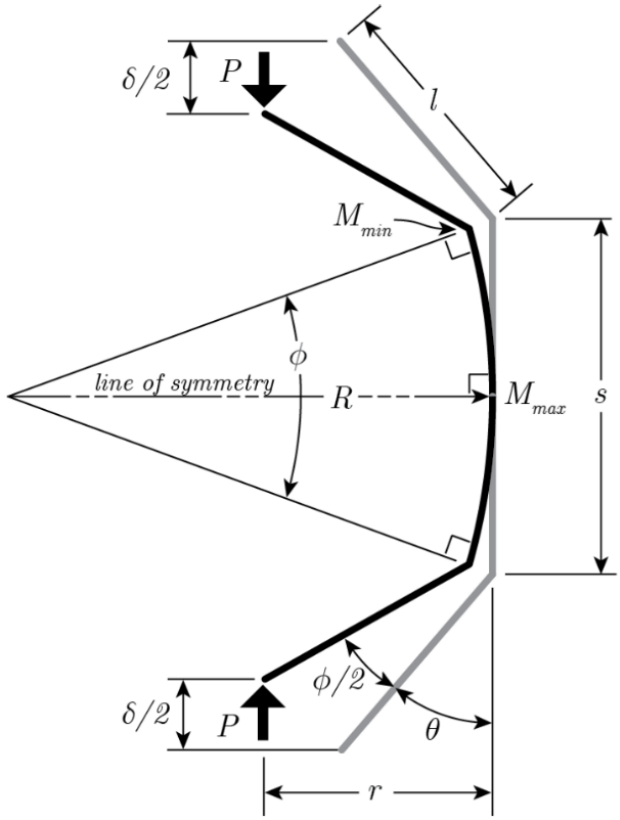

Figure 4.1. Schematic of the CBT with the thick gray lines showing the initial configuration and the thick black lines showing the deformed configuration [77].

are processed using kinematic relations [77] from the load and displacement measurements as summarized in the following. The specimen curvature κ is computed using the total fixture arm rotation angle change ϕ and specimen gauge length s

$$\kappa(t) = \frac{\phi(t)}{s} \tag{4.8}$$

Notice that Eq. (4.8) implies the assumption that the curvature is uniform along the gauge length, as it is based on the arc length formula. Angle change ϕ can be calculated using the following formula

$$\frac{\delta}{s} = 1 - \frac{2}{\phi}\sin\frac{\phi}{2} + 2\frac{l}{s}\left(\cos\theta - \cos\left(\theta + \frac{\phi}{2}\right)\right) \tag{4.9}$$

For the simplicity of notation, dependency of time is not explicitly shown here and in the following equations. For evaluating the effective stiffness, the moment in the specimen also

needs to be calculated. The maximum moment M_{max} at the middle of the gauge length can be calculated with the load P and offset r

$$M_{max} = Pr \tag{4.10}$$

with the load P being measured at the loading head, and offset r calculated with

$$\frac{r}{s} = \frac{1}{\phi}\left(1 - \cos\frac{\phi}{2}\right) + \frac{l}{s}\sin\left(\theta + \frac{\phi}{2}\right) \tag{4.11}$$

then the effective stiffness D_{11}^* is calculated using

$$D_{11}^* = \frac{M_{max}/d}{\kappa} \tag{4.12}$$

In experiments, the full-field curvature can be measured directly with Digital Image Correlation (DIC). The DIC curvature data is averaged within a rectangular region of interest (R0) near the center of the specimen, as shown in Figure 4.2. Due to the nonuniform

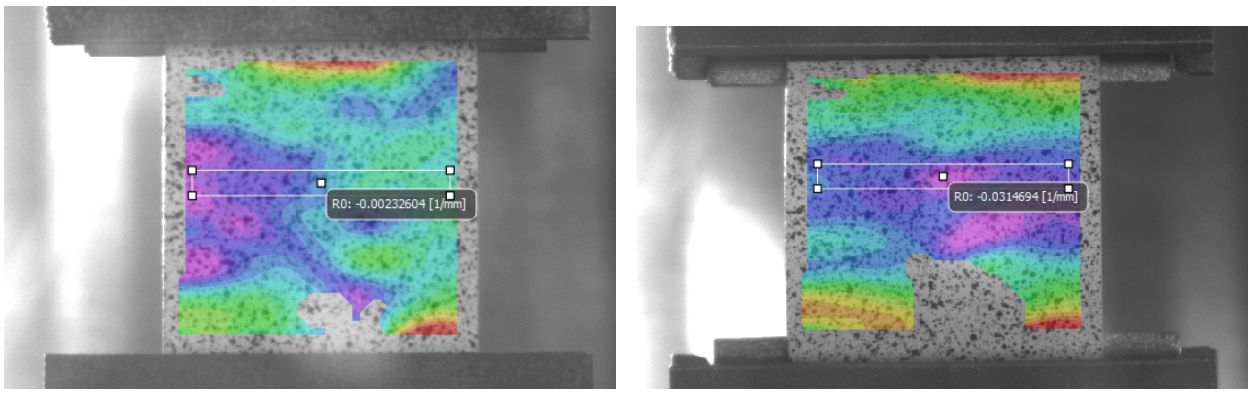

(a) Before folding. (b) After folding.

Figure 4.2. DIC image of a specimen and the rectangular region of interest for averaging [116].

deformation, the curvature obtained from DIC is closer to the maximum curvature in the specimen, while the curvature calculated from Eq. (4.8) is closer to the average curvature of the whole specimen.

4.2.2 Finite Element Model of CBT

A finite element model for simulating CBT is built with Abaqus. By reproducing experimental results, effectiveness of the modeling technique and user subroutines can be validated, so that realistic models of TP-HSC structures such as a deployale boom structure can be studied. The CBT finite element model in Abaqus CAE [117] is shown in Figure 4.3. The specimen between the clamps is modeled with fully integrated four-node shell elements S4, and the clamped regions are neglected. In this model, total number of shell elements is 2,800, but due to the simple geometry, the model is not sensitive to mesh density. This is verified by a coarse mesh with 700 elements. Both meshes give the same normal displacement of 25.01 mm at the center of the specimen. The mesh with 2,800 elements is used for providing more data points reflecting the nonuniform deformation. The pins are represented by two reference points. The lower reference point (RP-1) is fixed in all degrees of freedom (DOFs) except rotation about the x-axis. The upper reference point (RP-2) allows rotation about the x-axis and displacement in the y-direction with the other DOFs held constant. Kinematic couplings are applied between the upper and lower edge of the specimen and the corresponding reference points RP-1 and RP-2, as shown in Figure 4.3 by the blue lines. These couplings connect the displacement of the edges with those of the reference points rigidly, and ensure that the edges have the same rotation as the corresponding reference points to mimic the fixture arms in the experiments.

The analysis includes four loading steps: folding, relaxation, unfolding, and recovery. The experiment of CBT is a quasi-static process so all of the steps are implemented as general static steps in Abaqus. In the folding step, end shortening, implemented through a y-displacement boundary condition, is applied to RP-1 such that the specimen bends. Then, this configuration is kept constant for a specified period of time to allow stress relaxation. After relaxation, the displacement boundary condition in the y-direction at RP-1 is removed, so that the reaction forces at the reference points become zero and the specimen is unfolded by its internal stress. It is noted that the boundary condition change in the model is instantaneous, while, in the test, a prescribed displacement rate was applied until zero load is

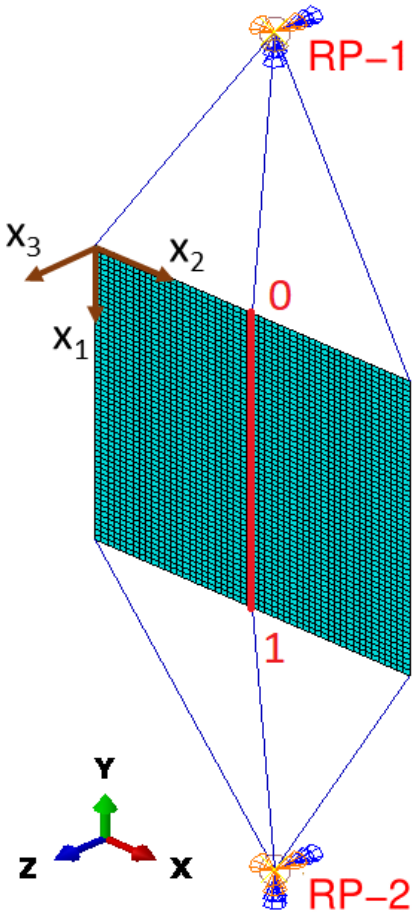

Figure 4.3. CBT model in Abaqus CAE.

reached. The unfolded configuration is also kept for some time, during which the specimen gradually recovers its original shape. Geometric nonlinearity is enabled in all the steps.

The specimen and test parameters of the CBT model shown in Table 4.2 are used in order to compare with existing experimental data [118]. The displacement in the folding step is applied at a rate of 12.7 mm/min, resulting in a load time of 2 min (the same rate was used in the test for unfolding), and the times for relaxation and recovery are 6 hours and 2 hours respectively.

The CBT specimens are constructed using M30S/PMT-F7 plain weave plies with layup $[\pm 45]_4$ and the material directions x_1, x_2, x_3 shown in Figure 4.3. The carbon M30S fiber is treated as an elastic material and the PMT-F7 toughened epoxy resin is assumed to be linear viscoelastic. The Prony series coefficients of the PMT-F7 resin were fit to the experimental

Table 4.2. Specimen and test parameters of the CBT model.

CBT fixture arm length l (mm)	25.4
Specimen width d (mm)	25.4
Specimen gauge length s (mm)	27.432
Fixture arm initial angle θ (rad)	0.0712
Fixture total displacement δ (mm)	25.4
Specimen thickness h (mm)	0.276

data obtained by LaRC [5]. For woven composites, effective properties can be obtained using MSG through a two-step homogenization [41] that first calculates the effective yarn properties in terms of the fiber and matrix properties, and then the effective shell properties of the woven fabric are obtained using the yarn and matrix properties. The effective A, B, D matrices are written as Prony series coefficients, shown in Table 4.3.

Table 4.3. Prony series coefficients of the shell stiffness matrix for $[\pm 45_{PW}]_4$ layup [119].

s	λ_s	$A_{11,s}$ (N/mm)	$A_{12,s}$ (N/mm)	$A_{66,s}$ (N/mm)	$D_{11,s}$ (N·mm)	$D_{12,s}$ (N·mm)	$D_{66,s}$ (N·mm)
∞	–	10,930.00	10,000.00	10,110.00	47.33	43.34	43.79
1	37.0	145.40	23.83	44.08	0.63	0.10	0.19
2	10^2	128.50	23.59	42.00	0.56	0.10	0.18
3	10^3	108.10	19.69	35.12	0.47	0.08	0.15
4	5×10^3	46.32	9.37	16.14	0.20	0.04	0.07
5	10^4	47.54	8.50	15.25	0.20	0.04	0.06
6	5×10^4	131.80	26.94	46.24	0.57	0.12	0.20
7	10^5	12.80	2.90	4.81	0.05	0.01	0.02
8	5×10^5	66.90	14.25	24.13	0.30	0.07	0.11
9	10^6	39.40	9.12	15.06	0.16	0.03	0.06
10	5×10^6	0.44	0.08	0.14	0.01	0.00	0.00

In order to directly compare with experimental results, data reduction consistent with the experiments is necessary for simulation. The curvature of the specimen κ can be calculated using Eq. (4.8), but instead of using Eq. (4.9), the fixture arm rotation angle change is obtained from the rotation of the reference point ϕ_{rp}, and calculated as $\phi = 2\phi_{rp}$[1]. Alternatively, for comparing with the DIC data, κ can also obtained through averaging across

[1]↑Comparison of using Eq. (4.8) and Eq. (4.9) vs. Eq. (4.8) with ϕ_{rp} showed the difference was less than 1%.

all the elements inside a rectangular region near the center. When calculating the moment M_{max}, the load P in Eq. (4.10) equals to the vertical reaction force output at the reference point of Abaqus, and moment arm r can be calculated with

$$r = u_3 + r_0 \tag{4.13}$$

where u_3 is the normal displacement at the center of the specimen obtained from Abaqus and r_0 is the initial offset. Notice that the moment obtained with the r from Eq. (4.13) is closer to the maximum moment in the specimen as it does not imply the uniform curvature assumption.

4.2.3 Results

The curvature history during the folding step is shown in Figure 4.4 and 4.5 with the dashed lines showing the analysis results and the solid lines showing the experimental results. In Figure 4.4, Eq. (4.8) is used, and in Figure 4.5 data from the center region R0 is used. It can be seen that the results from simulations match well with those computed using the kinematic formulas, and follow the same trend as the experiments, with their magnitudes being close, having some overprediction. The simulation results using QE and DI methods overlap each other.

The nonuniform distribution of curvature in the folded specimen is captured by the simulation, as shown in Figure 4.6. The simulation result for the curvature κ_{11}, after folding along the center (red) line in Figure 4.3 is shown in Figure 4.7, with the distance normalized by the specimen gauge length. The curvature κ_{11} at the center is 0.071 mm^{-1}, which is 34% larger than the value of 0.053 mm^{-1} at the upper and lower edges. The specimen curvatures after folding obtained by different methods are shown in Table 4.4. The DIC result is averaged from four sets of experiments. Experiment average column of the kinematic row refers to the results from Eq. (4.8) and (4.9). The measured and predicted curvatures calculated with kinematic formulas match well with each other. However, the curvature from the center rectangular region of the simulation is 15.4% larger than the DIC results. The DIC data obtained from the center, representing the maximum curvature, is smaller than

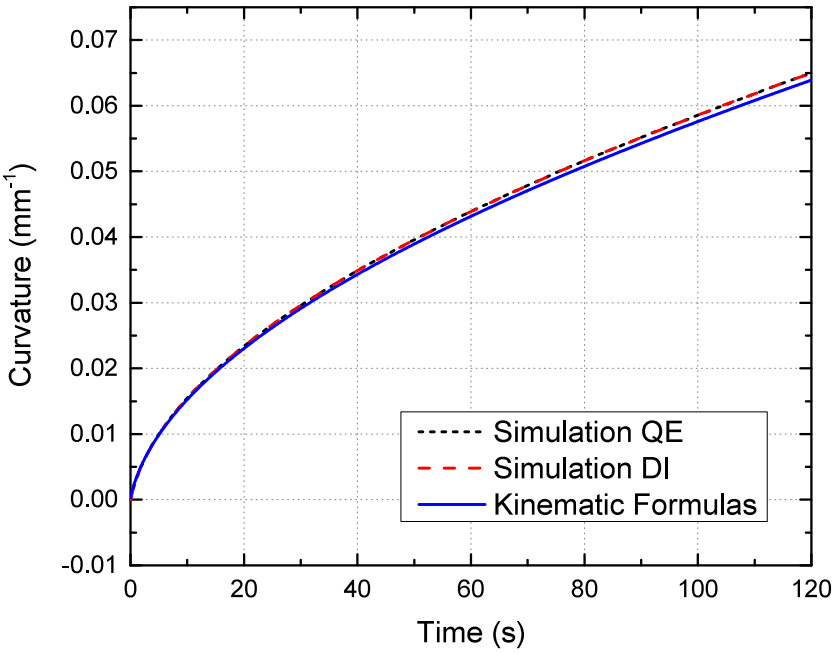

Figure 4.4. Curvature history during folding with kinematic formulas.

curvature from the kinematics formula, which is representative to the average. A possible explanation could be the boundary condition at the clamps. In the kinematic formula and the finite element model, the upper and lower edges of the specimen have the same rotation as the corresponding loading head, which means the clamping at the edges are perfectly rigid that completely eliminate relative rotation. However, a rigid clamp is hard to achieve in experiments, and relative rotation can happen between the clamp and the specimen edge. Nonetheless, curvature averaged across the center rectangular region is used in the following.

Table 4.4. Specimen curvature (mm^{-1}) after folding.

Method	Exp. avg.	Exp. CoV	Simulation	Error
Kinematic	0.06387	N/A	0.06500	1.8%
Center region	0.06127	1.4%	0.07070	15.4%

The simulation results also captured the nonuniform distribution of the shell section moments M_{11} and M_{22}, as shown in Figure 4.8. In addition to the variation in the gauge length

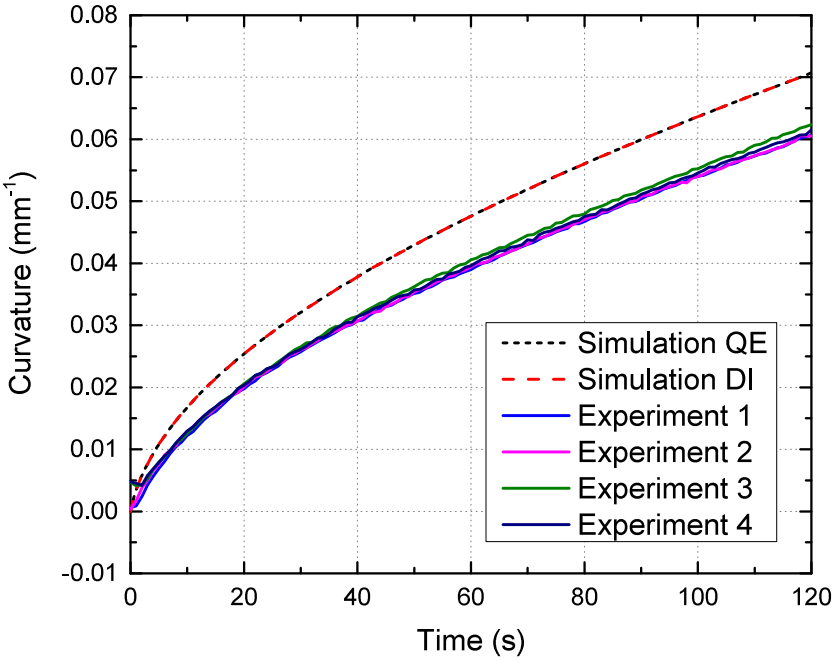

Figure 4.5. Curvature history during folding with center R0 region.

direction, the moments also vary in the width direction. Figure 4.9 shows the history of the moment M_{max} during relaxation. The simulation results lie within the range of experimental curves. Again, the QE and DI results match exactly, which verifies the effectiveness of the QE implementation for predicting the CBT relaxation.

The history of D_{11}^* during relaxation is plotted in Figure 4.10. It can be observed that the simulation underpredicts the experimental data. Since the moment relaxation is well predicted, as shown in Figure 4.9, the underprediction is likely caused by the overprediction of the curvature at the end of the folding that can be seen in Figure 4.5. It should be emphasized that the effective stiffness D_{11}^* is different from the D_{11}, which is a term of the shell section bending stiffness D, with the value shown in Table 4.3. A comparison between D_{11}^* and D_{11} before and after relaxation is shown in Table 4.5. The D_{11}^* obtained from simulation is 8.3% smaller than the D_{11} before relaxation and 9.5% smaller after relaxation.

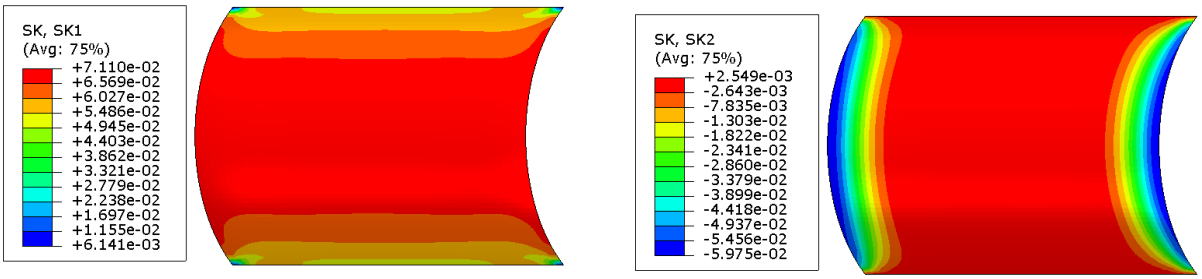

(a) Contour plot of curvature κ_{11} at the start of relaxation.

(b) Contour plot of curvature κ_{22} at the start of relaxation.

Figure 4.6. Non-uniform distribution of curvature in the specimen.

Table 4.5. Comparison between D_{11}^* and D_{11} (N · mm).

	Before relaxation	After relaxation
D_{11}^* simulation DI	45.3	43.6
D_{11}^* exp. avg.	51.5	49.9
D_{11}	49.4	48.2

This can be explained by the nonuniform deformation and the small but non-negligible curvature κ_{22}, as shown in Figure 4.6.

In order to evaluate the capability of the present method of predicting the residual deformation, the predicted and measured curvatures are compared in the unfolding and recovery stages, as shown in Figure 4.11. After taking the unloading process into consideration, the whole loading history is no longer a step function. In this case the QE implementation is not able to capture any residual deformation, so it is not shown here. The DIC data from experiment 2 for the unfolding and recovery steps is not available due to a lighting issue. The comparison of residual deformation after relaxation shows disagreement, especially in the final steady-state curvature. The curvature values during relaxation, after unfolding and after recovery are shown in Table 4.6. The curvature in the "After unfolding" column of Table 4.6 is approximate because the time resolution of the DIC is 30 s, relatively large compared with the total unfolding time, and there are time lags between the DIC and the loading frame.

Observing the curve in Figure 4.11, one possible cause for the disagreement in residual curvature is viscoplasticity, as the disparity between the computed and experimental results is

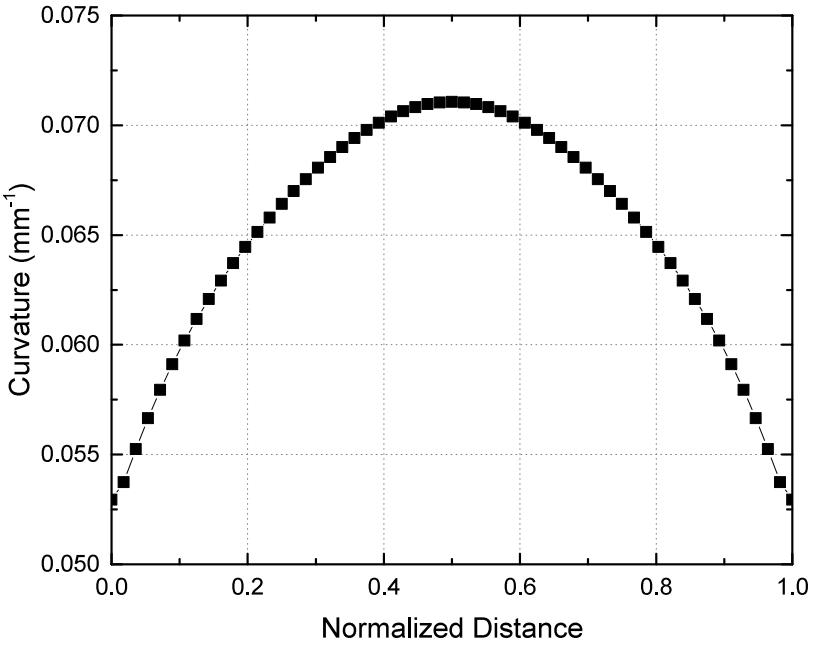

Figure 4.7. Curvature κ_{11} along the vertical center line.

Table 4.6. Residual curvature after relaxation (mm^{-1}).

Curvature	Relaxation	After unfolding (Approx.)	After recovery
Simulation	0.07075	0.004859	0.0007431
Exp. avg.	0.06181	0.007605	0.004998
Error	14.5%	-36.1%	-85.1%

relatively constant through the recovery period. The large strains imposed on the specimens during the CBT likely caused some degree of plastic deformation. To understand the effect of viscoplasticity, future work should consider a viscoplastic material model and a nonlinear shell model as well be attempted in the next chapter.

4.2.4 Demonstration of Calibration

The CBT simulation also has the potential to be used for the calibration of material properties. To demonstrate this capability, a calibration of the shell bending stiffness in the axial x_1-direction D_{11} is carried out. This calibration does not involve MSG homogeniza-

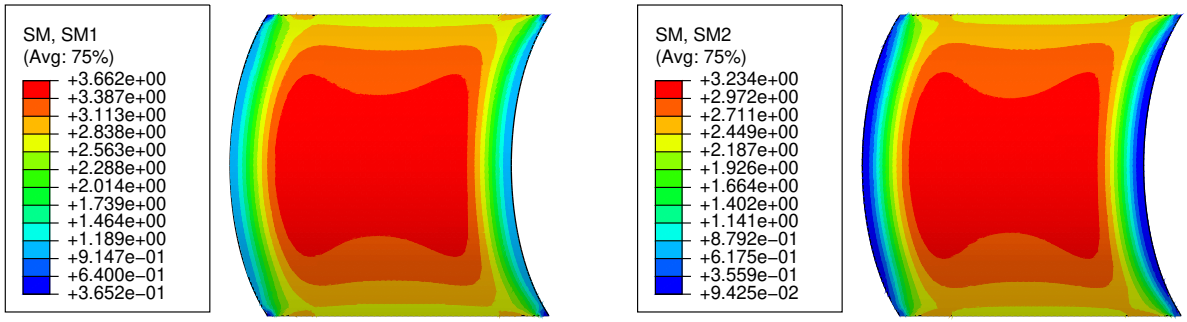

(a) Contour plot of section moment M_{11} at the start of relaxation.

(b) Contour plot of section moment M_{22} at the start of relaxation.

Figure 4.8. Nonuniform distribution of section moments in the specimen.

tion, but it can be integrated into the algorithm in future work to calibrate resin material properties. In this study, only D_{11} is calibrated, and other terms in the D matrix are held constant. The A matrix is estimated based on the relation

$$A_{ij} = D_{ij}\frac{12}{h^2} \tag{4.14}$$

where h is the thickness of the specimen. The parameters to be calibrated are $D_{11,m}$ with $m = 1$ to 6, indicating the six terms in the Prony series. The summation of all terms is kept constant during calibration, so that $D_{11,\infty}$ can be calculated. The calibration is conducted using the Dakota optimization software [120] as follows. At the beginning of the calibration, an initial value for D_{11} is written into a UGENS by Dakota, and this UGENS is used for a CBT simulation in Abaqus. After that, a post-processing script computes the effective bending stiffness D^*_{11}, which is a time-dependent curve and it can be directly compared with the experimental results. In this case, the average of the four experimental curves is used. An error is evaluated using error sum of squares (SSE)

$$SSE = \sum \left(D^*_{11,simulation} - D^*_{11,experiment}\right)^2 \tag{4.15}$$

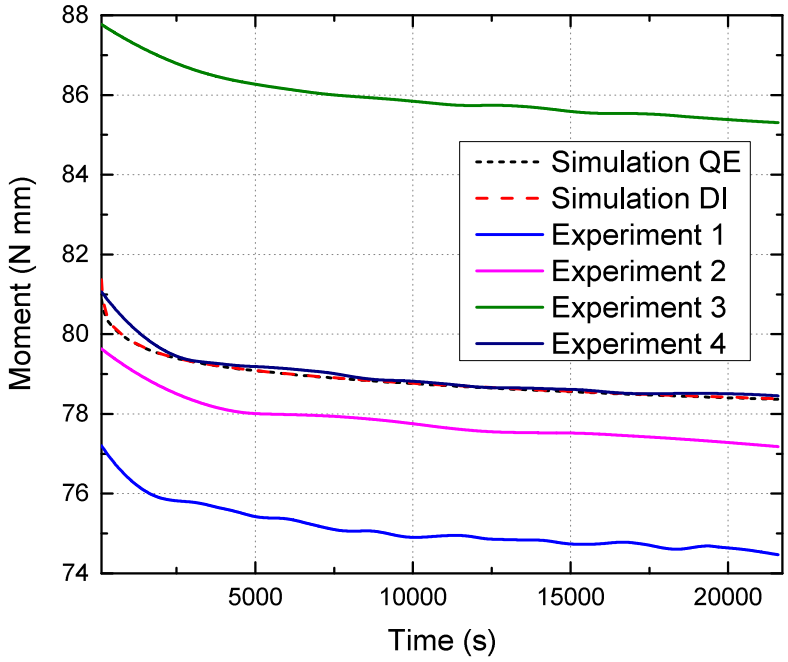

Figure 4.9. History of moment M_{max} during relaxation.

and the SSE is passed to Dakota, based on which a new set of $D_{11,m}$ is generated and the UGENS is updated. This iteration process is repeated until the SSE is converged to a minimum or the number of iterations reaches a preset value.

In this case study, calibration is judged converged by Dakota after 480 iterations, with the best results obtained at iteration 465. SSE history is shown in Figure 4.12. The initial SSE is 99.4, and after calibration, SSE is minimized to be 1.6. It can be seen that the SSE is, for practical purposes, converged after about 250 iterations. Initial values at iteration 1 of the Prony series coefficients of D_{11} and the values after calibration at iteration 465 are shown in Table 4.7. A longer relaxation time is chosen for the sixth term considering that potential applications can have stowage time of years. The D_{11}^{*} during relaxation is shown in Figure 4.13 for the initial material model, the calibrated material model, and the average of the experiments. It can be observed that compared with the initial properties, using the

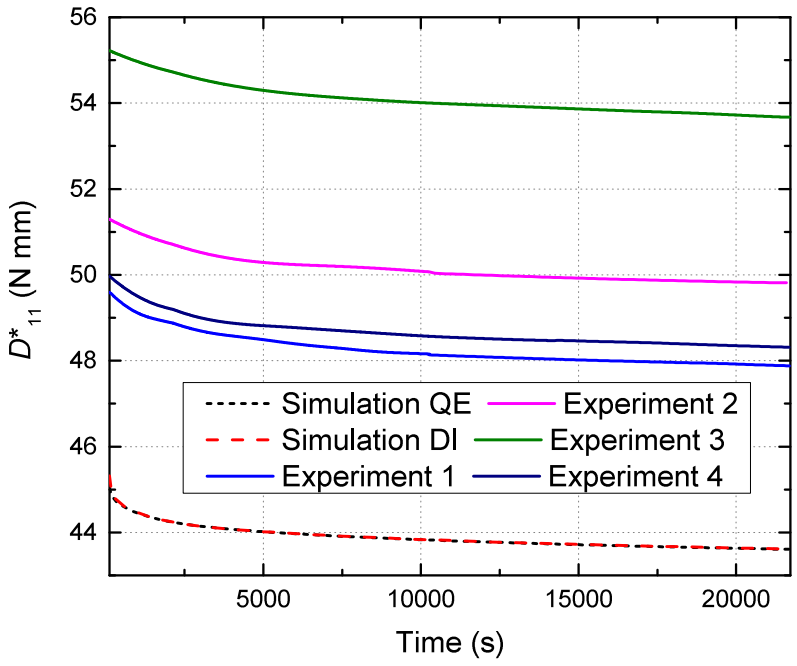

Figure 4.10. History of effective bending stiffness D^*_{11} during relaxation.

calibrated data makes D^*_{11} have a faster relaxation and a smoother change of the relaxation rate, agreeing with the experiment better.

4.3 Simulation of a Hub and TP-HSC Boom Deployable Structure

To understand the viscoelastic behavior of TP-HSC in deployable boom structures, both the boom and coiling hub need to be simulated to study the effect of coiling, stowage, and deployment. The boom is coiled to the hub by wrapping around it. This coiled configuration is kept during stowage, which can be as long as several years. For deployment, the hub is rotated in the opposite direction and the boom unwraps to its natural extended form. Differences in the boom's cross-section after deployment and recovery due to the viscoelastic-viscoplastic nature of the constituent TP-HSC materials can have a large impact on the structural performance of the boom. For simulating this process, the boom is modeled using

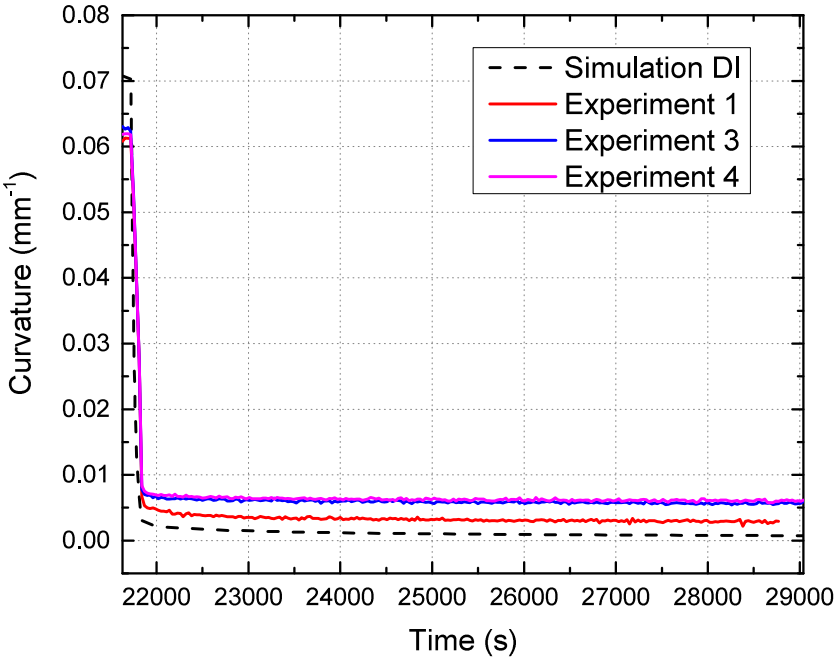

Figure 4.11. Residual curvature after relaxation.

shell elements and the hub by a rigid cylindrical surface. Compared to the high flexibility of the boom, the hub has a much larger stiffness, so it can be modeled as a rigid body.

In this study, the boom has a lenticular cross-section, which consist of two Ω-shaped shells bonded together along flat regions called the webs. Geometric parameters of the cross-section are listed in Table 4.8, with the definition of the various shell segments based on [121], as shown in Figure 4.14. Notice the subtended angles of segment 1 and 2 have to be the same because of continuity. The layup in segment 1 consists of a unidirectional axial ply between two off-axis plain weave plies, $[45_{PW}/0_{UD}/45_{PW}]$. In segment 2 and the web, the layer of plain weave composite on the inner side of the boom is dropped. In the web, a layer of epoxy film is added for joining the two shells together. Both the epoxy film and plain weave composites are considered viscoelastic materials. In the finite element model, these three sections have different effective properties due to different layups and materials. The length of the boom is 880 mm and the radius of the hub is 90 mm.

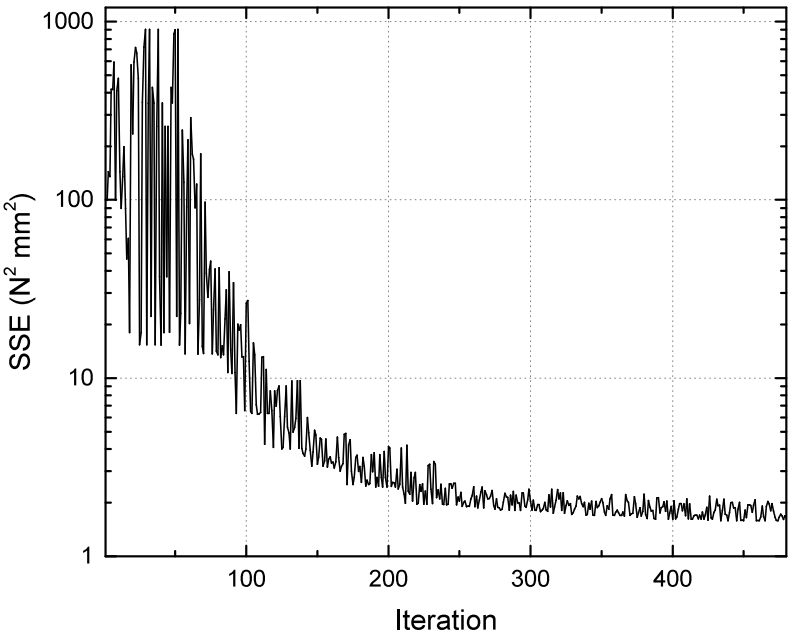

Figure 4.12. Error sum of squares (SSE) history for D_{11}^{*} calibration.

Due to the complexity of the problem, some simplifications have been adopted to avoid convergence issues. The finite element model of the deployable boom structure is shown in Figure 4.15. In addition to the boom and the hub, two rigid plates are also included in the model to facilitate the modeling of the boom coiling and deployment processes. Different from reality, the whole boom is flattened all together by moving the rigid plates towards each other, so that convergence limitations caused by local buckling during the transition from the lenticular cross-section to the flattened cross-section in the boom segment near the hub can be avoided. This modeling technique can be justified as coiling and deployment are finished in a short time compared to the stowage time. The way this simplified flattening process occurs has little impact on the total energy dissipation, which is the main source of residual deformation. To also ensure convergence, an implicit dynamic quasi-static step is used in Abaqus/Standard for flattening, coiling and deploying steps, while a general static step is used for stowage step for better accuracy. A kinematic coupling between a reference point located at the center of the hub and the nodes at the hub-end of the boom is applied as

Table 4.7. Prony series coefficients of D_{11} before and after calibration.

s	λ_s	$D_{11,s}$ (N·mm)	
		Initial	After calibration
∞	–	49.501800	50.149425
1	10	0.076000	0.091625
2	10^2	0.513000	0.575500
3	10^3	0.434500	0.238750
4	10^4	0.217800	0.946550
5	10^5	0.487300	0.208550
6	10^8	1.000000	0.020000

Table 4.8. Cross-sectional geometric parameters of the lenticular boom.

Segment 1 Radius (mm)	Segment 2 Radius (mm)	Subtended Angle (°)	Flattened Height (mm)	Web Width (mm)
26.5	12	90	130	4.5

the driver for coiling and deployment. After the boom is flattened, rotation is only applied to the reference point at the center of the hub while the hub itself remains fixed, acting as a rigid support for the boom to slide on during the coiling process. This technique avoids applying multiple contacts to fix the boom on the hub, and thus reducing complexity of the model. A tension force of 104 N in the z-direction is applied on the free end of the boom at the start of coiling and kept until the deployment is finished. The flattening plates are also kept in place until deployment is finished. These features greatly help stabilize the model during deployment so that convergence can be improved. During coiling and deployment, the hub is rotated with an angular velocity of 40 rad/s (382 rpm), which is much higher than the speed of 1 rpm in the real application. Counter-intuitively, it is observed that using a high rotational speed stabilizes the structures more, which allows a larger increment size that reduces the computational cost, and makes convergence issues occur less frequently. This may be caused by the way Abaqus/Standard handles the numerical damping in a quasi-static analysis. The adoption of a fast rotational speed can also be justified by the relatively short time of coiling and deployment compared with the stowage and recovery times. For obtaining numerical results, a stowage time of 30 days was used, and a recovery free-standing

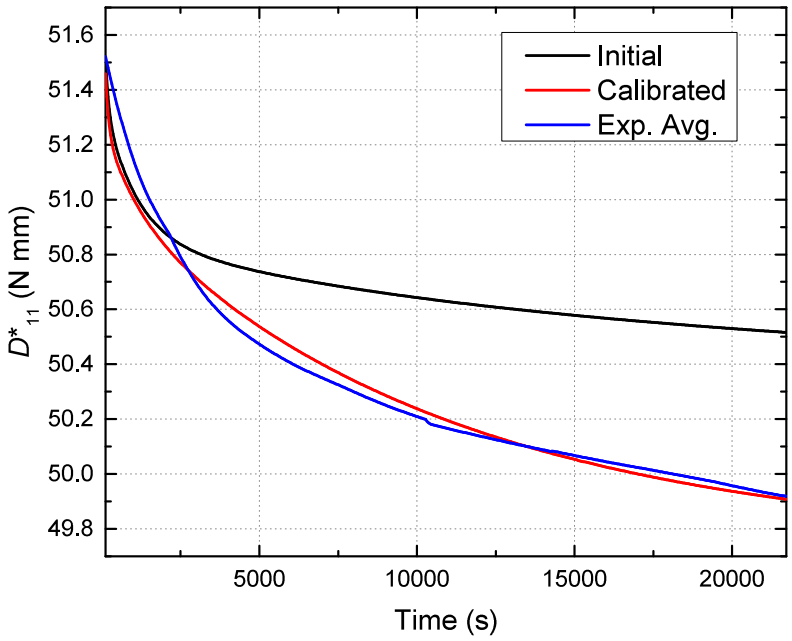

Figure 4.13. History of effective bending stiffness D^*_{11} during the relaxation step before (initial, iteration 1) and after calibration.

period of 24 hours was considered after deployment. This model is referred to as the baseline model, as an improved version of the model is introduced below.

To investigate the effect of long stowage time, effective viscoelastic shell properties with the DI implementation in the UGENS is used. Contour plots of the residual curvature in both directions after the 24-hour recovery are shown in Figure 4.16. There is no obvious residual curvature in the longitudinal direction ($SK1$), while residual curvature with different signs in segments 1 and 2 can be observed in the hoop direction ($SK2$). A plot of $SK1$ along the symmetry line of the inner shell (shell closest to the hub) is shown in Figure 4.17 and referred to as the baseline model. Likewise, a plot of $SK2$ along the Ω-shaped hoop line at the midspan of the inner shell is shown in Figure 4.18.

From Figure 4.17 it can be seen that residual curvature in the longitudinal direction only exists at the boom free ends, which is caused by the boundary effects. Considering the short length of the boom, and also its high structural stiffness if treated as a beam, it

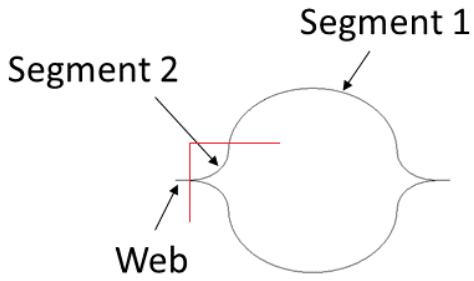

Figure 4.14. Lenticular boom cross-section showing the various shell segments.

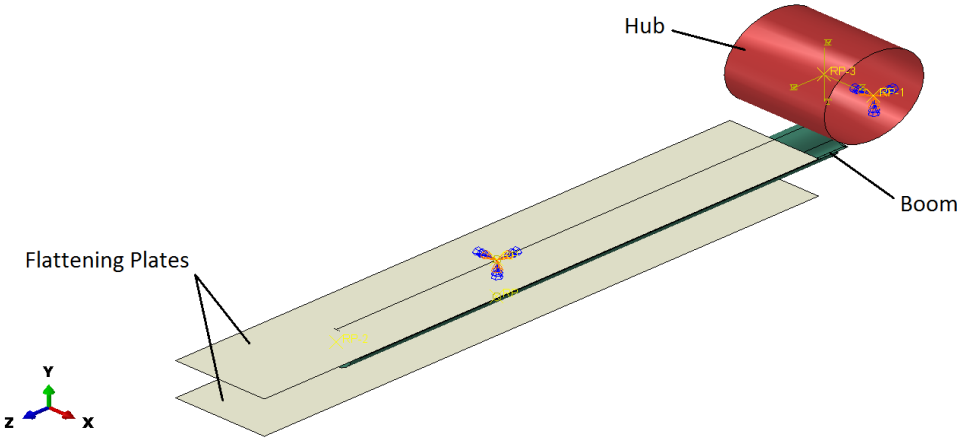

Figure 4.15. Model of the deployable boom structure in Abaqus CAE.

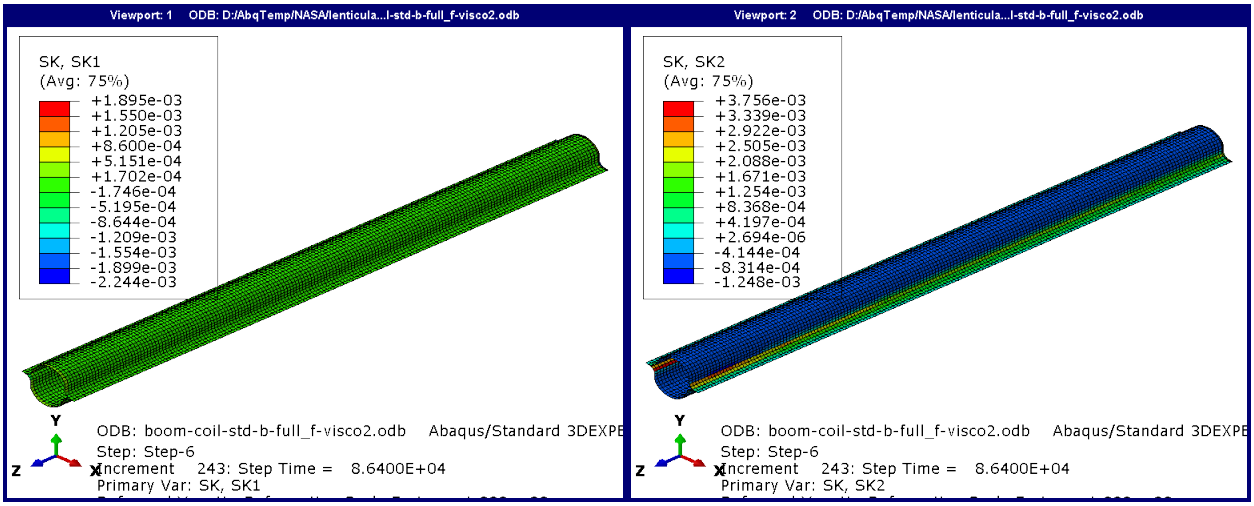

Figure 4.16. Contour plots of the residual curvatures after recovery.

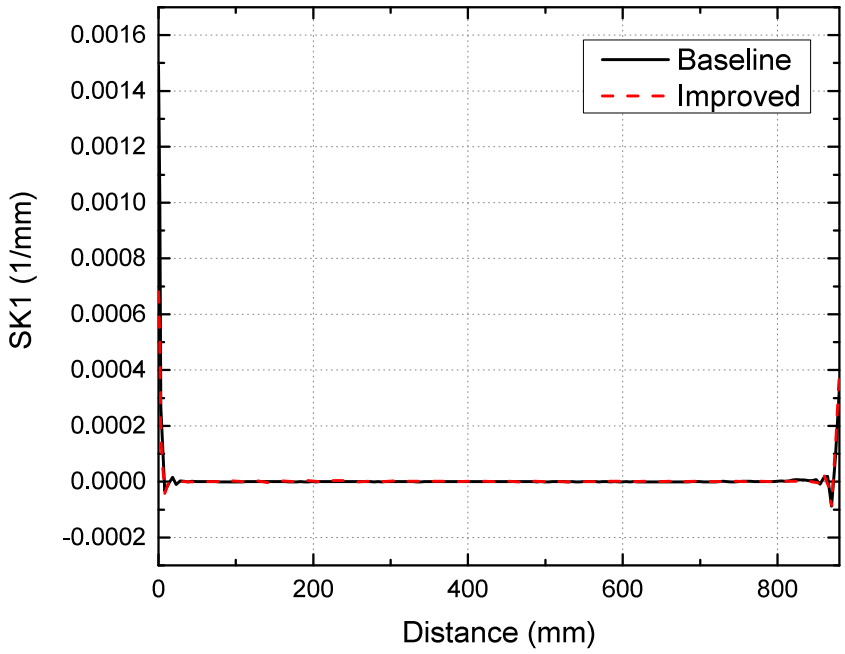

Figure 4.17. Residual curvature in the longitudinal direction along the symmetry line of the inner shell.

is reasonable to have negligible values outside the boundary regions. On the other hand, residual curvature in the hoop direction is much more pronounced. The opposite curvature signs of segments 1 and 2 are caused by their initial curvatures. After 24 hours of recovery, the maximum residual curvature was reduced by 88.3%.

Table 4.9. Forces applied to the radial hub rollers.

Roller	1	2	3	4	5	6	7
Force (N)	20	21	11	11	6	6	21

In the simplified baseline model, the tension force and flattening plates are present during the stowage and deployment process. Although this is partly justified by the step times, this setup is far from reality. It should still be noticed that (1) the existence of an axial tension force and flattening plates may affect the structural behavior during deployment, and (2) the effect of an axial tension force during stowage may not be negligible. Consequently, the

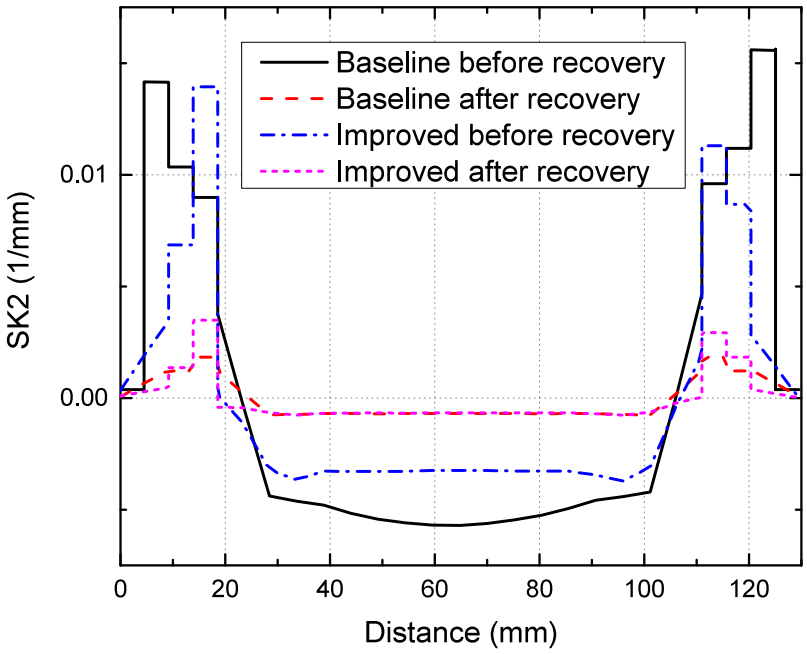

Figure 4.18. Residual curvature in hoop direction vs. hoop position at the midspan of the inner shell.

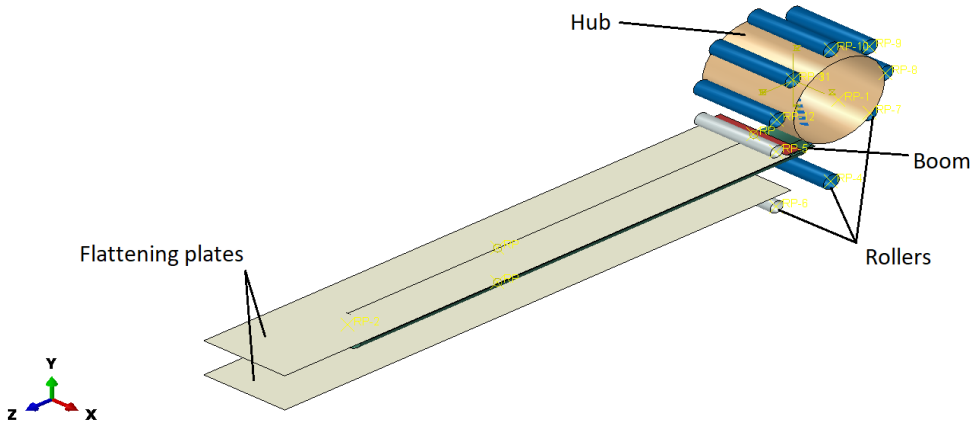

Figure 4.19. Improved model of the deployable boom structure in Abaqus/CAE.

baseline model was improved to remove the tension force and flattening plates after coiling. The improved model has cylindrical rollers to hold the boom in the stowed configuration, as shown in Figure 4.19. There are two kinds of rollers in the model, 7 surrounding the

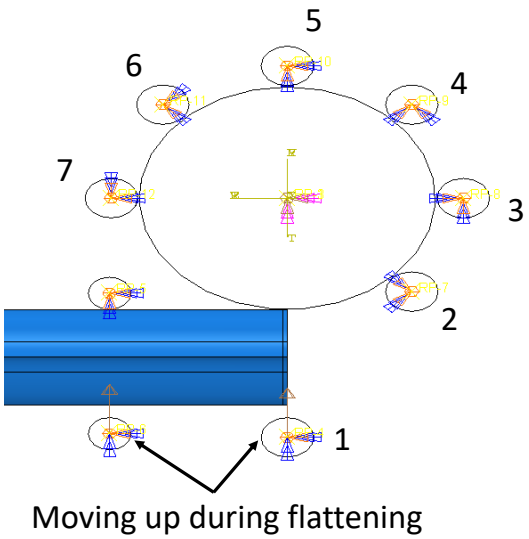

Figure 4.20. Numbering of the radial hub rollers.

hub radially (blue in Figure 4.19) and a pair below and above the boom, called nip rollers (gray in Figure 4.19). Numbering of the 7 radial hub rollers are shown in Figure 4.20, and the forces applied on each roller are shown in Table 4.9, with the magnitudes artificially increased from the design values to numerically improve stability.

In addition, all radial rollers have linear springs with a stiffness of 1 N/mm to provided larger compressive force if the boom tends to pop out from the hub during deployment. The nip rollers serve the purpose of controlling the deployment direction, which was initially done by the flattening plates in the baseline model. The nip rollers are fixed 13 mm apart for controlling the direction and preventing the boom from oscillating during deployment.

With the same stowage and recovery time as the baseline model, similar residual curvature distributions in the longitudinal and hoop directions are observed. The plot of curvature $SK1$ along the symmetry line of the inner shell is shown in Figure 4.17 and referred to as the improved model. Likewise, the plot of curvature $SK2$ along the hoop line at the midspan of the inner shell is shown in Figure 4.18. The residual curvature in the longitudinal direction is still negligible, while there is significant deformation in the hoop direction. The 24-hour recovery step reduces the residual curvature to 25% of the original value. The complexity of

the boom coiling simulation around a hub makes a quantitative comparison between the two models challenging. One reason for the differences between the two models in Figure 4.18 is caused by the rollers, as the boom tends to pop out from the hub during deployment, which is an interesting dynamic phenomenon that requires further investigation.

4.4 Summary

Starting with an introduction of linear viscoelasticity, this chapter presents the finite element simulation of CBT, and the coiling and deployment of a hub and TP-HSC boom deployable structure. Linear viscoelastic material properties are considered in both simulations. The effective shell properties obtained from the MSG-based shell theory are expressed in terms of Prony series and implemented in Abaqus UGENS. During the simulation of CBT, point-wise distributions of deformation and stress field are captured. With data reduction, direct comparisons with experimental results are made possible. Both QE and DI methods are compared and moment relaxation is accurately captured, while only DI method captures the residual deformation. However, there are deviations in the particular values obtained from simulation and experiments, possibly caused by boundary condition and viscoplasticity. For the simulation of boom and hub deployable structure, several simplifications were introduced to avoid convergence difficulties. Numerical studies were carried out with two models. Results from both models show residual curvature is negligible in the longitudinal direction, but significant in the hoop direction. As the material model is viscoelastic, residual deformation can be greatly reduces by a 24-hour recovery.

5. MSG-BASED NONLINEAR SHELL ANALYSIS

5.1 Nonlinear Shell Analysis with SwiftComp

As mentioned in Chapter 2, SwiftComp is an MSG-based general purpose homogenization tool. However, current version SwiftComp is limited to linear analysis. When doing a linear structure analysis with SwiftComp, effective properties of the structure, the ABD matrices for the classical shell model, can be obtained through a homogenization process. In some cases the homogenization will be carried out in multiple steps. For example, in unidirectional/plain weave composites a 3D solid homogenization for the matrix and fiber is carried out first to obtain the effective lamina/yarn properties, then the shell homogenization with the laminae/yarn and matrix to obtain the effective shell properties. The effective properties will be used as the sectional stiffness of the elements in a structural level finite element simulation. Results of the structural simulation can be used in SwiftComp to carry out dehomogenization to obtain the local distribution of strains and stresses inside the SG. However, in nonlinear analysis, effective properties of the structure is dependent on the loading state. In this case, the homogenization need to be integrated with the macroscopic analysis, such as the global structural analysis, and the effective properties need to be updated every iteration based on the dehomogenized state variables from the macroscopic analysis. For performing MSG-based nonlinear shell analyses, a nonlinear version of SwiftComp is developed based on the algorithm in Section 2.4. The flowchart of the nonlinear SwiftComp is shown in Figure 5.1. For handling shell structures with laminate or woven composites, the nonlinear SwiftComp is capable of performing both 3D homogenization and shell homogenization.

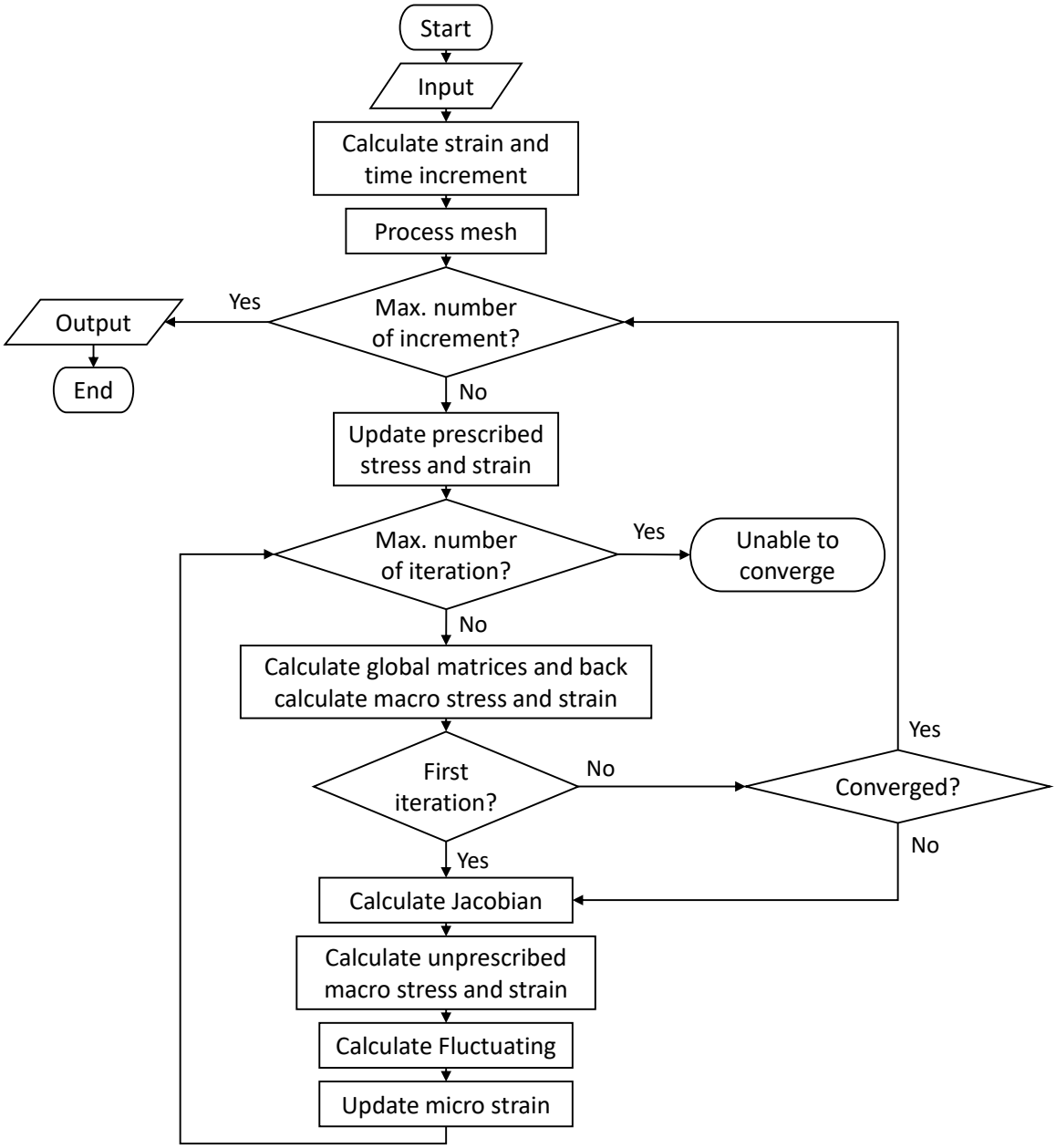

Figure 5.1. Flowchart of the nonlinear SwiftComp.

For carrying out nonlinear homogenizations, maximum strains need to be provided in the SwiftComp input file. A logical array with 6 components *indx_ss* is created to indicate which term in the macro strain is prescribed. In order to handle time dependent material behavior, maximum time, number of increments, and number of load steps also need to be provided as inputs. Based on the terms of *indx_ss*, a steering matrix *g_ss* is generated. Following [104], the macro stress and strain can be partitioned as

$$\bar{\sigma} = \begin{Bmatrix} \bar{\sigma}_u \\ \bar{\sigma}_k \end{Bmatrix}, \qquad \bar{\epsilon} = \begin{Bmatrix} \bar{\epsilon}_k \\ \bar{\epsilon}_u \end{Bmatrix} \tag{5.1}$$

where subscript k indicates prescribed components in the strain and stress, and u indicates the unprescribed components. Increment of the prescribed strain components is calculated with

$$\Delta\bar{\epsilon} = \bar{\epsilon}_{max}/N_{inc} \tag{5.2}$$

where $\bar{\epsilon}_{max}$ is the maximum strain, N_{inc} is the number of increments. Time increment is calculated with

$$\Delta t = t_{max}/(N_{maxinc} - N_{ldstp} - 1) \tag{5.3}$$

where $N_{maxinc} = N_{ldstp} \times N_{inc} + N_{ldstp} + 1$, and N_{ldstp} is the number of load steps. An array *atime* is defined following the same way as Abaqus, with *atime(1)* being the step time at the beginning of the current increment, and *atime(2)* being the total time at the beginning of the current increment.

The prescribed strain is updated at the start of every increment. Then, components of $\bar{\epsilon}_k$ and $\bar{\sigma}_k$ are rearranged to be the same as Eq. (5.1) using *g_ss*. A new array can be formed as

$$\bar{\epsilon}^* = \begin{Bmatrix} \bar{\epsilon}_k \\ \bar{\sigma}_k \end{Bmatrix} \tag{5.4}$$

After that, global matrices of $D_{\epsilon\epsilon}$, $D_{h\epsilon}$, $S_h = \Psi = \left\langle (\Gamma_h S)^{\mathrm{T}} \sigma \right\rangle$, E_ϵ, and S_ϵ are calculated by looping through every elements and integration points in the SG. Here

$$E_\epsilon = \langle \Gamma \rangle, \; S_\epsilon = \langle \sigma \rangle \tag{5.5}$$

for 3D models and

$$E_\epsilon = \left\langle \Gamma_\epsilon^{\mathrm{T}} \Gamma \right\rangle, \; S_\epsilon = \left\langle \Gamma_\epsilon^{\mathrm{T}} \sigma \right\rangle \tag{5.6}$$

for shell models. At each integration point, micro stress and strain, and state variables are initialized if this is the first increment. If it is not, their values are read from arrays storing the data from the previous iteration. After the global matrices are assembled, macro stress and strain are back-calculated using the global matrices and Ω. In the case of 3D models,

$$\tilde{\epsilon} = \frac{1}{\Omega} E_\epsilon, \qquad \tilde{\sigma} = \frac{1}{\Omega} S_\epsilon \tag{5.7}$$

and in shell models,

$$\begin{aligned} \tilde{\epsilon} = \epsilon &= \begin{bmatrix} \varepsilon_{11} & \varepsilon_{22} & 2\varepsilon_{12} & \kappa_{11} & \kappa_{22} & \kappa_{12} + \kappa_{21} \end{bmatrix}^{\mathrm{T}} \\ \tilde{\sigma} = N &= \frac{1}{\Omega} S_\epsilon \end{aligned} \tag{5.8}$$

where

$$\begin{aligned} \varepsilon_{11} &= \frac{1}{\Omega} \frac{6E_{\epsilon(4)} \left(h^+ + h^-\right) - 4E_{\epsilon(1)} \left(h^{+2} + h^{-2} + h^+ h^-\right)}{h^3} \\ \varepsilon_{22} &= \frac{1}{\Omega} \frac{6E_{\epsilon(5)} \left(h^+ + h^-\right) - 4E_{\epsilon(2)} \left(h^{+2} + h^{-2} + h^+ h^-\right)}{h^3} \\ 2\varepsilon_{12} &= \frac{1}{\Omega} \frac{6E_{\epsilon(6)} \left(h^+ + h^-\right) - 4E_{\epsilon(3)} \left(h^{+2} + h^{-2} + h^+ h^-\right)}{h^3} \\ \kappa_{11} &= \frac{1}{\Omega} \frac{6E_{\epsilon(1)} \left(h^+ + h^-\right) - 12E_{\epsilon(4)}}{h^3} \\ \kappa_{22} &= \frac{1}{\Omega} \frac{6E_{\epsilon(2)} \left(h^+ + h^-\right) - 12E_{\epsilon(5)}}{h^3} \\ \kappa_{12} + \kappa_{21} &= \frac{1}{\Omega} \frac{6E_{\epsilon(3)} \left(h^+ + h^-\right) - 12E_{\epsilon(6)}}{h^3} \end{aligned} \tag{5.9}$$

and h is the thickness of the plate/shell, h^+ and h^- are the thickness coordinates of the top and bottom surfaces respectively. Tilde instead of bar is used to distinguish the back-calculated macro stress and strain from the maco stress and strain at the start of the increment. $\tilde{\epsilon}$ and $\tilde{\sigma}$ are also rearranged using *g_ss*, resulting in a new array $\tilde{\epsilon}^*$. Difference between $\bar{\epsilon}^*$ and $\tilde{\epsilon}^*$ is calculated as

$$\mathrm{d}\bar{\epsilon} = \bar{\epsilon}^* - \tilde{\epsilon}^* \tag{5.10}$$

If the current iteration is not the first iteration, it will perform the convergence check. If $\mathrm{d}\bar{\epsilon}$ is close to zero, the iteration is judged converged and the current increment is finished. Micro stress and strain, and state variables are stored for use in the next increment. Macro stress and strain are stored for output.

If the current iteration is the first iteration or not converged, it will calculate a Jacobian. If this is the first iteration, the Jacobian will be the tangent stiffness, calculated by calculating the $\hat{V}_0$ in Eq. (2.73) and using Eq. (2.76). If this is not the first iteration, the Jacobian is calculated using Eq. (2.90). To calculate the unprescribed components in the macro strain and stress, the Jacobian needs to be partitioned and rearranged using *g_ss*, gives

$$A = \begin{bmatrix} A_{uk} & A_{uu} \\ A_{kk} & A_{ku} \end{bmatrix} \tag{5.11}$$

$$A^* = \begin{bmatrix} A_{uk} - A_{uu}A_{ku}^{-1}A_{kk} & A_{uu}A_{ku}^{-1} \\ -A_{ku}^{-1}A_{kk} & A_{ku}^{-1} \end{bmatrix} \tag{5.12}$$

Then, $\bar{\sigma}^*$ can be calculated as

$$\mathrm{d}\bar{\sigma}^* = \begin{Bmatrix} \mathrm{d}\bar{\sigma}_u \\ \mathrm{d}\bar{\epsilon}_u \end{Bmatrix} = A^* \mathrm{d}\bar{\epsilon}^* \tag{5.13}$$

If this is the first iteration, $\mathrm{d}\bar{\epsilon}^*$ represent the increment of the prescribed values. If this is not the first iteration, it represents the residual between the current iteration and the prescribed

values. Macro strain $\bar{\epsilon}$ is updated using $\mathrm{d}\bar{\epsilon}^*$ and $\mathrm{d}\bar{\sigma}^*$. If this is the first iteration, fluctuating function is solved by

$$EV = -S_h - D_{h\epsilon}\bar{\epsilon} \tag{5.14}$$

S_h is presented to prevent the accumulation of numerical error from previous increment. If this is not the first iteration, correction of the fluctuating function is solved based on Eq. (2.84) as

$$E\mathrm{d}V = -S_h \tag{5.15}$$

Notice that in Eq. (5.14) and (5.15), V and $\mathrm{d}V$ are solved instead of $\hat{V}_0$ in Eq. (2.73) or $\mathrm{d}\hat{V}_0$. The fluctuating function/correction solved in Eq. (5.14) and (5.15) is used for updating the micro strain, which will be used in the next iteration, and this completes the current iteration. The next iteration will be executed at least until the convergence check.

The nonlinear SwiftComp has the potential to be linked with global structural analysis, such as analyzing the nonlinear behavior of TP-HSC in deployable structures. In Abaqus, this can be done through the user subroutine UGENS, with the UGENS working as an interface to call and pass data to the nonlinear SwiftComp, and receive the output from the nonlinear SwiftComp. Figure 5.2 shows the procedure of a two-step nonlinear homogenization. At

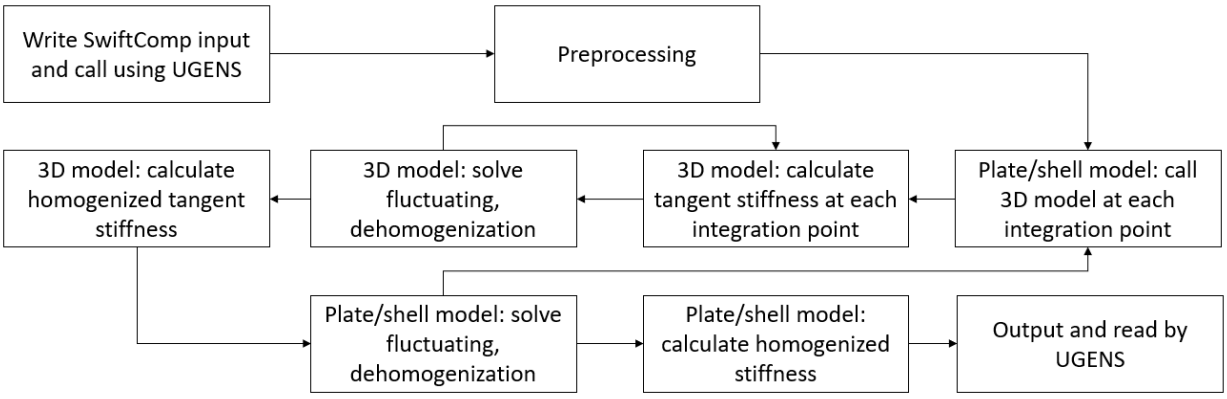

Figure 5.2. Procedure of nonlinear homogenization for TP-HSC with SwiftComp.

every integration point in the structural simulation, the UGENS will be called at the start of every iteration. The UGESN will generate SwiftComp input files, and write the stress and strain to the input file. The nonlinear SwiftComp will read the input and preprocess,

and start the shell level homogenization. At each integration point of the shell SG, the process of 3D solid homogenization will be called. In this step of homogenization, the tangent stiffness of the lamina or yarn will be calculated based on the nonlinear material model. This process is done by iterations and loops until the homogenization converges. The resultant 3D tangent stiffness will be used for shell level homogenization, and similarly, the shell level homogenization is also done by iterations. If the current iteration is not converged, it will go back to the 3D homogenization step and re-calculate the tangent stiffness based on the updated stress and strain at the integration point of the shell SG. Once the shell homogenization is converged, tangent ABD stiffness will be output and read by UGENS for the structural level analysis.

5.2 User Material for SwiftComp

To perform nonlinear shell analysis, in addition to a nonlinear homogenization solver, nonlinear material constitutive models are also necessary. For the easiness of implementing various nonlinear material models, the user material capability of nonlinear SwiftComp is developed. This capability allows implementing a nonlinear material into a separated subroutine without changing the other part of the SwiftComp code. For the convenience of the user, the user material for SwiftComp, called SCUMAT, is developed to be similar with the Abaqus UMAT user subroutine. Format of the SCUMAT is:

```
      module UserMaterial
      contains
c
      SUBROUTINE SCUMAT(stress,statev,ddsdde,
     1 stran,dstran,time,dtime,
     2 ndi,nshr,ntens,nstatv,props,nprops,
     3 noel,npt,kstep,kinc,cmtype)
c
      integer ndi,nshr,ntens,nstatv,nprops,
     1 noel,npt,kstep,kinc,cmtype
```

```
      double precision stress(ntens),statev(nstatv),
     1 ddsdde(ntens,ntens),stran(ntens),dstran(ntens),
     2 time(2),dtime,props(nprops)
c
c Code for defining the user material
c
      return
      end
      end module UserMaterial
```

In SCUMAT, the variables to be defined by the user are *stress*, the stress at the end of the increment, *statev*, the solution dependent variables (SDV), and *ddsdde*, Jacobian matrix of the material model. Other variables that are passed to SCUMAT and can be used for defining the *stress*, *statev*, and *ddsdde* are: *stran*—strain at the start of the increment, *dstran*—strain increment, *time(1)*—time of the loading step at the start of the increment, *time(2)*—time of the whole analysis at the start of the increment, *dtime*—time increment, *ndi*—number of normal components of the stress and strain, *nshr*—number of shear components of the stress and strain, *ntens*—number of all components of the stress and strain, *nstatv*—number of SDV, *props*—an array with user defined material properties, *nprops*—the number of user defined material properties, *noel*—the element number, *npt*—the integration point number, *kstep*—the step number, *kinc*—the increment number, and *cmtype*—the material type number. It needs to be specified in the SwiftComp input file if user material will be used. This is done by defining the isotropy indicator *isotropy* to be 9, and then when defining the material properties, it should have the form:

```
material_number    isotropy    ntemp
2-step_flag
number_of_material_properties    number_of_SDV
temperature    density
(List of material properties)
```

The *2-step_flag* indicates that this analysis is a 2-step homogenization which will call another nonlinear SwiftComp run if it is 1. The required values are the number of user defined material properties, the number of SDV, and a list of user defined material properties. These values are the same as defining a user material in Abaqus. The format of SCUMAT and inputs needed for the user material provided the best possibility and minimum effort of converting an Abaqus UMAT into an SCUMAT for SwiftComp.

To validate the user material as well as the nonlinear material capability of the nonlinear SwiftComp, numerical studies are used to compare with Abaqus. To this end, a plate test sample was created in Abaqus, with the geometry and boundary conditions shown in Figure 5.3. It has only one material and the thickness is 1 mm. By applying a displacement

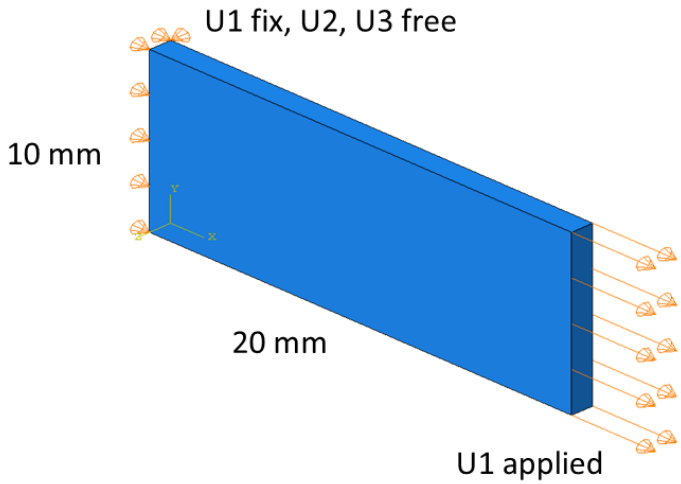

Figure 5.3. Plate test sample in Abaqus.

U_1, a normal strain of ϵ_{11} can be generated at the center of the plate, with other strain terms being free to vary. This results in a stress σ_{11} and other stress terms being zero. The comparison with nonlinear SwiftComp shell model can be done by analyzing the stress and strain through the thickness at the center of the plate and obtain the shell strain and curvature ϵ and κ, and the sectional force and moment N and M. The SCUMAT used in the nonlinear SwiftComp is converted from the Abaqus UMAT.

The first nonlinear material model is a simple viscoelastic model from Abaqus UMAT documentation [122]. Diagram of the model is shown in Figure 5.4. Stress-strain relation of

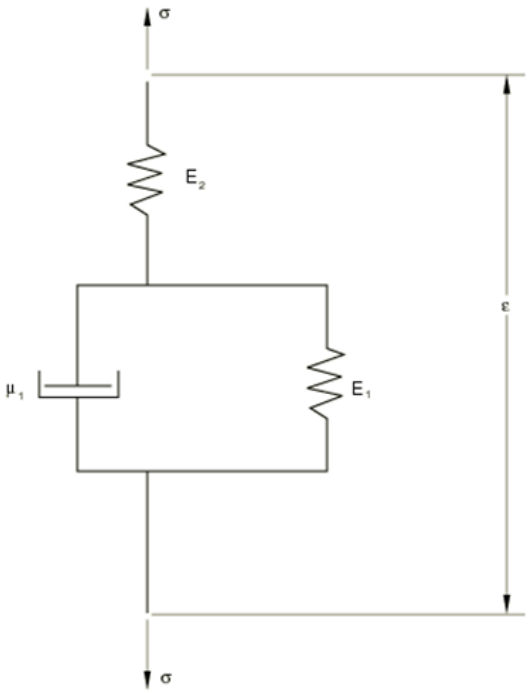

Figure 5.4. Diagram of the simple viscoelastic model [122].

the model can be generalized as an isotropic solid [122]

$$\sigma_{11} + \bar{\nu}\dot{\sigma}_{11} = \lambda\epsilon_V + 2\mu\epsilon_{11} + \bar{\lambda}\dot{\epsilon}_V + 2\tilde{\mu}\dot{\epsilon}_{11} \tag{5.16}$$

$$\sigma_{12} + \bar{\nu}\dot{\sigma}_{12} = \mu\epsilon_{12} + \tilde{\mu}\dot{\epsilon}_{12} \tag{5.17}$$

The model has 5 user defined material properties, as shown in Table 5.1, along with the values used in the analysis. The displacement U_1 is applied to be 0.2 mm, generating a

Table 5.1. User defined properties of the simple viscoelastic material.

λ	μ	$\bar{\lambda}$	$\tilde{\mu}$	$\bar{\nu}$
693	195	22587	6496	56

strain of 1%. Since this is a viscoelastic material model, 2 loading rates are used, with the loading process finished in 1 s or 100 s. Results are shown in Figure 5.5. It can be seen the no

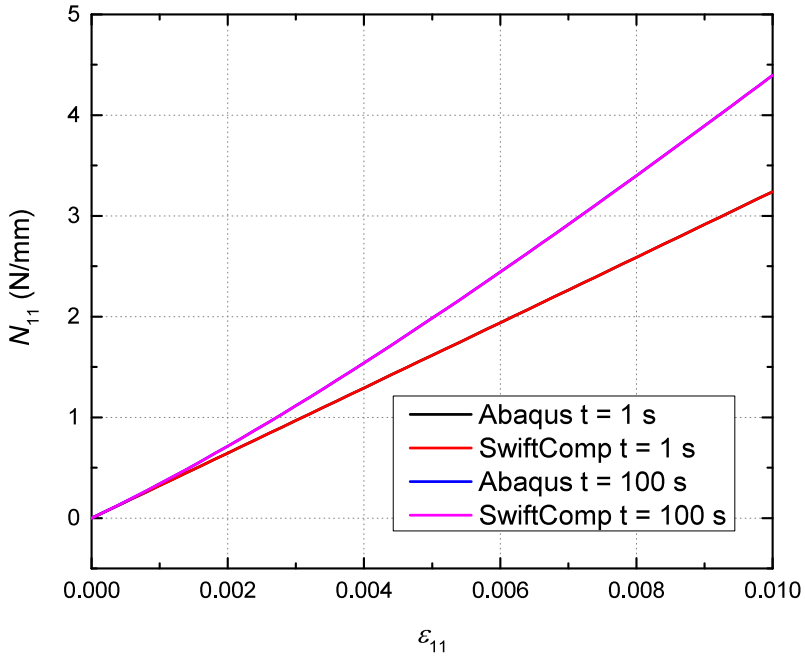

Figure 5.5. Loading curve of the simple viscoelastic model.

matter the loading rate, the curves from nonlinear SwiftComp overlap with the curves from Abaqus, showing the effectiveness of running with time-dependent nonlinear user material.

The second example is a continuum damage model, developed by Zhang and Yu [123]. This model is originally developed based on an explicit algorithm, so it is not rigorous to apply it in the implicit nonlinear SwiftComp, but it can still serve for the testing purpose. In this model, the update of the stress is given in a rate form:

$$\dot{\boldsymbol{\sigma}} = \left\{ [-(\boldsymbol{\mathcal{F}} : \boldsymbol{\epsilon}) : \boldsymbol{\mathcal{E}} + \boldsymbol{\mathcal{G}} : \boldsymbol{\epsilon}] : \tilde{\mathcal{N}}^{-1} + \mathcal{C}^{\mathrm{e}} \right\} : \dot{\boldsymbol{\epsilon}} \tag{5.18}$$

where $\mathcal{C}^{\mathrm{e}}$ is the elastic stiffness tensor before any damage; $\boldsymbol{\mathcal{E}}$ and $\tilde{\mathcal{N}}$ are fourth-order coefficient tensors; $\boldsymbol{\mathcal{F}}$ and $\boldsymbol{\mathcal{G}}$ are sixth-order coefficient tensors. When implemented as an SCUMAT, this rate form is used as incremental form, and strain rate and strain at the start of the current iteration, $\boldsymbol{\epsilon}$, are known. All the coefficient tensors can be calculated based on elastic stiffness, strain state, and other damage related parameters. Details of the model can be

found in [123]. This model has 12 user defined material constants and 9 SDV, as shown in Tables 5.2 and 5.3. In this example the displacement applied is 0.024 mm, generating

Table 5.2. User defined properties of the damage model.

Material Properties (12)	Value
Isotropic elatic modulus	38500
Isotropic Poisson's ratio	0.24
Damage threshold	1.6e-5
Damage model parameter 1	0.5
Damage model parameter 2	0.5
Damage surface shape parameter	1
Damage anisotropy vector	(1, 1, 1, 1, 1, 1)

Table 5.3. SDV of the damage model.

SDV (9)
Current damage threshold
Current damage accumulation variable
Damage variable, 6 components
Element delete flag

a normal strain of 0.12%. The strain is not further increased because originally the model is developed for explicit analysis and implemented as a VUMAT, and a direct conversion to UMAT makes the model not stable in implicit analysis. Increase the strain will lead to convergence issue in both Abaqus and nonlinear SwiftComp. Loading curve of the model is shown in Figure 5.6. It can be seen from Figure 5.6 that nonlinear SwiftComp have an excellent match with Abaqus results. These two examples validate that the user material capability of nonlinear SwiftComp can be used in the same way as Abaqus UMAT and generates reliable results.

As mentioned in Section 5.1, for some structures such as laminates or woven composites shells, a 2-step homogenization consists of a 3D solid step and a shell homogenization step is necessary. The 2-step homogenization shown in Figure 5.2 is tested with the nonlinear SwiftComp. The SG used in the 3D solid step is shown in Figure 5.7, a hexagonal pack consists of fiber and matrix, representing the lamina. The matrix uses the viscoelastic model from Abaqus in the previous example, and the fiber is elastic, with the material properties

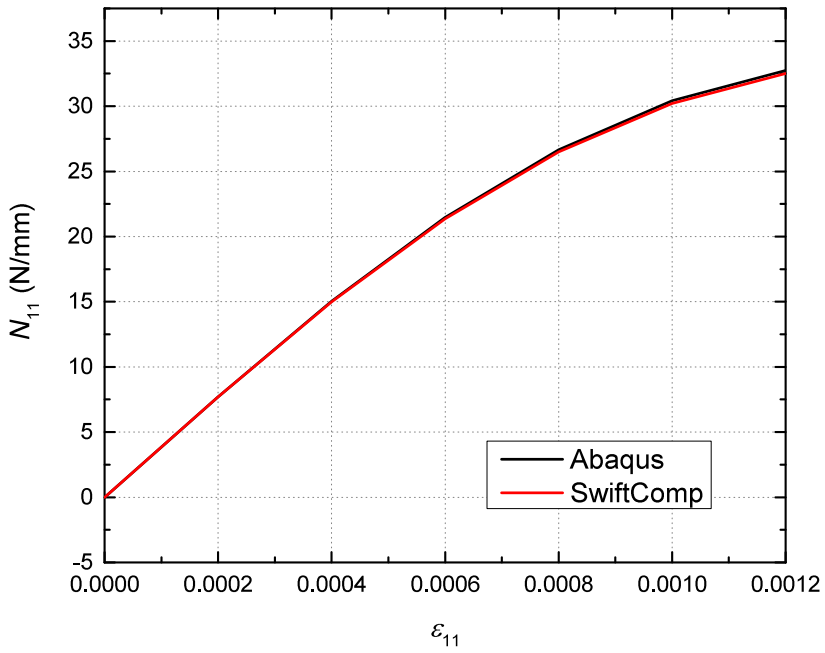

Figure 5.6. Loading curve of the damage model.

shown in Table 5.4. The shell model uses a 1D SG, with 1 element representing a one-layered shell. Thickness of the shell is 1 mm. In order to better observe the behavior caused by the material model of the matrix, a bending in the matrix direction is applied. A curvature of 0.02 1/mm is applied with two curvature rates, resulting in loading time of 1 s and 100 s respectively. Moment-curvature curve are shown in Figure 5.8. It can be seen that with a slower loading speed, the shell generates more moment, and the curve is more nonlinear. As expected, the behavior of the matrix material in the 3D solid step is reflected in the behavior of the shell model. However, the 2-step homogenization has the drawback of being computational expensive. Both loading cases take about 6 hours to finish, and the cost will be greatly increased if the shell model uses a more complex SG such as a 3D SG representing woven composites. This makes applying the method to structural analysis impractical. A possible solution to this is to construct a surrogate model based on the results of the nonlinear homogenization. For example, a surrogate model can be constructed to represent

Figure 5.7. 2D SG of the fiber reinforced composite.

Table 5.4. Engineering constants of the fiber.

E_1 (MPa)	2.94×10^5
E_2 (MPa)	2.91×10^4
E_3 (MPa)	2.91×10^4
ν_{23}	0.20
ν_{13}	0.20
ν_{12}	0.46
G_{23} (MPa)	1.13×10^4
G_{13} (MPa)	1.13×10^4
G_{12} (MPa)	1.00×10^4

the behavior of the lamina, and then 2-step homogenization can be avoided by using the surrogate model in the shell homogenization step.

5.3 Nonlinear Viscoelastic-Viscoplastic Shell Analysis

In Chapter 4, the behavior of TP-HSC is discussed based on the linear viscoelastic constitutive model. However, some of the deviation between finite element simulation and experiments shows that permanent deformation exists when the TP-HSC specimens undergo large bending deformation. Since permanent deformation can greatly affect the behavior of deployable structures made with TP-HSC, shell analysis with nonlinear viscoelastic-viscoplastic constitutive material model is necessary. The constitutive material model suitable for this purpose was developed by Zhang [124]. The model consists of two parts: a nonlinear viscoelastic part that governs the resin behavior before yielding, and a viscoplastic part that

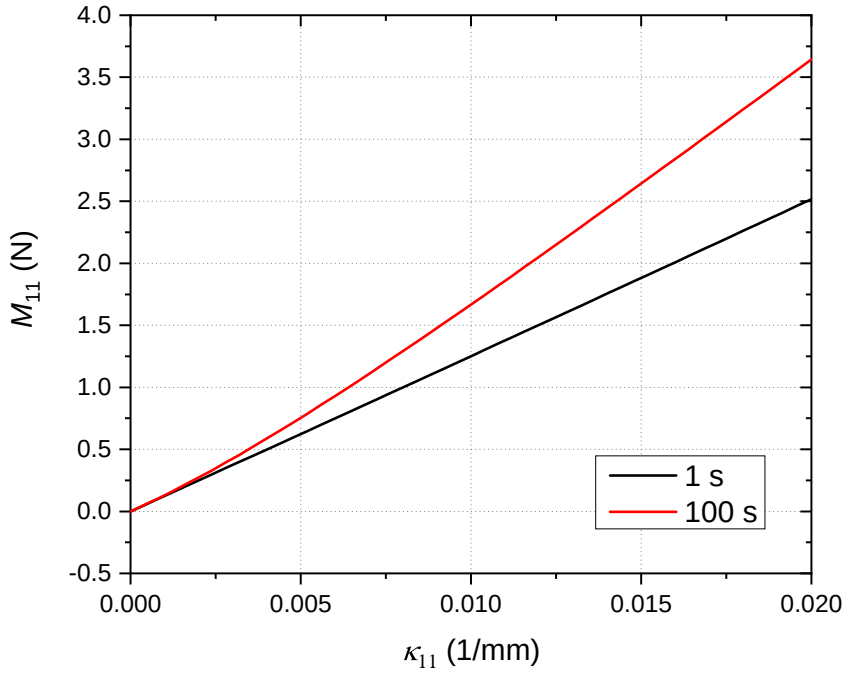

Figure 5.8. Moment-curvature curves of the 2-step homogenization.

calculates the permanent deformation. In the viscoelastic part, the tangent stiffness $\tilde{\mathcal{C}}$ and stress increment $\Delta\boldsymbol{\sigma}$ can be calculated with:

$$\tilde{\mathcal{C}}^{-1} = \tilde{J}\mathcal{I}' + \frac{1}{3}\tilde{B}\boldsymbol{I} \otimes \boldsymbol{I} \tag{5.19}$$

$$\Delta\boldsymbol{\sigma} = \tilde{\mathcal{C}} : \Delta\boldsymbol{\epsilon} + \sum_{i=1}^{N} \left[1 - \exp\left(-\lambda_i \Delta\psi\right)\right] \tilde{\mathcal{C}} : \left(\boldsymbol{\epsilon}_i\right)_n \tag{5.20}$$

where $\tilde{J}$ and $\tilde{B}$ are scalars calculated from the shear and the bulk compliance, along with stress-dependent functions and stress-dependent effective time ψ; $\mathcal{I}'$ is the deviatoric part of the fourth-order identity tensor; $\boldsymbol{I}$ is the second-order identity tensor; λ_i are the inverse of relaxation time; $\boldsymbol{\epsilon}_i$ are strain components decomposed based on the 1D generalized Maxwell

model. When the resin starts yielding, viscoplastic deformation happens. In this case, a radial return algorithm is used and the stress can be updated with:

$$\boldsymbol{\sigma} = \beta + \boldsymbol{\sigma} \tag{5.21}$$

And the tangent operator $\mathcal{C}^{alg}$ can be calculated with:

$$\mathcal{C}^{alg} = \left(\mathcal{I} + \frac{\partial \boldsymbol{X}}{\partial \beta} - \frac{\frac{\partial \boldsymbol{X}}{\partial \Delta v} \otimes \frac{\partial \mathrm{P}}{\partial \beta}}{\frac{\partial \mathrm{P}}{\partial \Delta v}} \right) : \left(\frac{\partial \boldsymbol{\Psi}}{\partial \beta} - \frac{\frac{\partial \boldsymbol{\Psi}}{\partial \Delta v} \otimes \frac{\partial \mathrm{P}}{\partial \beta}}{\frac{\partial \mathrm{P}}{\partial \Delta v}} \right)^{-1} : \tilde{\mathcal{C}} \tag{5.22}$$

where $\boldsymbol{X}$ is the back stress tenor due to kinematic hardening; β is a stress related tensor to be updated in the algorithm; v is a viscoplastic multiplier; $\mathrm{P} = \Delta v - \dot{v}\Delta t$; $\boldsymbol{\Psi}$ is another stress related tensor. Details of this constitutive model can be found in [124].

5.3.1 Numerical Examples

Firstly, the nonlinear viscoelastic part of the constitutive model introduced is implemented into an SCUMAT and tested with the nonlinear SwiftComp. An experiment done by Lai and Bakker [125] is used for comparison. The material model has 11 user-defined

Table 5.5. Prony series of the Material [125].

n	λ_n (s^{-1})	$D_n \times 10^{-6}$ (MPa^{-1})
1	1	23.6358
2	10^{-1}	5.6602
3	10^{-2}	14.8405
4	10^{-3}	18.8848
5	10^{-4}	28.5848
6	10^{-5}	40.0569
7	10^{-6}	60.4235
8	10^{-7}	79.6477
9	10^{-8}	162.1790
D_0		270.9000

material constants, 10 of them being the Prony series expressed in terms of compliance, as shown in Table 5.5, and the last one being the Poisson's ratio $\nu = 0.39$. In the mean time, in order to show the capability of the nonlinear SwiftComp on shell modeling, a shell model

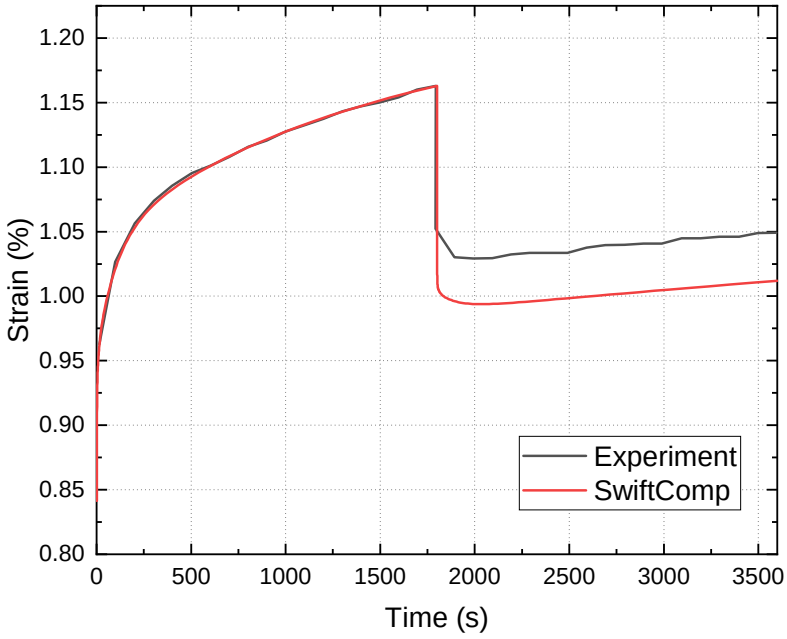

Figure 5.9. Strain history of a nonlinear viscoelastic shell under creep and recovery.

is used instead of a solid model. For a straightforward comparison, the thickness of the shell is 1 mm. In the analysis, the shell is loaded with tensile sectional force of 30 N/mm instantaneously, and kept for 1800 seconds for creep. After that, the load is reduced to 25 N/mm, and kept for another 1800 seconds for recovery. Results are shown in Figure 5.9. We can see that the strain has an excellent match during the creep, while underestimation exist during the recovery period, with an error of about 5%. Possible cause of underestimation can be explained by that plastic deformation already happened in the experiment while it is not included in the numerical model. Responses of the model under different load magnitudes are also compared. In the experiments [125], the specimens are loaded with 15, 20, 25, and 30 MPa respectively. Using the same 1 mm thick shell setting, prescribed section forces of 15, 20, 25 and 30 N/mm are applied in the nonlinear SwiftComp. After the creep time of 1800 seconds, the load is completely removed and followed with recovery of another 1800 seconds. Resultant strains during creep are shown in Figure 5.10 and during recovery in Figure 5.11.

In these two figures, different line types are used to represent different load magnitudes,

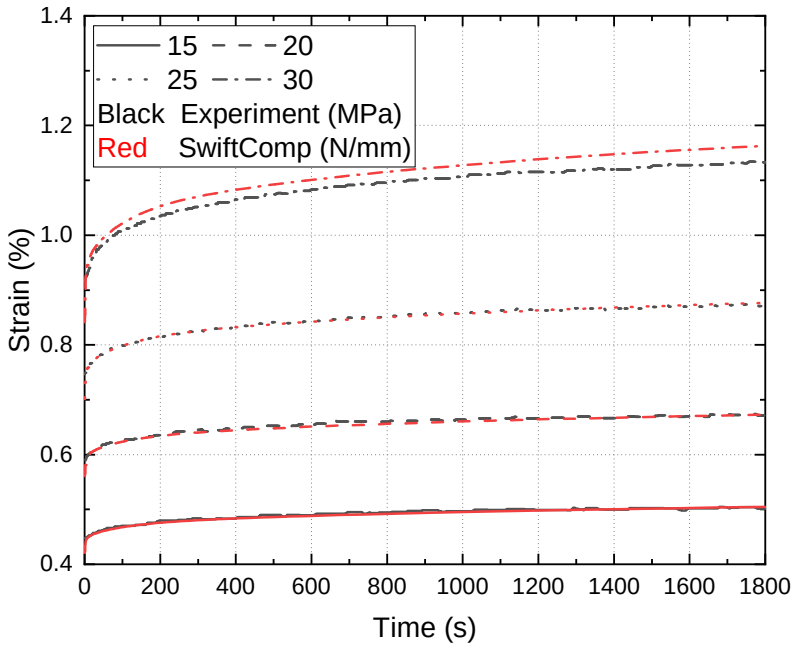

Figure 5.10. Strain history of a nonlinear viscoelastic shell under different load magnitude during creep.

with the unit of MPa for experimental results, plotted in black, or N/mm for the SwiftComp Results, plotted in red. Similar to the previous example, the nonlinear SwiftComp provides excellent matches for the creep and some deviation can be observed during the recovery. The deviation is greater with load with larger magnitudes.

Another example is studied with the constitutive model using a hexagonal pack as a 2D SG for 3D solid homogenization, as shown in Figure 5.7. The capability of 3D solid homogenization needs to be validated as it is necessary in the 2-step homogenization. The nonlinear viscoelastic material model is used for the resin matrix and the fiber is elastic, with the properties shown in Table 5.4. A tensile load is applied in the fiber direction: 1% of strain loaded incrementally over 180 seconds. Then the strain is kept for 1800 seconds for relaxation. Stress history of the whole loading process is shown in Figure 5.12. Due to the load being applied in the fiber direction, the curve looks bi-linear, and the stress magnitude is large compared with those with homogeneous material in previous examples. However,

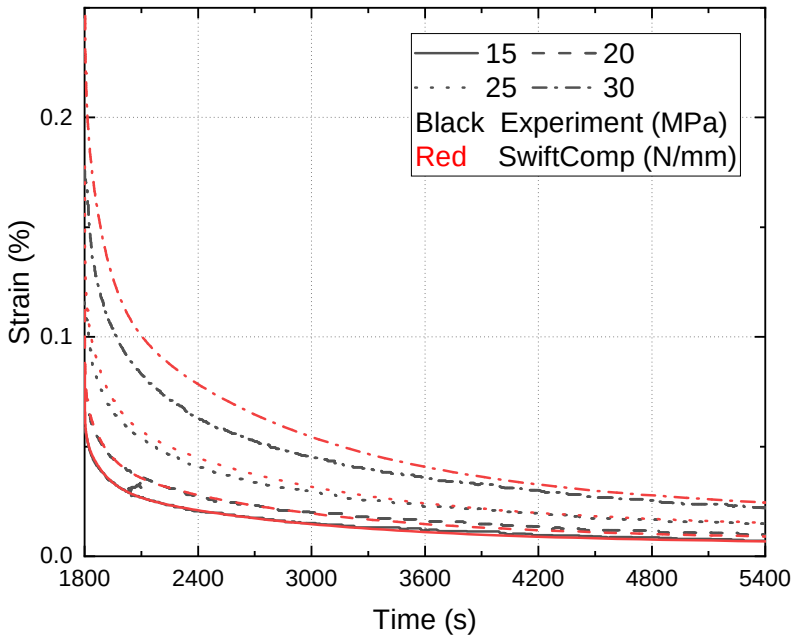

Figure 5.11. Strain history of a nonlinear viscoelastic shell under different load magnitude during recovery.

when focusing on the relaxation part, as shown in Figure 5.13, the stress relaxation can be observed. This shows the capability of the nonlinear SwiftComp and the SCUMAT for capturing the nonlinear viscoelastic behavior for both shell and 3D solid models.

To analyze the material behavior after yielding, the viscoplastic part of the constitutive model is also implemented into an SCUMAT. This model has totally 18 user-defined material constants. The viscoelastic part use the same Prony series and Poisson's ratio as the previous model, as shown in Table 5.5. Seven Viscoplasticity related material constants are shown in Table 5.6, where σ_y is the initial yield stress; Q and b are isotropic hardening parameters; C and a are kinematic hardening parameters; γ is a viscosity parameter; n is a rate-sensitivity parameter. The model is tested with a homogeneous shell model with a thickness of 0.2 mm. The loading path consists of four parts: loading, relaxation, unloading, and recovery. The shell is loaded with a curvature of 0.18 mm^{-1} through a 100-second time period. Two relaxation times are compared, 9000 seconds and 18000 seconds. Then the shell is unloaded

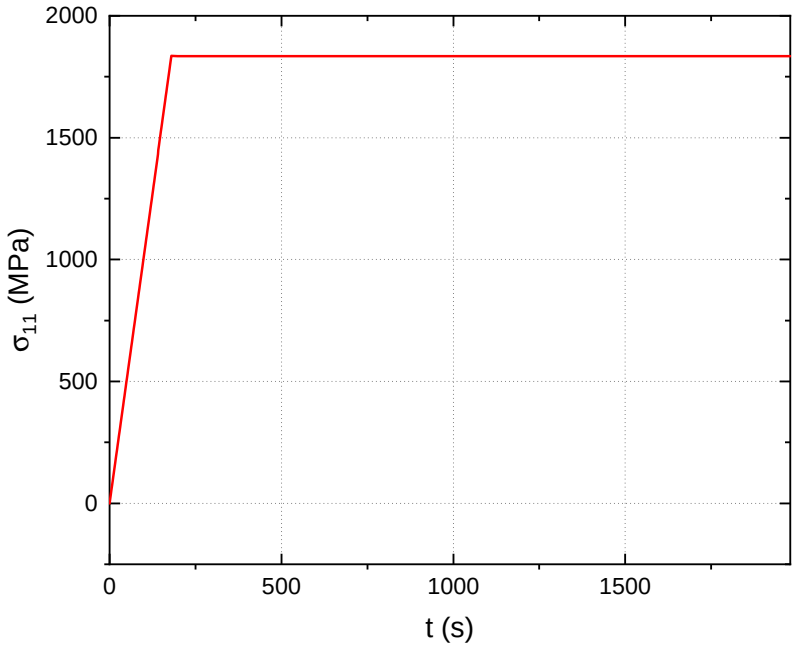

Figure 5.12. Stress history of the hexagonal pack.

Table 5.6. Viscoplastic material parameters.

Parameter	Value
σ_y (MPa)	35
Q (MPa)	5.50879
b	53.2535
C (MPa)	1035.167
a	140.2
γ (s^{-1})	1.00845 $\times 10^{-4}$
n	8.27066

to a moment-free state through 100 seconds, and followed by the recovery of 36000 seconds. Moment-curvature curve during the loading cycle is shown in Figure 5.14. During relaxation, the moment dropped while the curvature remains the same, and longer relaxation time results in larger total drop. Although the loading and unloading curves look linear, after recovery, residual curvature can be observed in both cases, as shown in Figure 5.15. At the end of the recovery. the residual curvature of the 18000-second relaxation time case is 32.6%

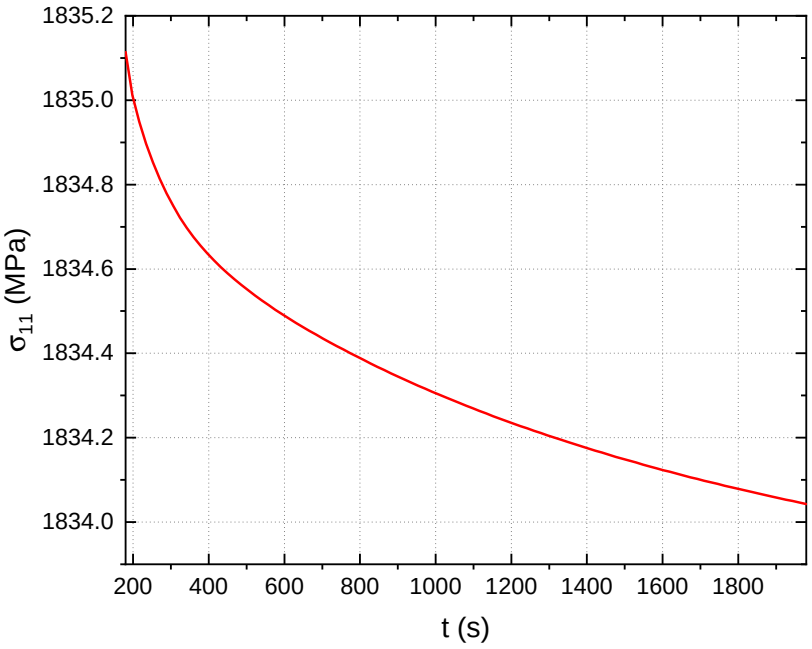

Figure 5.13. Stress history of the hexagonal pack during relaxation.

larger than the 9000-second case, even though their loaded curvatures are the same. This means that in both cases the material has yielded, and the plastic deformation happen to be accumulating during the relaxation, validating that the developed models can capture viscoplastic behavior.

5.3.2 Surrogate Model with Nonlinear SwiftComp

As mentioned in Section 5.2, due to the high computational cost of the 2-step homogenization. Surrogate models are necessary for nonlinear SwiftComp to be applied in the global structural simulation. In this preliminary study, the original behavior of the SG is fitted into a polynomial as the surrogate model. For simplicity, the 2D SG in Figure 5.7 is used, as well as the same viscoelastic resin and elastic fiber shown in Table 5.1 and Table 5.4.

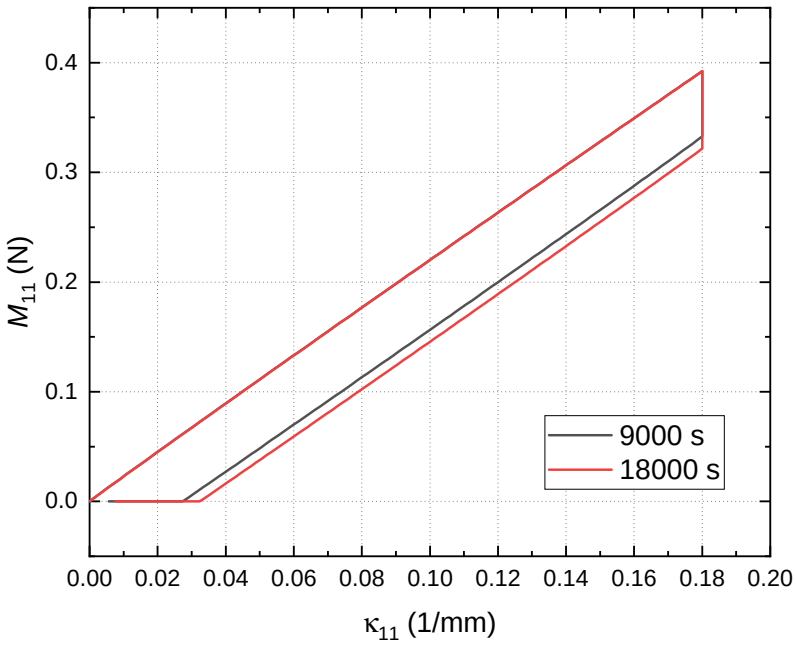

Figure 5.14. Moment-curvature curve of the viscoelastic-viscoplastic shell.

The polynomial surrogate model is generated using Dakota. It uses a quadratic function in the form of [120]:

$$f(\mathbf{x}) = c_0 + \sum_{i=1}^{n} c_i x_1 + \sum_{i=1}^{n} \sum_{j \geqslant i}^{n} c_{ij} x_i x_j \tag{5.23}$$

where $f(\mathbf{x})$ represents each response of the surrogate model; x_i are terms of the design parameters vector $\mathbf{x}$; n is the dimension of $\mathbf{x}$; c_0, c_i and c_{ij} are the coefficients of the polynomial to be fitted by data. Due to the material properties and the geometry of the SG, there is no coupling between normal and shear behavior. As a result, when investigating the normal behavior of the SG, the design parameters only need to include the normal terms of the macro strains ϵ_{11}, ϵ_{22} and ϵ_{33}. The model consists of 24 responses, representing 3 normal terms of the macro stresses and 21 terms in the 3D effective stiffness matrix. The coefficients of the polynomials are determined based on the sample data provided to Dakota. In this study, the sample data are generated through nonlinear 3D homogenization of the SG, and

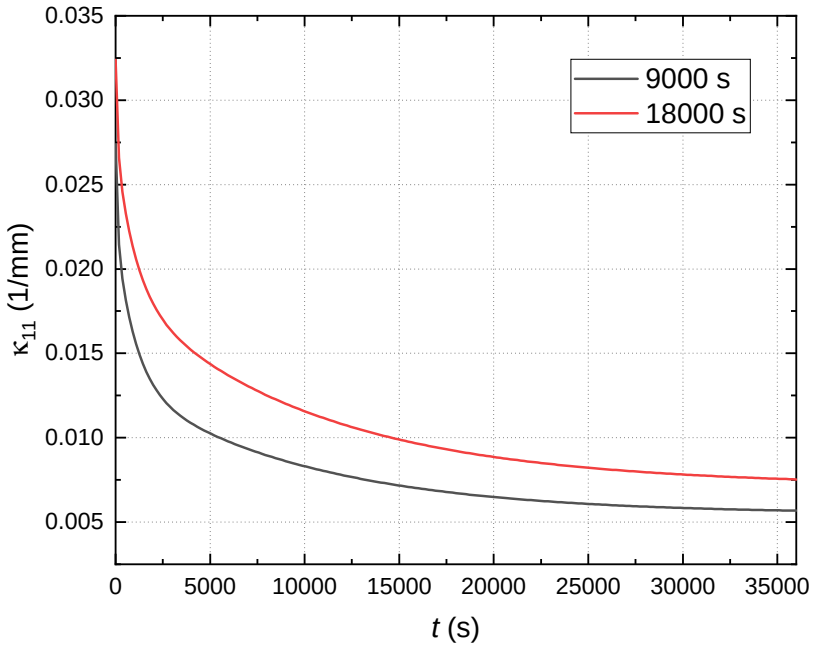

Figure 5.15. Residual curvature of the viscoelastic-viscoplastic shell during recovery.

since this is a preliminary study, separated surrogate models are constructed for different loading cases and these surrogate models are not for general purposes.

The surrogate model constructed for 3D homogenization of the 2D SG is implemented in another SCUMAT as if it is a homogenized material, and this SCUMAT substitutes the 3D solid homogenization step in the 2-step homogenization described previously. In the following example, a tensile strain of 1% is applied on a single-layer shell model, represented by a 1D SG, in 90 degree. To generate the sample data for surrogate modeling, the 2D SG is applied with a tensile strain of 1.5% in the matrix direction. A larger strain is used in the surrogate modeling for the purpose of avoiding extrapolation of the data. Shell analysis with the surrogate model is compared with the 2-step homogenization with the same setting, and results are shown in Figure 5.16. It can be seen that the surrogate model match closely to the 2-step homogenization. Overestimation exist when the strain goes higher, with an maximum error of 4.3%. Compared to the computational time of approximately 6 hours for the 2-step homogenization, the computational cost of the analysis with surrogate models is determined

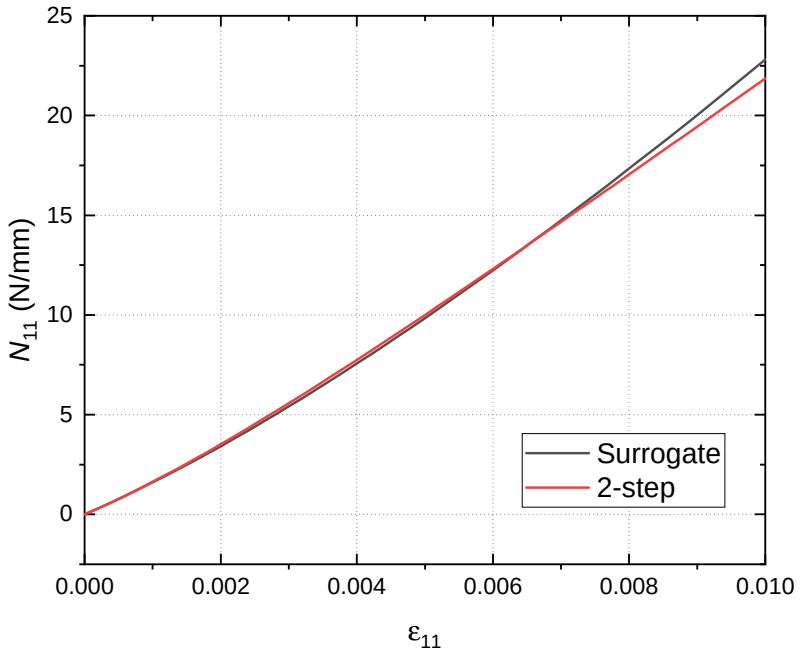

Figure 5.16. Force-strain curve of the shell with currogate model and 2-step homogenization.

only by the shell homogenization step and in this example about 1 minute. On the other hand during the study it is also found that surrogate models are highly sensitive to the sample data. If the strain state passed to the surrogate model is away from the sample data, significant loss of accuracy or divergence can happen. To construct a more general-purpose surrogate model, large amount of sample data generated with different loading conditions is necessary.

5.4 Summary

In this chapter, the formulation of the MSG-based nonlinear shell model in Section 2.4 is implemented in a nonlinear version of SwiftComp. Details of the workflow of the nonlinear SwiftComp is introduced, featuring calculating the un-prescribed macro stresses and strains based on prescribed macro stresses and strains, and a 2-step homogenization strategy that can link the MSG-based nonlinear shell analysis with the global structural analysis using

Abaqus is proposed. For conveniently implementing different types of nonlinear material constitutive models, a user-material interface called SCUMAT that shares similarity with Abaqus UMAT is developed. The SCUMAT, along with the nonlinear SwiftComp, is validated with a viscoelastic model and a continuum damage model by comparing results with Abaqus. The 2-step homogenization using nonlinear SwiftComp is also demonstrated with a unidirectional fiber reinforced composite shell. The capability of the nonlinear SwiftComp is further demonstrated with a nonlinear viscoelastic-viscoplastic constitutive model. The nonlinear viscoelastic analysis is validated with experimental results using a creep-recovery loading curve. Combined with viscoplasticity, residual deformation after recovery can be observed and longer relaxation time results in greater residual deformation. Potential of nonlinear SwiftComp to run with a surrogate model is also demonstrated, so that the computational time of nonlinear multiscale analysis can be reduced.

6. CONCLUSIONS AND FUTURE PROSPECTS

6.1 Conclusions

In this dissertation, a shell theory is developed based on the mechanics of structure genome (MSG). The MSG is a general theory that unifies structure mechanics and micromechanics. The MSG-based shell theory derived in this dissertation takes advantage of the small thickness of shell and the derivation process follows the minimization of total potential in the shell structure. This MSG-based shell theory is capable of constitutive modeling of shell structures with full anisotropy and heterogeneity in all directions. Using the MSG-based shell theory, effective constitutive relations for both classical shell model and the Reissner-Mindlin model can be obtained. It has the form of a shell stiffness matrix that can be commonly applied on a 2D global shell problem solver to obtain the global structural behavior. With the global behavior, such as shell displacements, 2D membrane strains, curvatures, section forces and moments, 3D displacements, strains and stresses in the original 3D structure can be recovered. The MSG-based shell theory is also expanded to handle shells with nonlinear material properties. The MSG-based nonlinear shell model uses a combined Euler-Newton method, with a Euler step is implemented first to proceed the loading in the tangent direction, and then a Newton-Raphson step is used to calculate the correction to obtain a converged solution. In this work, the MSG-based shell theory is applied to deal with three type of practical engineering problems: the analysis of composites curing, thin-ply high strain composites (TP-HSC) deployable structures, and shells with nonlinear behaviors.

In order to simulate the autoclave curing process of composites, the MSG-based shell theory is modified to use the bottom surface as the reference surface, so that effect of the contact between the composites part and the tool can be captured rigorously. Since only 1D structure gene (SG) is considered, the formulation is written in an analytical form. The effects of temperature change and cure shrinkage are included in the variational statement, and the change of material properties in terms of them are also modeled. In addition to the classical shell model, refined model that includes the correction due to initial curvature and transverse shear deformation are also developed. The resultant stiffness matrix has the same form as that of the Reissner-Mindlin model. Numerical examples are studied for

validating the present theory. The capability of accurately predicting the displacements of an initially curved part under non-mechanical load is demonstrated with a unidirectional shell, greatly outperforming the Abaqus composite shell section. On the other hand, the limitation on 3D strain recovery is also presented. The capability of handling nonuniform through-the-thickness temperature distribution is also validated with the same unidirectional shell structure. The accurate match with direct numerical simulation (DNS) in the analysis of a multilayered L-shape and C-channel parts going through a simplified curing cycle shows the potential of the MSG-based shell theory on predicting spring-in and residual stress introduced during composites curing, with greatly reduced computational cost with much lower number of elements and nodes required. However, the 2D global shell solver used in the study, Abaqus, has the limitation of fixing the transverse shear stiffness as constants through the whole analysis. In a more realistic simulation with the cure-hardening instantaneously linear elastic (CHILE) model, simulation with MSG-based shell theory cannot match the DNS unless the transverse shear stiffness is also fixed in the DNS. It is found by another qualitative study that the error is caused by the change of transverse shear stiffness during curing. Further research is recommended to overcome this problem.

Before simulating a TP-HSC deployable boom structure, linear viscoelasticity theory to be used in the simulation is introduced. A column bending test (CBT) and a lenticular boom coiling/deploying around a hub are studied using the MSG-based shell theory. The CBT simulation results are compared with experiments, and the curvature during folding, moment and bending stiffness during relaxation, and residual curvature immediately after unfolding show good qualitative agreement. The results from quasi-elastic (QE) and direct integration (DI) implementations match with each other during folding and relaxation, but only the DI implementation captures the curvature during recovery. Some deviations in the particular values obtained from simulation and experiments were noted. The overprediction of the curvature results in an underprediction of the effective stiffness relaxation over the 6-hour process. After recovery at zero load, it is found that the model underpredicts the residual curvature by an order of magnitude compared to the experimental results. One possible reason for this deviation in residual curvature is that the material experiences viscoplasticity, which is not included in the current material model, particularly because the

disparity between the model and the experiment is relatively constant through the recovery period. A calibration of the specimen bending stiffness D_{11}, which is the shell element stiffness used in simulation, using Dakota is also presented for demonstration purposes. The error sum of squares of the bending stiffness calculated using the same formula as experiment D_{11}^* is reduced from 99.4 to 1.6. In the simulation of the TP-HSC deployale boom and hub structure, the boom is modeled using shell elements and the hub using rigid elements. Due to the complexity of the model, several simplifications were introduced to avoid convergence difficulties. Numerical studies were carried out with two models. Results from both models show residual curvature is negligible in the longitudinal direction, but significant in the hoop direction. A 24-hour recovery greatly reduces residual deformation after deployment by more than 70%.

A nonlinear version of SwiftComp is developed for the MSG-based nonlinear shell analysis. The nonlinear SwiftComp uses the algorithm of a combined Euler-Newton method, with a Euler prediction step followed by a Newton correction step to ensure convergence. The prescribed load applied incrementally and in each increment solved by iteration. A 2-step nonlinear homogenization process for the nonlinear SwiftComp to handle laminates and woven composites and link the MSG-based nonlinear shell modeling with the global structural analysis is also proposed. For the convenience of implementing nonlinear material models, user material capability is implemented in the nonlinear SwiftComp. A user material can be defined in a subroutine SCUMAT, which can be easily converted from an Abaqus UMAT. Validation of the user material capability is done by comparing with Abaqus model. A simple viscoelastic material and a continuum damage model are tested and both show excellent match with the Abaqus results. The 2-step homogenization capability is also tested, while high computational cost is realized. A nonlinear viscoelastic-viscoplastic constitutive model developed for analyzing the permanent deformation of TP-HSC is implemented using SCUMAT. Comparison with experimental results in literature shows the nonlinear SwiftComp can accurately reproduce the nonlinear behavior observed in experiments. Studies with other SG and model types further validates the capability of nonlinear SwiftComp. To reduce the high computational cost of 2-step nonlinear homogenization, a preliminary study on using surrogate models to substitute the 3D solid homogenization step of the 2-step ho-

mogenization is carried out. Results show that the surrogate model can have close results compared with 2-step homogenization, with an error less than 5%, while greatly reduce the computational time. It is also found that surrogate models are highly sensitive to sample data, which means to construct a general-purpose surrogate model, large amount of data need to be prepared.

6.2 Future Prospects

This work shows the effectiveness of the MSG-based shell theory. On the other hand, some limitations of the current theory and its implementation are also observed. To further improve the capability of MSG-based shell theory, future studies in several aspects can be recommended.

During the simulation of composites autoclave curing, it has been found that the 3D strain recovery in a curved shell has qualitative disagreement with the direct numerical simulation (DNS) results. The magnitude of the deviation is acceptable within a shell of simple layup and geometry, while the accuracy loss can be hard to estimate with complex structures in engineering applications. The main reason of this error is the fluctuating function not been updated in the geometric correction. Based on MSG, the strain energy can be expanded based on the small parameters of a shell, h/l and h/R

$$\mathcal{J} \sim \left(hl^2\right)\left(1+\frac{h}{R}+\frac{h}{l}+\frac{h^2}{l^2}+\frac{h^2}{R^2}+\frac{h^2}{lR}+...\right)\mu\epsilon^2 \tag{6.1}$$

and the fluctuating function can be perturbed as

$$w_i = w_i^0 + w_i^1 + w_i^R \tag{6.2}$$

with the w_i^R representing the fluctuating with the order of h/R. To solve it, terms with the order of h^2/R^2, h^2/lR and h^2/l^2 need to be kept in the strain energy and since coupling terms exist, the fluctuating related with transverse shear deformation w_i^1 need to be solved together. With the updated fluctuating function, the prediction of 3D fields in curved parts should be improved.

Another limitation when simulating the composites curing is the change of transverse shear stiffness. Based on the analysis in Chapter 3, the limitation of Abaqus that fixes the shell transverse shear stiffness is the main cause of the disagreement with DNS. To overcome this limitation, a user defined shell element using the Abaqus UEL user-subroutine can be developed. With the UEL shell element, fully coupled 8×8 stiffness matrix can be implemented with user defined properties.

$$\begin{Bmatrix} N \\ M \\ Q \end{Bmatrix} = \begin{bmatrix} A & B & Y_A \\ B^{\mathrm{T}} & D & Y_D \\ Y_A^{\mathrm{T}} & Y_D^{\mathrm{T}} & G \end{bmatrix} \begin{Bmatrix} \epsilon \\ \kappa \\ \gamma \end{Bmatrix} \tag{6.3}$$

In the simulation of CBT, overpridiction is observed with the curvature after folding. The kinematics coupling used in the finite element model is a rigid coupling that force the rotation at the coupled boundary to be equal to the reference point, while in experiments the clamps can be flexible. To reduce the error from the boundary condition, better modeling of the clamp should be developed. A possible way is introducing rigid surfaces to represent the clamps along with the contact with the specimen. Then, instead of the coupling between the reference point and the specimen, the coupling should be applied on the clamps.

During the simulation of the TP-HSC deployable boom structure, the finite element model suffered from convergence issue due to the complexity of the model. The process of coiling and deployment can be considered dynamic so using Abaqus/Explicit instead of the Abaqus/Standard solver may be more suitable. However, a UGENS equivalent user-subroutine for the explicit solver, VUGENS, was not available until recent, and it lacks documentation. A preliminary study was done with the CBT finite element model, and the curvature κ_{11} along the center line of the specimen after folding is shown in Figure 6.1. In explicit analysis, simulation speed can be manually adjusted by the technique of variable mass scaling. Then using this technique, size of the time increment $\mathrm{d}t$ can be prescribed, and then the solver will automatically apply different scaling factors to the density of each element so that the whole structure can still be stable. The larger $\mathrm{d}t$, the larger the scaling factor. However, when the scaling factor becomes too large, structural behavior can be

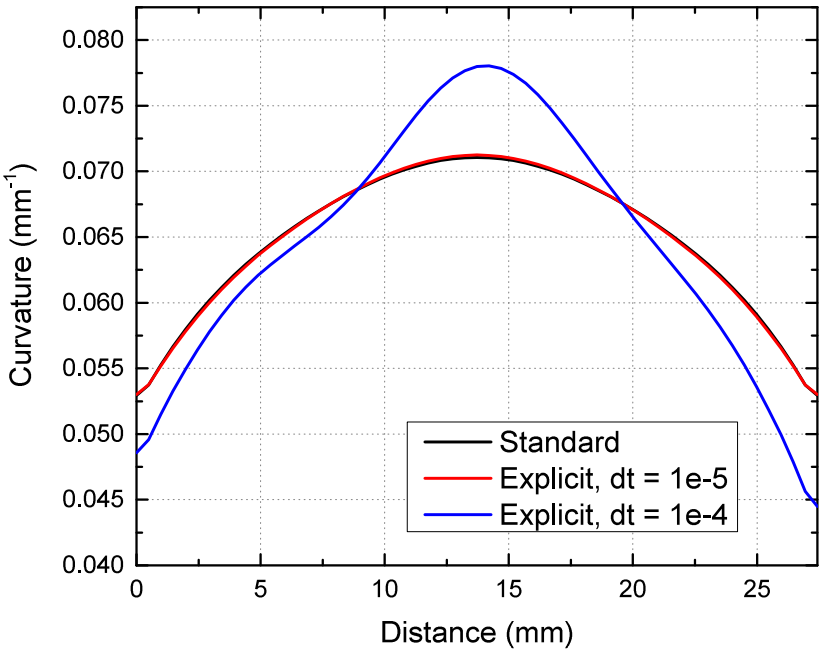

Figure 6.1. Curvature along the center line after folding.

affected, as modifying the density can change the dynamic characteristics of the structure. It can be seen from Figure 6.1 that with a smaller dt, excellent match with Abaqus/Standard can be achieved. The technique can be applied to more effectively simulate deployable boom structures.

Although the nonlinear SwiftComp is validated to be capable of generating good results with various material constitutive models, during the analysis with the nonlinear viscoelastic-viscoplastic model, stability issue with the nonlinear SwiftComp is observed. Divergence can happen when the local stresses inside the SG become large. Error accumulation is also observed. Though in most engineering practices, the stress would not be that large to make this issue significant, it is recommended to further improve the formulation and the implementation of the nonlinear SwiftComp so that it can be more robust in different types of applications.

The preliminary study on using a polynomial surrogate model in a 2-step nonlinear homogenization proves the feasibility of this method to reduce the computational cost. The high cost of nonlinear homogenization also makes adopting this method a necessity for applying the MSG-based nonlinear shell modeling in multiscale structural analysis. However, for developing more general-purpose surrogate models, machine learning is recommended. Among different machine learning techniques, neural network is the most widely used tool, been successfully applied in nonlinear constitutive modeling [126]–[128]. When applying surrogate models with multiscale structural analysis, surrogate models can be constructed for different scales: a model for the lamina/yarn level that can be used it for shell modeling, and a model for the laminate/woven penal level that can be implemented in UGENS for the global structural analysis. Sample data can be obtained through nonlinear SwiftComp, without relying on experiments.

REFERENCES

[1] N. Liu and W. Yu, "Evaluation of smeared properties approaches and mechanics of structure genome for analyzing composite beams," *Mechanics of Advanced Materials and Structures*, vol. 25, no. 14, pp. 1171–1185, 2018.

[2] S. G. Advani and K.-T. Hsiao, *Manufacturing techniques for polymer matrix composites (PMCs)*. Elsevier, 2012.

[3] T. W. Murphey, W. Francis, B. Davis, and J. M. Mejia-Ariza, "High strain composites," in *2nd AIAA Spacecraft Structures Conference*, 2015, p. 0942.

[4] J. M. Fernandez, "Advanced deployable shell-based composite booms for small satellite structural applications including solar sails," 2017.

[5] J. E. Salazar and J. M. Fernandez, "Experimental characterization of the dimensional stability of deployable composite booms during stowage," in *AIAA SciTech 2021 Forum*, Virtual Event: American Institute of Aeronautics and Astronautics, Jan. 2021. DOI: 10.2514/6.2021-0195.

[6] T. Keil and J. Banik, "Stowage and deployment strength of a rollable composite shell reflector," in *52nd AIAA/ASME/ASCE/AHS/ASC Structures, Structural Dynamics and Materials Conference 19th AIAA/ASME/AHS Adaptive Structures Conference 13t*, 2011, p. 2103.

[7] J. Fernandez, J. Banik, and E. Ardelean, "Creep effects and deployment characterization of rollable composite shell reflectors," in *53rd AIAA/ASME/ASCE/AHS/ASC Structures, Structural Dynamics and Materials Conference 20th AIAA/ASME/AHS Adaptive Structures Conference 14th AIAA*, 2012, p. 1955.

[8] D. S. Adams and M. Mobrem, "Lenticular jointed antenna deployment anomaly and resolution onboard the mars express spacecraft," *Journal of Spacecraft and Rockets*, vol. 46, no. 2, pp. 403–410, 2009.

[9] E. Cosserat and F. Cosserat, "Théorie des corps déformables," 1909.

[10] J. Ericksen and C. Truesdell, "Exact theory of stress and strain in rods and shells," *Archive for Rational Mechanics and Analysis*, vol. 1, no. 1, pp. 295–323, 1957.

[11] P. M. Naghdi, "Foundations of elastic shell theory," CALIFORNIA UNIV BERKELEY INST OF ENGINEERING RESEARCH, Tech. Rep., 1962.

[12] P. M. Naghdi, "The theory of shells and plates," in *Linear Theories of Elasticity and Thermoelasticity*, Springer, 1973, pp. 425–640.

[13] R. A. Toupin, "Theories of elasticity with couple-stress," *Archive for Rational Mechanics and Analysis*, vol. 17, no. 2, pp. 85–112, 1964.

[14] A. E. Green, P. M. Naghdi, and W. Wainwright, "A general theory of a cosserat surface," *Archive for Rational Mechanics and Analysis*, vol. 20, no. 4, pp. 287–308, 1965.

[15] H. Cohen and C. DeSilva, "Nonlinear theory of elastic directed surfaces," *Journal of Mathematical Physics*, vol. 7, no. 6, pp. 960–966, 1966.

[16] J. Simo, D. Fox, and M. Rifai, "On a stress resultant geometrically exact shell model. part ii: The linear theory; computational aspects," *Computer Methods in Applied Mechanics and Engineering*, vol. 73, no. 1, pp. 53–92, 1989.

[17] D. Fox and J. Simo, "A drill rotation formulation for geometrically exact shells," *Computer Methods in Applied Mechanics and Engineering*, vol. 98, no. 3, pp. 329–343, 1992.

[18] A. Ibrahimbegović, "Stress resultant geometrically nonlinear shell theory with drilling rotations—part i. a consistent formulation," *Computer Methods in Applied Mechanics and Engineering*, vol. 118, no. 3-4, pp. 265–284, 1994.

[19] W. Krätzig, "'best'transverse shearing and stretching shell theory for nonlinear finite element simulations," *Computer Methods in Applied Mechanics and Engineering*, vol. 103, no. 1-2, pp. 135–160, 1993.

[20] E. Reissner, "Linear and nonlinear theory of shells," *Thin-shell structures: Theory, experiment, and design*, pp. 29–44, 1974.

[21] A. E. H. Love, "Xvi. the small free vibrations and deformation of a thin elastic shell," *Philosophical Transactions of the Royal Society of London.(A.)*, no. 179, pp. 491–546, 1888.

[22] A. E. H. Love, *A treatise on the mathematical theory of elasticity*. Cambridge university press, 2013.

[23] A. L. Goldenveizer, *Theory of elastic thin shells: solid and structural mechanics*. Elsevier, 2014, vol. 2.

[24] A. I. Lurie, "On the equations of the general theory of elastic shells," *J. Appl. Math. Mech. (PMM)*, vol. 12, no. 5, p. 558, 1950.

[25] V. V. Novozhilov, *Thin shell theory*. Springer, 1959.

[26] W. Koiter, "A consistent first approximation in the general theory of thin elastic shells," in *Proceedings of the Symppsium in the Theory of Thin Elastic Shells*, 1959.

[27] J. L. Sanders, *An improved first-approximation theory for thin shells*. US Government Printing Office, 1960, vol. 24.

[28] B. Budiansky and J. L. Sanders, "On the 'best' first-order linear shell theory," in *Progress in Applied Mechanics, The Prager Anniversary Volume*, 1963, pp. 129–140.

[29] J. N. Reddy, "A simple higher-order theory for laminated composite plates," *Journal of Applied Mechanics*, vol. 51, no. 4, pp. 745–752, 1984.

[30] E. Carrera, "Theories and finite elements for multilayered, anisotropic, composite plates and shells," *Archives of Computational Methods in Engineering*, vol. 9, no. 2, pp. 87–140, 2002.

[31] W. Yu, "A unified theory for constitutive modeling of composites," *Journal of Mechanics of Materials and Structures*, vol. 11, no. 4, pp. 379–411, 2016.

[32] W. Yu, "Simplified formulation of mechanics of structure genome," *AIAA Journal*, pp. 1–9, 2019.

[33] W. Yu, "An introduction to micromechanics," in *Applied Mechanics and Materials*, Trans Tech Publ, vol. 828, 2016, pp. 3–24.

[34] V. L. Berdichevskii, "Variational-asymptotic method of constructing a theory of shells: Pmm vol. 43, no. 4, 1979, pp. 664–687," *Journal of Applied Mathematics and Mechanics*, vol. 43, no. 4, pp. 711–736, 1979.

[35] W. Yu, D. H. Hodges, and V. V. Volovoi, "Asymptotic construction of Reissner-like composite plate theory with accurate strain recovery," *International Journal of Solids and Structures*, vol. 39, no. 20, pp. 5185–5203, 2002.

[36] W. Yu, D. H. Hodges, and V. V. Volovoi, "Asymptotic generalization of reissner–mindlin theory: Accurate three-dimensional recovery for composite shells," *Computer Methods in Applied Mechanics and Engineering*, vol. 191, no. 44, pp. 5087–5109, 2002.

[37] L. Liao and W. Yu, "Asymptotical construction of a fully coupled, Reissner–Mindlin model for piezoelectric composite plates," *Smart Materials and Structures*, vol. 17, no. 1, p. 015 010, 2008.

[38] H. Chen and W. Yu, "A multiphysics model for magneto-electro-elastic laminates," *European Journal of Mechanics-A/Solids*, vol. 47, pp. 23–44, 2014.

[39] Y. Long and W. Yu, "Asymptotical modeling of thermopiezoelastic laminates," *Smart Materials and Structures*, vol. 25, no. 1, p. 015 002, 2015.

[40] H. Chen and W. Yu, "Asymptotical construction of an efficient high-fidelity model for multilayer functionally graded plates," *AIAA Journal*, vol. 48, no. 6, pp. 1171–1183, 2010.

[41] X. Liu, T. Tang, W. Yu, and R. B. Pipes, "Multiscale modeling of viscoelastic behaviors of textile composites," *International Journal of Engineering Science*, vol. 130, pp. 175–186, 2018.

[42] H. Hahn and N. Pagano, "Curing stresses in composite laminates," *Journal of Composite Materials*, vol. 9, pp. 91–106, 1975.

[43] A. C. Loos and G. S. Springer, "Curing of epoxy matrix composites," *Journal of composite materials*, vol. 17, no. 2, pp. 135–169, 1983.

[44] S. White and H. Hahn, "Mechanical property and residual stress development during cure of a graphite/bmi composite," *Polymer Engineering & Science*, vol. 30, no. 22, pp. 1465–1473, 1990.

[45] S. White and H. Hahn, "Process modeling of composite materials: Residual stress development during cure. part i. model formulation," *Journal of Composite Materials*, vol. 26, no. 16, pp. 2402–2422, 1992.

[46] S. White and H. Hahn, "Process modeling of composite materials: Residual stress development during cure. part ii. experimental validation," *Journal of Composite Materials*, vol. 26, no. 16, pp. 2423–2453, 1992.

[47] T. A. Bogetti and J. W. Gillespie Jr, "Two-dimensional cure simulation of thick thermosetting composites," *Journal of Composite Materials*, vol. 25, no. 3, pp. 239–273, 1991.

[48] T. A. Bogetti and J. W. Gillespie Jr, "Process-induced stress and deformation in thick-section thermoset composite laminates," *Journal of composite materials*, vol. 26, no. 5, pp. 626–660, 1992.

[49] A. A. Johnston, "An integrated model of the development of process-induced deformation in autoclave processing of composite structures," Ph.D. dissertation, University of British Columbia, 1997.

[50] G. Twigg, A. Poursartip, and G. Fernlund, "Tool–part interaction in composites processing. part i: Experimental investigation and analytical model," *Composites Part A: Applied Science and Manufacturing*, vol. 35, no. 1, pp. 121–133, 2004.

[51] G. Twigg, A. Poursartip, and G. Fernlund, "Tool–part interaction in composites processing. part ii: Numerical modelling," *Composites Part A: Applied Science and Manufacturing*, vol. 35, no. 1, pp. 135–141, 2004.

[52] S. Clifford, N. Jansson, W. Yu, V. Michaud, and J.-A. Månson, "Thermoviscoelastic anisotropic analysis of process induced residual stresses and dimensional stability in real polymer matrix composite components," *Composites Part A: Applied Science and Manufacturing*, vol. 37, no. 4, pp. 538–545, 2006.

[53] N. Zobeiry, R. Vaziri, and A. Poursartip, "Computationally efficient pseudo-viscoelastic models for evaluation of residual stresses in thermoset polymer composites during cure," *Composites Part A: Applied Science and Manufacturing*, vol. 41, no. 2, pp. 247–256, Feb. 2010. DOI: 10.1016/j.compositesa.2009.10.009. [Online]. Available: https://doi.org/10.1016/j.compositesa.2009.10.009.

[54] A. R. A. Arafath, R. Vaziri, and A. Poursartip, "Modelling process-induced deformations in composite structures using higher order elements," in *16th International Conference on Composite Materials, Kyoto, Japan*, 2007.

[55] A. R. A. Arafath, R. Vaziri, and A. Poursartip, "Closed-form solution for process-induced stresses and deformation of a composite part cured on a solid tool: Part i–flat geometries," *Composites Part A: Applied Science and Manufacturing*, vol. 39, no. 7, pp. 1106–1117, 2008.

[56] A. R. A. Arafath, R. Vaziri, and A. Poursartip, "Closed-form solution for process-induced stresses and deformation of a composite part cured on a solid tool: Part ii–curved geometries," *Composites Part A: Applied Science and Manufacturing*, vol. 40, no. 10, pp. 1545–1557, 2009.

[57] N. Ersoy, T. Garstka, K. Potter, M. R. Wisnom, D. Porter, and G. Stringer, "Modelling of the spring-in phenomenon in curved parts made of a thermosetting composite," *Composites Part A: Applied Science and Manufacturing*, vol. 41, no. 3, pp. 410–418, 2010.

[58] O. G. Kravchenko, C. Li, A. Strachan, S. G. Kravchenko, and R. B. Pipes, "Prediction of the chemical and thermal shrinkage in a thermoset polymer," *Composites Part A: Applied Science and Manufacturing*, vol. 66, pp. 35–43, 2014.

[59] E. Kappel, D. Stefaniak, and G. Fernlund, "Predicting process-induced distortions in composite manufacturing–a pheno-numerical simulation strategy," *Composite Structures*, vol. 120, pp. 98–106, 2015.

[60] A. Ding, S. Li, J. Wang, and A. Ni, "A new analytical solution for spring-in of curved composite parts," *Composites Science and Technology*, vol. 142, pp. 30–40, 2017.

[61] K. Gordnian, "Crystallization and thermo-viscoelastic modelling of polymer composites," Ph.D. dissertation, University of British Columbia, 2017.

[62] D. Li, X. Li, J. Dai, and S. Xi, "A comparison of curing process-induced residual stresses and cure shrinkage in micro-scale composite structures with different constitutive laws," *Applied Composite Materials*, vol. 25, no. 1, pp. 67–84, 2018.

[63] K. Gordnian, A. Forghani, R. Brockman, and A. Poursartip, "Experimental and numerical investigation of effects of cure cycle on process-induced-distortions of carbon fibre reinforced composites," in *SAMPE 2019 - Charlotte, NC*, SAMPE, Apr. 2019. DOI: 10.33599/nasampe/s.19.1434. [Online]. Available: https://doi.org/10.33599/nasampe/s.19.1434.

[64] W. Chen and D. Zhang, "Improved prediction of residual stress induced warpage in thermoset composites using a multiscale thermo-viscoelastic processing model," *Composites Part A: Applied Science and Manufacturing*, vol. 126, p. 105 575, Nov. 2019. DOI: 10.1016/j.compositesa.2019.105575. [Online]. Available: https://doi.org/10.1016/j.compositesa.2019.105575.

[65] I. Convergent Manufacturing Technologies, *Compro cca for abaqus modeling guidelines*, 2015.

[66] O. Rique Garaizar, Y. Long, J. Goodsell, W. Yu, and R. B. Pipes, "Composite de-tooling simulation using an improved plate and shell theory base on mechanics of structure genome," in *Proceedings of the American Society for Composites: Thirty-First Technical Conference*, 2016.

[67] H. Mallikarachchi, "Thin-walled composite deployable booms with tape-spring hinges," Ph.D. dissertation, University of Cambridge, 2011.

[68] H. Mallikarachchi and S. Pellegrino, "Quasi-static folding and deployment of ultrathin composite tape-spring hinges," *Journal of Spacecraft and Rockets*, vol. 48, no. 1, pp. 187–198, 2011.

[69] H. Mallikarachchi and S. Pellegrino, "Design and validation of thin-walled composite deployable booms with tape-spring hinges," in *52nd AIAA/ASME/ASCE/AHS/ASC Structures, Structural Dynamics and Materials Conference 19th AIAA/ASME/AHS Adaptive Structures Conference 13t*, 2011, p. 2019.

[70] K. Kwok and S. Pellegrino, "Micromechanics models for viscoelastic plain-weave composite tape springs," *AIAA Journal*, vol. 55, no. 1, pp. 309–321, 2016.

[71] M. Yapa Hamillage, K. Kwok, and J. M. Fernandez, "Micromechanical modeling of high-strain thin-ply composites," in *AIAA Scitech 2019 Forum*, 2019, p. 1751.

[72] J. Tetsuka, H. Nagaoka, and T. Matsuda, "Analysis of micro/meso/macro temperature-dependent elastoviscoplastic properties of woven composites," in *22nd International Conference on Composite Materials*, 2019.

[73] J. Yee and S. Pellegrino, "Folding of woven composite structures," *Composites Part A: Applied Science and Manufacturing*, vol. 36, no. 2, pp. 273–278, 2005.

[74] J. Yee and S. Pellegrino, "Biaxial bending failure locus for woven-thin-ply carbon fibre reinforced plastic structures," in *46th AIAA/ASME/ASCE/AHS/ASC Structures, Structural Dynamics and Materials Conference*, Austin, Texas: American Institute of Aeronautics and Astronautics, Apr. 2005, p. 1811.

[75] J. Yee and S. Pellegrino, "Composite tube hinges," *Journal of Aerospace Engineering*, vol. 18, no. 4, pp. 224–231, 2005.

[76] G. E. Sanford, E. V. Ardelean, T. W. Murphey, and M. M. Grigoriev, "High strain test method for thin composite laminates," in *16th International Conference on Composite Structures*, A. J. M. Ferreira, Ed., Porto, Portugal: Faculty of Engineering University of Porto, 2011.

[77] J. M. Fernandez and T. W. Murphey, "A simple test method for large deformation bending of thin high strain composite flexures," in *2018 AIAA Spacecraft Structures Conference*, 2018, p. 0942.

[78] Y. Long, O. Rique, W. Yu, J. M. Fernandez, and A. C. Bergan, "Multiscale simulation of deployable composite structures," in *AIAA SciTech 2021 Forum*, Virtual Event: American Institute of Aeronautics and Astronautics, Jan. 2021. DOI: 10.2514/6.2021-0199.

[79] A. H. Sharma, T. Rose, A. Seamone, T. W. Murphey, and F. Lopez Jimenez, "Analysis of the column bending test for large curvature bending of high strain composites," in *AIAA SciTech 2019 Forum*, San Diego, California: American Institute of Aeronautics and Astronautics, Jan. 2019, p. 1746.

[80] T. Rose, J. Calish, and F. Lopez Jimenez, "Modeling of viscoelasticity in thin flexible composites using coincident element method," in *AIAA SciTech 2020 Forum*, Orlando, Florida: American Institute of Aeronautics and Astronautics, Jan. 2020, p. 0693.

[81] A. Gomez-Delrio and K. Kwok, "Stowage and recovery of thin-ply composite deployable structures," in *AIAA SciTech 2020 Forum*, Orlando, Florida: American Institute of Aeronautics and Astronautics, Jan. 2020, p. 0205.

[82] J. Bai, J. Xiong, J. Gao, and X. Yi, "Analytical solutions for predicting in-plane strain and interlaminar shear stress of ultra-thin-walled lenticular collapsible composite tube in fold deformation," *Composite Structures*, vol. 97, pp. 64–75, 2013.

[83] A. Brinkmeyer, S. Pellegrino, and P. M. Weaver, "Effects of long-term stowage on the deployment of bistable tape springs," *Journal of Applied Mechanics*, vol. 83, no. 1, p. 011 008, 2016.

[84] Y. Hu, W. Chen, J. Gao, J. Hu, G. Fang, and F. Peng, "A study of flattening process of deployable composite thin-walled lenticular tubes under compression and tension," *Composite Structures*, vol. 168, pp. 164–177, 2017.

[85] E. C. Borowski, E. M. Soliman, A. I. Khan, and M. M. R. Taha, "Stowage and deployment of a viscoelastic orthotropic carbon-fiber composite tape spring," *Journal of Spacecraft and Rockets*, vol. 55, no. 4, pp. 829–840, 2018.

[86] A. Gomez-Delrio and K. Kwok, "Viscoelastic analysis of stowage and quasi-static deployment of composite tape springs," in *2018 AIAA Spacecraft Structures Conference*, 2018, p. 0940.

[87] K. Cox and K. A. Medina, "Scalability of triangular rollable and collapsible booms," in *AIAA Scitech 2019 Forum*, 2019, p. 2026.

[88] H. Yang, L. Liu, H. Guo, F. Lu, and Y. Liu, "Wrapping dynamic analysis and optimization of deployable composite triangular rollable and collapsible booms," *Structural and Multidisciplinary Optimization*, vol. 59, no. 4, pp. 1371–1383, 2019.

[89] M. Scherbarth and M. R. Taha, "Stowage testing and modeling of viscoelastic composite tape springs," in *AIAA Scitech 2019 Forum*, 2019, p. 1748.

[90] C. Leclerc and S. Pellegrino, "Reducing stress concentration in the transition region of coilable ultra-thin-shell booms," in *AIAA SciTech 2019 Forum*, 2019, p. 1522.

[91] A. Gomez-Delrio and K. Kwok, "Stowage and recovery of thin-ply composite deployable structures," in *AIAA Scitech 2020 Forum*, American Institute of Aeronautics and Astronautics, Jan. 2020. DOI: 10.2514/6.2020-0205.

[92] E. Ramm and A. Matzenmiller, "Consistent linearization in elasto-plastic shell analysis," *Engineering Computations*, 1988.

[93] S. Swaddiwudhipong and Z. Liu, "Dynamic response of large strain elasto-plastic plate and shell structures," *Thin-Walled Structures*, vol. 26, no. 4, pp. 223–239, 1996.

[94] C. Wang, C. Sun, and T. Gates, "Elastic/viscoplastic behavior of fiber-reinforced thermoplastic composites," *Journal of reinforced plastics and composites*, vol. 15, no. 4, pp. 360–377, 1996.

[95] X. Peng and J. Cao, "A dual homogenization and finite element approach for material characterization of textile composites," *Composites Part B: Engineering*, vol. 33, no. 1, pp. 45–56, 2002.

[96] Y.-C. Chen, K. R. Rajagopal, and L. Wheeler, "Homogenization and global responses of inhomogeneous spherical nonlinear elastic shells," *Journal of Elasticity*, vol. 82, no. 3, pp. 193–214, 2006.

[97] T. Rabczuk, P. M. A. Areias, and T. Belytschko, "A meshfree thin shell method for non-linear dynamic fracture," *International journal for numerical methods in engineering*, vol. 72, no. 5, pp. 524–548, 2007.

[98] J. Caseiro, R. Valente, A. Reali, J. Kiendl, F. Auricchio, and R. A. de Sousa, "Assumed natural strain nurbs-based solid-shell element for the analysis of large deformation elasto-plastic thin-shell structures," *Computer Methods in Applied Mechanics and Engineering*, vol. 284, pp. 861–880, 2015.

[99] B. R. Goncalves, J. Jelovica, and J. Romanoff, "A homogenization method for geometric nonlinear analysis of sandwich structures with initial imperfections," *International Journal of Solids and Structures*, vol. 87, pp. 194–205, 2016.

[100] A. Bensoussan, J.-L. Lions, and G. Papanicolaou, *Asymptotic analysis for periodic structures*. American Mathematical Soc., 2011, vol. 374.

[101] W. Yu, *SwiftComp^{TM} user manual - version 2.1*, 2020. [Online]. Available: https://cdmhub.org/resources/scstandard/supportingdocs.

[102] F. Jiang and W. Yu, "Nonlinear variational asymptotic sectional analysis of hyperelastic beams," *AIAA Journal*, vol. 54, no. 2, pp. 679–690, 2016.

[103] F. Jiang and W. Yu, "Damage analysis by physically nonlinear composite beam theory," *Composite Structures*, vol. 182, pp. 652–665, 2017.

[104] L. Zhang and W. Yu, "Variational asymptotic homogenization of elastoplastic composites," *Composite Structures*, vol. 133, pp. 947–958, 2015.

[105] D. A. Danielson and D. H. Hodges, "Nonlinear beam kinematics by decomposition of the rotation tensor," *Journal of Applied Mechanics*, vol. 54, no. 2, pp. 258–262, 1987.

[106] W. Yu and D. H. Hodges, "A geometrically nonlinear shear deformation theory for composite shells," *Journal of Applied Mechanics*, vol. 71, no. 1, pp. 1–9, 2004.

[107] W. Yu, "Variational asymptotic modeling of composite dimensionally reducible structures," Ph.D. dissertation, Georgia Institute of Technology, 2002.

[108] C. Teng, W. Yu, and M. Y. Chen, "Variational asymptotic homogenization of temperature-dependent heterogeneous materials under finite temperature changes," *International Journal of Solids and Structures*, vol. 49, no. 18, pp. 2439–2449, 2012.

[109] V. Misyura, "Effect of accuracy loss in classical shell theory," *Journal of Applied Mechanics*, vol. 59, S217, 1992.

[110] V. L. Berdichevsky, *Variational Principles of Continuum Mechanics*. Springer, 2009.

[111] J. Ren, "Exact solutions for laminated cylindrical shells in cylindrical bending," *Composites Science and Technology*, vol. 29, no. 3, pp. 169–187, 1987.

[112] J. Noh and J. Whitcomb, "Efficient techniques for predicting viscoelastic behavior of sublaminates," *Composites Part B: Engineering*, vol. 34, no. 8, pp. 727–736, 2003.

[113] M. Zocher, S. Groves, and D. H. Allen, "A three-dimensional finite element formulation for thermoviscoelastic orthotropic media," *International Journal for Numerical Methods in Engineering*, vol. 40, no. 12, pp. 2267–2288, 1997.

[114] R. Schapery, "Stress analysis of viscoelastic composite materials," *Journal of Composite Materials*, vol. 1, no. 3, pp. 228–267, 1967.

[115] O. Rique Garaizar, "Multiscale thermoviscoelastic modeling of composite materials," Ph.D. dissertation, Purdue University, 2021.

[116] J. M. Fernandez, *Personal communication*, May 2021.

[117] Abaqus, *6.14 documentation*, Dassault Systèmes Simulia Corporation, 2014.

[118] J. M. Fernandez, J. Salazar, M. Y. Hamillage, A. Gomez-Delrio, and K. Kwok, "Large deformation bending relaxation of thin ply composites laminates," in *22nd International Conference on Composite Materials*, 2019.

[119] O. Rique, Y. Long, W. Yu, R. B. Pipes, J. M. Fernandez, and A. C. Bergan, "Improved plate and beam models for thermoviscoelastic constitutive modeling of composites," in *American Society for Composites 2020*, Virtual Conference: DEStech Publications, Inc., Sep. 2020. DOI: 10.12783/asc35/34929.

[120] *Dakota, a multilevel parallel object-oriented framework for design optimization, parameter estimation, uncertainty quantification, and sensitivity analysis: Version 6.11 user's manual*, Sandia National Laboratories, 2019.

[121] A. J. Lee and J. M. Fernandez, "Inducing bistability in collapsible tubular mast booms with thin-ply composite shells," *Composite Structures*, p. 111 166, 2019.

[122] Abaqus, *2017 documentation*, Dassault Systèmes Simulia Corporation, 2017.

[123] L. Zhang and W. Yu, "Constitutive modeling of damageable brittle and quasi-brittle materials," *International Journal of Solids and Structures*, vol. 117, pp. 80–90, 2017.

[124] L. Zhang, W. Klimm, K. Kwok, J. M. Fernandez, A. C. Bergan, and W. Yu, "A nonlinear viscoelastic-viscoplastic constitutive model for epoxy polymers," in *AIAA SciTech 2022 Forum*, San Diego, California: American Institute of Aeronautics and Astronautics, Jan. 2022.

[125] J. Lai and A. Bakker, "3-d schapery representation for non-linear viscoelasticity and finite element implementation," *Computational mechanics*, vol. 18, no. 3, pp. 182–191, 1996.

[126] P. M. DeVries, T. B. Thompson, and B. J. Meade, "Enabling large-scale viscoelastic calculations via neural network acceleration," *Geophysical Research Letters*, vol. 44, no. 6, pp. 2662–2669, 2017.

[127] X. Liu, F. Tao, and W. Yu, "A neural network enhanced system for learning nonlinear constitutive law and failure initiation criterion of composites using indirectly measurable data," *Composite Structures*, vol. 252, p. 112 658, 2020.

[128] D. W. Abueidda, S. Koric, N. A. Sobh, and H. Sehitoglu, "Deep learning for plasticity and thermo-viscoplasticity," *International Journal of Plasticity*, vol. 136, p. 102 852, 2021.

VITA

Yufei Long was born in Wuhan, Hubei Province, China. He earned his Bachelor's degree in Aircraft Manufacturing Engineering from Harbin Institute of Technology. During his undergraduate study, he got a chance to study at National Tsing-Hua University as an exchange student. In 2013, he started his graduate study at Purdue University working in the Multiscale Structural Mechanics Lab led by Dr. Wenbin Yu. He earned his Master's degree and continued as PhD student under the supervision of Dr. Yu. During the course of the PhD program he did an internship at Dassault Systèmes SIMULIA, Johnston, Rhode Island. His research focuses on linear and nonlinear plate and shell theories, with an emphasis on the mechanics of structure genome-based theory, and finite element simulation of thin structures using shell elements. He finished his PhD in Aeronautics and Astronautics in December 2021.